

**University of Alberta**

**H<sub>2</sub>S-POWERED SOLID OXIDE FUEL CELLS**

by

**MAN LIU**



A thesis submitted to the Faculty of Graduate Studies and Research in partial  
fulfillment of the requirements for the degree of **Doctor of Philosophy**

in

**Chemical Engineering**

Department of Chemical and Materials Engineering

Edmonton, Alberta

Spring 2004



Library and  
Archives Canada

Bibliothèque et  
Archives Canada

Published Heritage  
Branch

Direction du  
Patrimoine de l'édition

395 Wellington Street  
Ottawa ON K1A 0N4  
Canada

395, rue Wellington  
Ottawa ON K1A 0N4  
Canada

*Your file* *Votre référence*  
*ISBN: 0-612-96296-2*  
*Our file* *Notre référence*  
*ISBN: 0-612-96296-2*

The author has granted a non-exclusive license allowing the Library and Archives Canada to reproduce, loan, distribute or sell copies of this thesis in microform, paper or electronic formats.

L'auteur a accordé une licence non exclusive permettant à la Bibliothèque et Archives Canada de reproduire, prêter, distribuer ou vendre des copies de cette thèse sous la forme de microfiche/film, de reproduction sur papier ou sur format électronique.

The author retains ownership of the copyright in this thesis. Neither the thesis nor substantial extracts from it may be printed or otherwise reproduced without the author's permission.

L'auteur conserve la propriété du droit d'auteur qui protège cette thèse. Ni la thèse ni des extraits substantiels de celle-ci ne doivent être imprimés ou autrement reproduits sans son autorisation.

---

In compliance with the Canadian Privacy Act some supporting forms may have been removed from this thesis.

Conformément à la loi canadienne sur la protection de la vie privée, quelques formulaires secondaires ont été enlevés de cette thèse.

While these forms may be included in the document page count, their removal does not represent any loss of content from the thesis.

Bien que ces formulaires aient inclus dans la pagination, il n'y aura aucun contenu manquant.

# Canada

## ABSTRACT

The potential utilization of hydrogen sulfide as fuel in solid oxide fuel cells has been investigated using an oxide-ion conducting YSZ electrolyte and different kinds of anode catalysts at operating temperatures in the range of 700-900°C and at atmospheric pressure. This technology offers an economically attractive alternative to present methods for removing toxic and corrosive H<sub>2</sub>S gas from sour gas streams and a promising approach for cogenerating electrical energy and useful chemicals. The primary objective of the present research was to find active and stable anode materials.

Fuel cell experimental results showed that platinum was a good electrocatalyst for the conversion of H<sub>2</sub>S, but the Pt/YSZ interface was physically unstable due to the reversible formation and decomposition of PtS in H<sub>2</sub>S streams at elevated temperatures. Moreover, instability of the Pt/YSZ interface was accelerated significantly by electrochemical reactions, and ultimately led to the detachment of the Pt anode from the electrolyte. It has been shown that an interlayer of TiO<sub>2</sub> stabilized the Pt anode on YSZ electrolyte, thereby prolonging cell lifetime. However, the current output for a fuel cell using Pt/TiO<sub>2</sub> as anode was not improved compared to using Pt alone.

It was therefore necessary to investigate novel anode systems for H<sub>2</sub>S-air SOFCs. New anode catalysts comprising composite metal sulfides were developed. These catalysts exhibited good electrical conductivity and better catalytic activity than Pt. In contrast to MoS<sub>2</sub> alone, composite catalysts (M-Mo-S, M = Fe, Co, Ni) were not volatile and had superior stability. However, when used for extended periods of time, detachment of Pt current collecting film from anodes comprising metal sulfides alone resulted in a large increase in contact resistance and reduction in cell performance. Consequently, a

systematic investigation was conducted to identify alternative electronic conductors for use with M-Mo-S catalysts. Anode catalysts comprising Co-Mo-S admixed with up to 10% Ag powder were found to have excellent performance and longevity, as well as improved electrical contact when compared with Pt/M-Mo-S anode systems. The highest current density of  $450 \text{ mA/cm}^2$  and power density of  $115 \text{ mW/cm}^2$  were achieved with an anode that consisted of 95%(Co-Mo-S) and 5%Ag.

## ACKNOWLEDGEMENTS

I would like to express my deepest gratitude to my supervisors Prof. Jingli Luo and Prof. Karl T. Chuang, for their guidance, patience and understanding throughout my studies at U of A.

I am truly grateful to Dr. Alan R. Sanger for many valuable suggestions and comments regarding my research and this dissertation.

I am also indebted to the present and past members of the fuel cell group for the encouraging and caring environment they created around me. I would like to particularly thank Ping He and Guolin Wei for their collaboration, assistance and many beneficial discussions. I would also like to acknowledge the help of Weizhu An and Hui Wang with GC analysis.

I am so grateful that I grew up in a loving family and I cannot thank my parents enough for their unceasing love, encouragement and support since I was born. I dedicate this dissertation to them. Finally, I would like to thank my husband, Haitao Zhang, for his encouragement and unwavering support throughout these years. He kept reminding me of what is truly important in life, which has become a constant source of inspiration for me to cheer up in the most difficult days of my research work.

# Table of Contents

<b>Chapter 1</b>	<b>Introduction</b>	<b>1</b>
	1.1 Introduction	1
	1.2 Fuel Cells	5
	1.2.1 Fuel cell benefits and development	5
	1.2.2 Types of fuel cells	7
	1.3 Current Hydrogen Sulfide Removal Technology	12
	1.4 Fuel Cells for Conversion of Hydrogen Sulfide	15
	1.4.1 Benefits	15
	1.4.2 Objectives	16
	References	16
<b>Chapter 2</b>	<b>Principles of Fuel Cells</b>	<b>20</b>
	2.1 Introduction	20
	2.2 Fuel Cell Thermodynamics	21
	2.2.1 Theoretical reversible potential	21
	2.2.2 Fuel cell efficiencies	23
	2.3 Fuel Cell Polarization and Current-Potential Relationships	25
	2.3.1 Activation polarization	27
	2.3.2 Ohmic polarization	30
	2.3.3 Concentration polarization	31
	2.4 Power Characteristics	32

	2.5 Electrochemical Impedance	33
	References	38
<b>Chapter 3</b>	<b>Literature Review</b>	<b>40</b>
	3.1 Structure and Operation of Solid Oxide Fuel Cells	40
	3.1.1 Principles of operation	41
	3.1.2 Materials for solid oxide fuel cells	43
	3.1.2.1 Electrolyte	44
	3.1.2.2 Cathode	47
	3.1.2.3 Anode	50
	3.2 H <sub>2</sub> S-powered Solid Oxide Fuel Cells	52
	3.2.1 Electrochemical and chemical reactions	52
	3.2.2 Results from earlier studies	56
	References	60
<b>Chapter 4</b>	<b>H<sub>2</sub>S-powered Solid Oxide Fuel Cell Using Platinum</b>	<b>65</b>
	<b>Electrodes</b>	
	4.1 Introduction	65
	4.2 Experimental	66
	4.2.1 Cell preparation	66
	4.2.2 Fuel cell system design	68
	4.2.3 Electrochemical apparatus	70
	4.2.4 Gas analysis	71

4.3	Results and Discussion	73
4.3.1	Use of 5% hydrogen sulfide as fuel	73
4.3.1.1	Open circuit voltage	73
4.3.1.2	Current-voltage and power density performance	75
4.3.1.3	Impedance characteristics	77
4.3.1.4	Identification of limiting factors to cell performance	81
4.3.2	Use of pure hydrogen sulfide as fuel	82
4.3.2.1	Cell performance	82
4.3.2.2	Impedance characteristics	85
4.3.2.3	Stability test of Pt anode using impedance technique	89
4.3.3	Gas analysis	92
4.4	Conclusions	99
	References	100
<b>Chapter 5</b>	<b>Use of an Intermediate TiO<sub>2</sub> Layer to Improve Stability of Platinum Anode Catalyst in a H<sub>2</sub>S-air SOFC</b>	<b>102</b>
5.1	Introduction	102
5.2	Experimental	103
5.2.1	Cell preparation and construction	103
5.2.2	Preparation of TiO <sub>2</sub> /YSZ wafer	105
5.2.3	Electrochemical measurements	105

5.2.4	Characterization of solids	105
5.3	Results and Discussion	106
5.3.1	Cell performance and stability of Pt anode in pure H <sub>2</sub> S stream	106
5.3.2	Improvement of anode-YSZ stability by interposition of a TiO <sub>2</sub> layer	113
5.4	Conclusions	125
	References	126
<b>Chapter 6</b>	<b>Performance Characteristics of H<sub>2</sub>S-powered Solid Oxide Fuel Cells Using Metal Sulfide Anode Catalysts</b>	<b>128</b>
6.1	Introduction	128
6.2	Experimental	130
6.2.1	Preparation of anode catalysts	130
6.2.2	Measurement of electrical resistivity of anode catalysts	131
6.2.3	Cell preparation and construction	131
6.2.4	Electrochemical characterization	134
6.2.5	Volatility of catalyst materials	135
6.3	Results and Discussions	135
6.3.1	Resistivity of MoS <sub>2</sub> and M-Mo-S (M = Fe, Co, Ni)	135
6.3.2	Electrochemical characteristics of metal sulfide anode catalysts	137
6.3.2.1	CoMoO <sub>4</sub>	137

6.3.2.2	MoS <sub>2</sub>	139
6.3.2.3	Fe-Mo-S	143
6.3.2.4	Ni-Mo-S	146
6.3.2.5	Co-Mo-S	149
6.3.3	Admixing Ag powder into Co-Mo-S anode catalyst	155
6.3.3.1	Current-voltage and power density performance	155
6.3.3.2	Impedance characteristics	159
6.4	Conclusions	167
	References	167
<b>Chapter 7</b>	<b>Conclusions, Recommendations and Future Work</b>	<b>170</b>
7.1	Pt Anode Catalyst Directly Deposited on YSZ	170
7.2	Stabilization of Pt Anode Catalyst with TiO <sub>2</sub> Interlayer	172
7.3	Metal Sulfide Anode Catalysts	173
7.4	Product Distribution of H <sub>2</sub> S-Air Fuel Cell	174
	References	175
<b>Appendix A</b>	<b>GC Analysis</b>	<b>177</b>
A.1	Operating Parameters of GC and Detectors	177
A.2	Typical Chromatograph	179
A.3	Calculation of Reaction Rates of H <sub>2</sub> S, SO <sub>2</sub> and H <sub>2</sub>	181
A.4	Conversions of H <sub>2</sub> S and H <sub>2</sub>	181
A.5	Calculation of Stoichiometric Values in Figures 4-14 and 4-15	182

## List of Tables

Table 1-1	Historical and projected global use of fossil fuels for electricity generation, 1995-2020 (% of total energy consumption)	3
Table 1-2	Essential characteristics of different types of fuel cells	8
Table 3-1	Ionic conductivity of some typical or candidate SOFC electrolytes	48
Table 3-2	Thermodynamic data for different fuel cell reactions	54
Table 3-3	Equilibrium compositions of species from the decomposition reaction of H <sub>2</sub> S	55
Table 6-1	Electrical resistivities of anode catalysts: MoS <sub>2</sub> or M-Mo-S (M = Fe, Co, Ni)	136
Table 6-2	Cell area specific ohmic resistance (R·A) using different anode materials at selected operating temperatures	142
Table A-1	Parameters under which GC and its detectors worked for analysis of sulfur-containing compounds	177
Table A-2	Parameters under which GC and its detector worked for analysis of H <sub>2</sub>	178
Table A-3	Conversions of H <sub>2</sub> S and H <sub>2</sub>	182

## List of Figures

Figure 1-1	Schematic of a three-stage Claus process	13
Figure 2-1	Typical relationship of cell potential to current for fuel cells, showing which regions are controlled by various types of polarization	28
Figure 2-2	Typical cell efficiency and power density vs. current density plots	34
Figure 2-3	(a) An impedance spectrum and (b) simplified equivalent circuit for a fuel cell	36
Figure 3-1	Schematic diagram of a SOFC	42
Figure 4-1	(a) Microstructure of a Pt electrode. (b) SEM micrograph of cross section of a Pt/YSZ interface	67
Figure 4-2	Configuration of first experimental H <sub>2</sub> S-air fuel cell assembly	69
Figure 4-3	Schematic drawing of the gas analysis system for anode effluent streams	72
Figure 4-4	Current-voltage measurements and power curves of a cell tested using 5% H <sub>2</sub> S at 750°C, 800°C and 850°C	76
Figure 4-5	Impedance spectra for 5% H <sub>2</sub> S, Pt/8% YSZ/Pt, air fuel cell at 750°C and 800°C under open circuit conditions	78
Figure 4-6	(a) Cell impedance spectra using 5% H <sub>2</sub> S as fuel at 750°C and 800°C under polarization condition; (b) simulated equivalent circuit	79

Figure 4-7	Contribution of various component effects to polarization for a H <sub>2</sub> S-O <sub>2</sub> cell at 800°C	83
Figure 4-8	Current-potential curves for a cell using pure H <sub>2</sub> S at 750°C and 800°C	84
Figure 4-9	Impedance spectra of the Pt/YSZ/Pt cell at OCV under the influence of an applied potential at 800°C	86
Figure 4-10	Impedance spectra of the Pt/YSZ/Pt cell using pure H <sub>2</sub> S fuel at 750°C and 800°C under polarization at 0 V	88
Figure 4-11	Cell specific ohmic resistance (R <sub>o</sub> ) changes with exposure time under open circuit conditions when using pure H <sub>2</sub> S feed	90
Figure 4-12	Impedance spectra of a Pt/8% YSZ/Pt cell using pure H <sub>2</sub> S at 750°C: (1) first day exposure in pure H <sub>2</sub> S without polarization; (2) after 5 day operation without polarization; (3) after polarization for 20 min; Inset: expanded region 0-20 Ω·cm <sup>2</sup>	91
Figure 4-13	Reaction rate of H <sub>2</sub> as a function of cell current for a 5% H <sub>2</sub> S fuel stream at 800°C	94
Figure 4-14	Reaction rate of H <sub>2</sub> S as a function of current for a 5% H <sub>2</sub> S fuel stream at 800°C as well as the expected stoichiometric values	96
Figure 4-15	Comparison of SO <sub>2</sub> generation rate vs. current for a 5% H <sub>2</sub> S fuel stream at 800°C to calculated stoichiometric values	98
Figure 5-1	Configuration of modified H <sub>2</sub> S-air fuel cell with a glass holder	104
Figure 5-2	Relationship of current density to cell potential as a function of	107

	temperature after prolonged exposure time in pure H <sub>2</sub> S stream	
Figure 5-3	Equilibrium components in the system Pt/PtS/H <sub>2</sub> S as a function of temperature (HSC Chemistry, Version 1.12, Outokumpu Research)	109
Figure 5-4	Current-voltage curves for a H <sub>2</sub> S-air fuel cell at 700°C with pure H <sub>2</sub> S feed. Curve 1: after 1 h operation; Curve 2: after 6 h operation; Curve 3: after polarization of the cell in H <sub>2</sub> atmosphere	111
Figure 5-5	XRD spectra of Pt anode and YSZ surface after fuel cell test in pure H <sub>2</sub> S stream: (a) disconnected Pt anode cooled down without passing N <sub>2</sub> ; (b) anodic surface of YSZ after cooling down under N <sub>2</sub>	112
Figure 5-6	Cross-section SEM image of TiO <sub>2</sub> /YSZ interface (sealed in epoxy)	115
Figure 5-7	EDX measurement on the cross-section of YSZ wafer after fuel cell test in pure H <sub>2</sub> S stream, as a function of distance from the TiO <sub>2</sub> /YSZ interface: (a) d = 0 μm; (b) d = 1 μm; (c) d = 3 μm	117
Figure 5-8	Open circuit voltage of H <sub>2</sub> S-air fuel cell with TiO <sub>2</sub> interlayer as a function of air flow rate at 800°C. H <sub>2</sub> S (pure) flow rate: 15 mL/min	118
Figure 5-9	Cell Performance at 800°C as a function of air flow rate for the fuel cell arrangement: pure H <sub>2</sub> S, Pt/TiO <sub>2</sub> /YSZ/Pt, air. H <sub>2</sub> S flow rate: 15 mL/min	119
Figure 5-10	Current as a function of voltage for the fuel cell: pure H <sub>2</sub> S, Pt/TiO <sub>2</sub> (sol-gel)/YSZ/Pt, air. Flow rates: H <sub>2</sub> S, 25 mL/min; air, 75 mL/min	121
Figure 5-11	Current as a function of voltage for the fuel cell: pure H <sub>2</sub> S, Pt/TiO <sub>2</sub> (paste painting)/YSZ/Pt, air.	123

Flow rates: H<sub>2</sub>S, 25 mL/min; air, 75 mL/min

Figure 5-12 Stability of H<sub>2</sub>S-air fuel cell with TiO<sub>2</sub> interlayer at 750°C. 124

Flow rates: H<sub>2</sub>S, 15 mL/min; air, 75 mL/min

- Figure 6-1 (a) SEM image of anode catalyst after heat-treatment 133  
(back-scattering mode); (b) EDX spectrum of a typical catalyst particle in  
(a)
- Figure 6-2 Current-voltage curves for the fuel cell with CoMoO<sub>4</sub> as 138  
anode material in pure H<sub>2</sub>S atmosphere
- Figure 6-3 Comparison of current-voltage curves using MoS<sub>2</sub> and Pt 140  
as anodes at 800°C with and without IR correction
- Figure 6-4 Relationship of current density to power density for 141  
H<sub>2</sub>S-air fuel cells using MoS<sub>2</sub> and Pt as anodes at 800°C
- Figure 6-5 Relationship between current density and voltage using 144  
Fe-Mo-S as anode
- Figure 6-6 Impedance spectra for the cell using Fe-Mo-S as anode at 800°C 145
- Figure 6-7 Relationship between current density and power density 147  
for the cell using Fe-Mo-S as anode at 800°C and 850°C
- Figure 6-8 Current-voltage and current-power relationships of H<sub>2</sub>S-air 148  
fuel cell using Ni-Mo-S anode at 850°C
- Figure 6-9 The relationship between current density and cell voltage 150  
using Co-Mo-S anode at 800°C and 850°C
- Figure 6-10 Impedance spectra for the cell using Co-Mo-S anode 151

	at 800°C under different polarization conditions	
Figure 6-11	Impedance spectra for the cell using Co-Mo-S anode at different temperatures and polarization conditions	152
Figure 6-12	The relationship between current density and power density using Co-Mo-S anode at 800°C and 850°C	154
Figure 6-13	The relationship between current density and cell voltage at 750°C, 800°C and 850°C using (Co-Mo-S)+5%Ag as anode	156
Figure 6-14	The relationship between current density and power density at 750°C, 800°C and 850°C using (Co-Mo-S)+5%Ag as anode	158
Figure 6-15	Comparison of current-voltage and current-power relationships during the 1st and 5th day of operation at 800°C using (Co-Mo-S)+5%Ag as anode	160
Figure 6-16	Maximum current density and power density of H <sub>2</sub> S-air fuel cell as a function of time on stream at 850°C	161
Figure 6-17	Impedance spectra for the cell using (Co-Mo-S)+5%Ag as anode at different temperatures under open circuit conditions	162
Figure 6-18	Impedance spectra for the cell using (Co-Mo-S)+5%Ag as anode at different temperatures under polarization conditions	164
Figure 6-19	Impedance spectra of the (Co-Mo-S+5%Ag)/YSZ/Pt cell at OCV under the influence of an applied voltage at 750°C	166
Figure A-1	(a) TCD chromatograph of typical sulfur containing compounds separated using a packed column with Porapak Q packing and	179

(b) SCD chromatograph of the same sulfur-containing compounds separated using CP-Sil 5CB capillary column at a chosen temperature program shown in Table A-1

Figure A-2 TCD chromatograph of non-sulfur containing compounds 180  
separated using a packed column with Porapak R packing at a chosen temperature program shown in Table A-2

## Nomenclature

$C$	Concentration	$\text{mol/cm}^3$
$E_{cell}$	Cell voltage	V
$E_{ocv}$	Open circuit voltage	V
$F$	Faraday's constant (96,485 C/mol)	
$G$	Gibbs free energy	$\text{kJ/kmol}$
$H$	Enthalpy	$\text{kJ/kmol}$
$I$	Current	A
$i$	Current density	$\text{A/cm}^2$
$i_o$	Exchange current density	$\text{A/cm}^2$
$i_L$	Limiting current density	$\text{A/cm}^2$
$k$	Rate coefficient	1/s
$L_e$	Electrolyte thickness	cm
$n$	Number of electrons transferred	
$R$	Gas constant (8.314kJ/kg mol K)	
$R_e$	Area specific ohmic resistance of electrolyte	$\Omega\cdot\text{cm}^2$
$R_o$	Cell area specific ohmic resistance	$\Omega\cdot\text{cm}^2$
$R_t$	Total cell area specific resistance	$\Omega\cdot\text{cm}^2$
$r$	Reaction rate	$\text{mol/s}$
$P$	Pressure	Pa
$P_{cell}$	Power density	$\text{W/cm}^2$
$Q$	Heat energy	$\text{kJ/kmol}$

$S$	Entropy	kJ/kmol K
$T$	Temperature	K
$V$	Electrode potential	V
$v$	Flow rate	m <sup>3</sup> /s
$W$	Work energy	kJ/kmol
$X_o$	Initial composition percentage	
$X_i$	Composition percentage at current density of $i$	
$Z$	Impedance	$\Omega$

### Greek

$\alpha_a, \alpha_c$	Charge transfer coefficients	
$\Delta$	Overall change in thermodynamic property H, G and S.	
$\varepsilon$	Overall efficiency	
$\varepsilon_{th}$	Thermal efficiency	
$\varepsilon_v$	Voltage efficiency	
$\varepsilon_I$	Current efficiency	
$\eta_{act}$	Activation polarization	V
$\eta_{conc}$	Concentration polarization	V
$\eta_{ohm}$	Ohmic polarization	V
$\sigma_e$	Ionic conductivity of electrolyte	S/cm
$\omega$	Angular frequency	rad/s

### **Subscripts**

A, B	Reactant gases
a	Anode
b	Backward(reduction) reaction
C, D	Product gases
c	Cathode
f	Forward(oxidation) reaction
ox	Oxidized species
r	Reversible
red	Reduced species

### **Superscript**

a, b, c, d	Stoichiometric coefficients
o	Standard reference state

# CHAPTER 1

## INTRODUCTION

### 1.1 Introduction

Demand for electricity is increasing throughout the world, as a result of growth in world population and demands for improved standards of living for people in developing countries. Worldwide electricity consumption is expected to nearly double over the 1999-2020 period, despite growing concerns over the environmental impact of power generation. The most rapid growth in electricity use will be seen in developing Asia, where electricity consumption is expected to increase by 4.5% per year over the next two decades. Electricity consumption in the industrialized world is expected to grow at a more modest pace than in the developing nations, at 1.9% per year between 1999 and 2020 [1].

At its point of use, electricity is a clean, convenient and flexible energy. The dominant energy resources used to generate electricity in the world today are fossil fuels (natural gas, oil, coal), nuclear and hydropower [2]. However, no form of electricity generation is without its environmental effects or safety considerations. Although nuclear technology has no airborne pollutants or greenhouse gas emissions in power generation, the nuclear share of energy use for electricity production is expected to decline in many regions of the world as a result of operational safety concerns, waste disposal issues, concerns about nuclear-weapons proliferation, and less favorable economic environments [1,3]. In 2020, nuclear power is expected to account for about 12% of electrical power production worldwide, down from 16% in 1999 [1]. Hydroelectricity, as one of the most

extensively developed renewable energy sources in North America, is also characterized by the large variety of positive and negative effects it can have on the ecosystem [4]. Hydropower produces very few greenhouse gases and hydro projects often provide numerous societal benefits such as flood control, secure water supply and increased recreational opportunities. On the other hand, development of hydropower also creates serious adverse impacts on natural resources, such as reduced fish populations, detrimental changes in water quality and deforestation in the tropics. While at present hydropower supplies about 19% of the world's electricity, the growth in environmental concerns and the fact that most of the sites have already been exploited have slowed the development of hydroelectric power throughout the world and particularly in the United States. As a result, electricity generation in the future will continue to rely largely on combustion of fossil fuels, as it has for the past several decades. This will have the serious drawback of producing substantial amounts of air pollutants and CO<sub>2</sub>, and thus also contributing to global warming.

In 2020, fossil fuels are projected to account for 67% of world energy use for electricity production, slightly higher than 64% in 1999 [1]. Table 1-1 shows historical and anticipated global use of fossil fuels for electricity generation during the period of 1995-2020. High oil prices and energy security concerns have diminished the role of oil in the world's electricity generation markets. Coal will remain the dominant energy source to meet the increasing world electricity consumption for a long period of time, because it is relatively inexpensive, much more plentiful and more widely available than either oil or natural gas. However, reliance on coal for electricity generation is expected to be reduced in the short term by increments in natural-gas-fired generation. Among

**Table 1-1** Historical and projected global use of fossil fuels for electricity generation, 1995-2020  
(% of total energy consumption) [1]

<i>Fuel</i>	<i>1995</i>	<i>1999</i>	<i>2005</i>	<i>2010</i>	<i>2015</i>	<i>2020</i>
Oil	9.6%	9.54%	8.95%	8.99%	9.22%	9.36%
Natural Gas	17.7%	18.3%	20.4%	22.3%	24.7%	26.47%
Coal	36.6%	36.2%	35.35%	34.2%	32.65%	31.7%

fossil fuels, natural gas is the least environmentally harmful fuel in terms of both pollutants (SO<sub>2</sub>, NO<sub>x</sub>, volatile organic compounds, heavy metals, particulate matter) and CO<sub>2</sub> production. When natural gas is burnt to generate electricity, it produces 45% less CO<sub>2</sub> and other gases per billion Btu than coal does and 30% less than oil. Natural gas fired combined cycle generation units can be up to 60% energy efficient, whereas coal and oil generation units typically are only 30 to 35% efficient [5]. Electricity markets of the near future are expected to rely increasingly on natural gas fired generation. Worldwide, the use of natural gas for electricity supply is projected to double in the next 20 years, as technologies for gas-fired generation continue to improve and ample gas reserves are exploited [1].

As the primary energy source for electricity, fossil fuels have become essential to economic and social development, and thereby have greatly improved living standards around the world. However, the adverse impacts of fossil fuel combustion on environments and human health have also been tremendous [6]. A variety of air pollutants are formed when fossil fuels are burned to generate electricity. Some of the major pollutants released into the atmosphere include particulates, SO<sub>2</sub> and NO<sub>x</sub>, which contribute to acid rain. While technology improvements have been made to reduce emission of these traditional air pollutants, the most challenging problem associated with consumption of fossil fuels is enormous greenhouse gas emissions, since all methods for fossil-fueled electricity generation emit carbon dioxide. Higher levels of greenhouse gases are widely believed to contribute to significant warming of the earth. It has been estimated that continued use of fossil energy will lead to an increase of the average global temperature by 1.4-5.8°C over the next 100 years [7]. Global warming of this magnitude

would cause potentially disastrous changes in the environment, including more frequent hurricanes, expanding deserts and melting ice caps causing sea levels to rise and flood coastal regions.

In response to the threat of such global climate change and the critical need for environmentally friendly energy resources, some promising technologies have been developed or deployed to improve energy efficiency and reduce energy-related greenhouse gas emissions, especially CO<sub>2</sub> emissions [8]. Among them, fuel cells have attracted intense interest and development efforts as an alternative efficient and clean energy conversion technology that can make a significant contribution to transportation and stationary power generation in the near future.

## **1.2 Fuel Cells**

### **1.2.1 Fuel Cell Benefits and Development**

A fuel cell is an electrochemical device that converts the chemical energy of externally supplied fuel and oxidant directly to electrical energy. Fuel cells are similar in principle to primary batteries, except that they continuously produce power as long as fuel and oxidant are supplied and do not need to be recharged. By converting fuel directly to electricity, fuel cells can operate at much higher efficiencies than combustion-based power generations, thereby generating more electricity from the same amount of fuel. With efficiencies approaching 60%, even without cogeneration, fuel cell power plants are nearly one and half times as efficient as conventional power plants [9]. Cogeneration is the simultaneous production of electrical and thermal energy, which can raise the total efficiency of fuel cell power plants. For transportation applications, 40-50% efficiency

could be achieved using proton-exchange membrane fuel cells or solid oxide fuel cells, compared to 20-35% efficiency of internal combustion engines [10].

In addition to higher efficiencies, fuel cells possess several other generic characteristics which make them more favorable for future power generation when compared with devices based primarily on thermo-mechanical processes. Fuel cells contribute significantly to providing a cleaner environment: they produce dramatically fewer emissions of critical pollutants such as  $\text{NO}_x$ , and can reduce  $\text{CO}_2$  emissions by 20–60% through more efficient and cleaner energy conversion [11]. Because of their modular and distributed nature, fuel cells can be placed at or near load centers, resulting in savings in capital costs and operating efficiency of transmission lines and reducing the need for large power generation plants. Another advantage of the modular structure is that fuel cells can be easily scaled up or down in size, depending on local load demands. Fuel cells operate very quietly, and so they can be located indoors for domestic and commercial uses. Other advantages, such as energy security, low operating cost, variable or constant power production and fuel flexibility, also make fuel cells attractive as an alternative energy source of the future [12].

Since Sir William Grove first demonstrated the principle of operation of a fuel cell based on the reverse of water electrolysis [13], many attempts have been made to develop fuel cells for sustainable stationary, mobile and military applications [14,15]. Especially over the past two decades, stimulated by the worldwide environmental concerns and diminishing fossil fuel resources, billions of dollars have been spent and significant improvements have been achieved in the research and commercialization of fuel cell technology. Today, there are approximately 6,800 fuel cell units that have been

built and operated worldwide [16]. With reduced cost and technical breakthroughs, fuel cells could capture significant market shares in competition with conventional power generation technology. Across the world, the fuel cell market is expected to grow 18.7% per year and reach \$3.3 billion by 2008 from the present \$1.4 billion [17].

### 1.2.2 Types of Fuel Cells

A number of different types of fuel cells are being developed for a variety of potential applications. Based on the nature of the electrolyte used, fuel cells can be classified as five primary kinds: proton exchange membrane fuel cell (PEMFC), alkaline fuel cell (AFC), phosphoric acid fuel cell (PAFC), molten carbonate fuel cell (MCFC) and solid oxide fuel cell (SOFC). The main features and applications of each type are presented in Table 1-2.

These five types of fuel cells are at very different stages of development and commercialization. Each of them has advantages and disadvantages relative to the others. AFC was the first fuel cell technology to be put into practical service, and made the generation of electricity from hydrogen feasible [20]. AFCs were widely used in military and space applications because of their high energy-conversion efficiency and proven reliability. To date, the electric power on board the space shuttle still comes from AFCs [19]. Another attractive feature of AFCs is that a wide range of electrocatalysts can be used in the electrodes, including Ni, Ag, spinels, and metal oxides, as well as noble metals (*e.g.*, Pt) [21]. However, a major problem with AFC technology is that alkaline electrolytes adsorb CO<sub>2</sub> to form solid carbonate deposits, which eventually block active sites on the electrodes and reduce electrolyte conductivity. Therefore, it is necessary to

**Table 1-2** Essential characteristics of different types of fuel cells [10,18,19]

<i>Characteristic</i>	<i>Type of Fuel Cell</i>				
	PEMFC	AFC	PAFC	MCFC	SOFC
Electrolyte	Solid polymer	Potassium hydroxide (8-12 N)	Phosphoric acid (85%-100%)	Molten carbonates (Li, K, Na)	Solid oxide (ZrO <sub>2</sub> -Y <sub>2</sub> O <sub>3</sub> )
Operating Temperature	50-90°C	50-250°C	180-200°C	650°C	750-1050°C
Charge Carrier	H <sup>+</sup>	OH <sup>-</sup>	H <sup>+</sup>	CO <sub>3</sub> <sup>2-</sup>	O <sup>2-</sup>
Applications	Portable, transportation	Military, space	Power generation, cogeneration, transportation	Power generation, cogeneration	Power generation, cogeneration
Cell Efficiency	35-50%	35-55%	40%	>50%	>50%

operate AFCs on CO<sub>2</sub>-free fuel and oxidant, limiting the widespread application of AFC. The renaissance of this technology will depend on development of highly efficient and economical means to scrub CO<sub>2</sub>.

Emphasis on research and development in AFC technology has been reduced considerably during the past decade. Instead, recent advances have made PEMFC the most favorable fuel cell technology for low-temperature operations [22]. PEMFC displays an order of magnitude higher power density than any other fuel cell system, with the exception of the advanced aerospace AFC, which has comparable performance [23]. The significant improvements made in performance and design also offer the possibility of lower cost when compared with other types of fuel cells. PEMFCs contain a layer of solid polymer membrane as the electrolyte, which allows protons to be transmitted from the anode to the cathode. The use of a solid polymer electrolyte eliminates the corrosion and safety concerns associated with liquid electrolyte fuel cells. Its low operating temperature provides instant start-up and requires no thermal shielding to protect personnel [23]. PEMFC can operate on reformed hydrocarbon fuels and air without removing CO<sub>2</sub>, but the performance can be affected by CO. CO can poison the anode catalyst and reduce cell performance, at concentrations as low as 10 ppm. Since the membrane relies on the presence of liquid water to be able to conduct protons effectively, the reactant gases must be humidified to replace the water lost by evaporation from the membrane in order to keep the membrane hydrated. Therefore, water and heat management are crucial for a PEMFC to function properly.

PAFC is the most mature fuel cell technology in terms of system development and commercialization activities [23]. Phosphoric acid (H<sub>3</sub>PO<sub>4</sub>) is an excellent electrolyte

for fuel cells using reformed hydrocarbon fuels due to its tolerance to CO<sub>2</sub>. Concentrated H<sub>3</sub>PO<sub>4</sub> is a relatively stable acid, which allows operation at temperatures up to 200°C. The higher operating temperatures (150-200°C) reduce the complexity of power plants and make the co-generated heat more valuable [22]. The CO tolerance level of PAFC is about 1%-2%, much higher than that of PEMFC. In addition, the use of highly concentrated acid (close to 100%) minimizes the water vapor pressure, and so water management in PAFC is not difficult, unlike PEMFC [10]. One issue for PAFCs is that, if the source of its hydrogen fuel is reformed gasoline, sulfur must be removed from the fuel or it will damage the electrode catalyst. Another issue is that some acid may be entrained in the fuel or oxidant streams and replenishment of acid may be required after several hours' operation [23]. PAFC technology has been developed mainly for the medium-scale power generation market, and 200 KW demonstration units have been operated successfully for many thousands of hours. However, in comparison with the two low-temperature fuel cells, AFCs and PEMFCs, PAFCs achieve only moderate current densities [19].

As one of the high temperature fuel cells, MCFC can utilize hydrogen generated from a variety of fuels using either an internal or external reformer. It is also less prone to carbon monoxide "poisoning" than lower temperature fuel cells, which makes coal-based fuels more attractive for this type of fuel cell. MCFCs work well with catalysts made of relatively inexpensive nickel (Ni) and nickel oxide (NiO). MCFCs exhibit up to 60% efficiency, and this can rise to 80% if the waste heat is utilized for cogeneration. However, two major difficulties with molten carbonate technology put it at a disadvantage compared to SOFCs. One is the complexity of working with a liquid

electrolyte rather than a solid at the operating temperature of about 650°C. The other stems from the chemical reaction inside a molten carbonate cell. Carbonate ions from the electrolyte are consumed in reactions at the anode, making it necessary to compensate by injecting carbon dioxide at the cathode. In addition, the electrolyte used in molten carbonate fuel cells is highly corrosive, limiting some of its potential applications [23].

SOFCS are the only fuel cells that utilize a true solid electrolyte, and therefore electrolyte management problems that are common to other fuel cell types are not a concern with SOFCs [22]. SOFCs work at even higher temperatures than MCFCs, typically around 900-1000°C. However, a consequence of high-temperature operation is a slow startup, and the cell requires significant thermal shielding to retain heat and protect personnel. These features are acceptable for continuous utility applications, but not for transportation and small portable applications. The high operating temperatures also impose stringent durability requirements on cell materials. The development of low-cost materials with high durability at cell operating temperatures is the key technical challenge facing this technology. Substantial efforts are underway to explore the potential for developing lower-temperature SOFCs operating at or below 800°C that have fewer durability problems and cost less. However, decreasing the operating temperature generally results in a lower power density and stack materials that will function in this lower temperature range have not been identified [24]. In spite of these challenges, SOFC technology offers many advantages over other fuel cell technologies. The higher operating temperature allows direct internal reforming, promotes rapid electrocatalysis with non-precious metal catalysts, and produces high-grade waste heat for cogeneration or combined cycle applications. Efficiencies for this type of fuel cell can reach up to

70%, with an additional 20% available through heat recovery [25]. As in MCFC, CO is not a poison in SOFC and can be used directly as a fuel. SOFC is also the most sulfur-resistant fuel cell type; it can tolerate several orders of magnitude higher concentrations of sulfur than other fuel cells [23]. Because of the advantages of SOFC technology, a variety of fuels have been examined as potential fuel candidates in SOFCs, such as coal gas, gasoline, diesel fuel, jet fuel, alcohol, natural gas, hydrogen sulfide and ammonia.

### 1.3 Current Hydrogen Sulfide Removal Technology

One promising fuel candidate for SOFC is hydrogen sulfide. Hydrogen sulfide is a highly corrosive and toxic pollutant that is often present in natural gas at concentrations ranging from trace amounts to more than 80%. Many industrial operations, *e.g.* coking and hydrodesulfurization of crude oil and coal also produce hydrogen sulfide as an undesirable by-product. H<sub>2</sub>S production from hydrocarbon reserves is very large, over 20,000 tons per day in Western Canada alone. Because hydrogen sulfide has few industrial uses and is inherently dangerous, once it has been separated from other useful constituents of the gas mixture it is normally converted into a more useful form of sulfur. It can be burned to give sulfur dioxide and water and then converted into sulfuric acid. However, the product of choice is usually elemental sulfur, which is easier to transport than sulfuric acid [26].

The most commonly used method for the conversion of H<sub>2</sub>S to sulfur is the Claus process. Figure 1-1 shows the basic process scheme. A Claus sulfur recovery unit consists of a combustion furnace, waste heat boiler, sulfur condenser, and a series of catalytic stages each of which employs reheat, catalyst bed, and sulfur condenser [27].

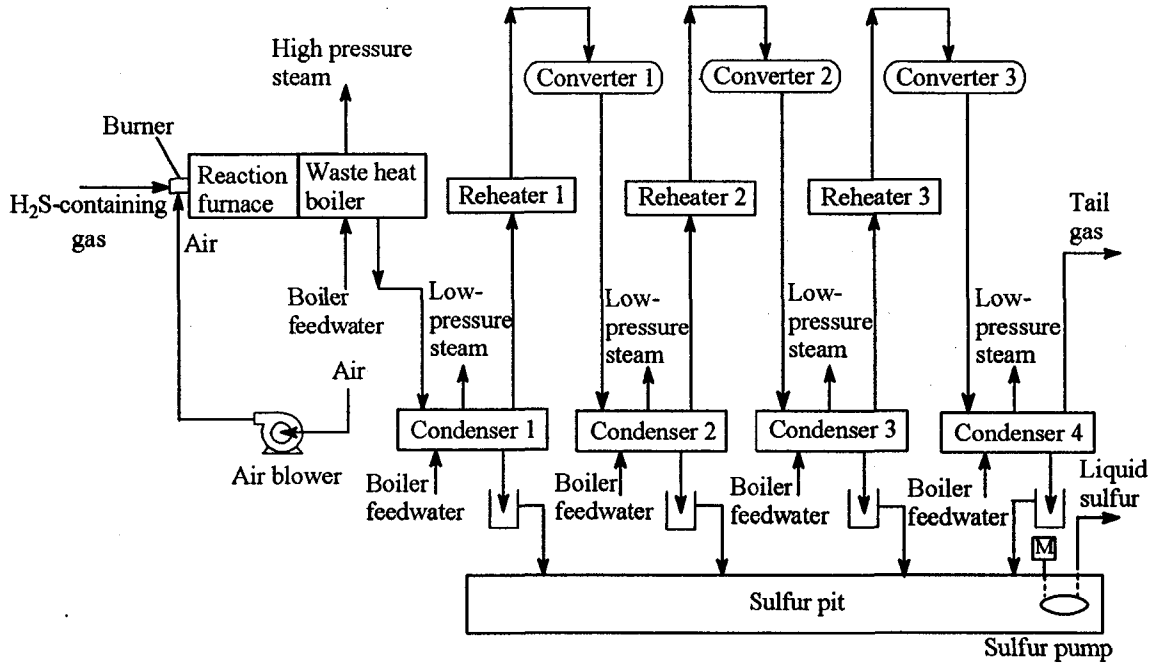


Figure 1-1 Schematic of a three-stage Claus process [26,27]

The chemical reactions to convert hydrogen sulfide to sulfur are carried out in the following two steps:



The first step is controlled combustion of the feed gas at high temperatures (1000-1400°C) to convert approximately one-third of the hydrogen sulfide to sulfur dioxide (Eq. 1-1) and non-catalytic reaction of unburned hydrogen sulfide with sulfur dioxide (Eq. 1-2). In the second step, hydrogen sulfide and sulfur dioxide react at low temperatures (200-350°C) over a catalyst to produce sulfur and water (Eq. 1-2) [27]. Typically, sulfur recoveries over 97% must be achieved. However, the recovery is highly dependent on the concentration of hydrogen sulfide and contaminants in the feed to the Claus unit. Due to its high operating costs, the Claus process is uneconomical when H<sub>2</sub>S concentrations in feed streams are lower than *ca.* 25 mol% [27].

As the sulfur in feed streams cannot be fully recovered via the Claus process, the tail gas, containing H<sub>2</sub>S, SO<sub>2</sub>, sulfur vapor and traces of other sulfur compounds, must be treated to remove these pollutants prior to venting to the atmosphere. As a result, a number of processes have been developed and applied to operation of the tail gas clean-up unit following the Claus unit to recover the residual sulfur. These processes can boost the overall sulfur recovery to up to 99% [27]. Nevertheless, the tail gas clean-up units can be rather costly; some can cost as much as or more than the Claus unit itself. Currently, the U.S. EPA regulations limit sulfur emissions from Claus sulfur recovery plants with capacity greater than 22.4 tons per day to 250 ppm on a dry, oxygen-free basis. This is comparable to an overall sulfur recovery of 99.8-99.9% [28]. As environmental policies

become increasingly stringent, higher capital and operating costs will be expected for treating effluent of Claus plants. Thus, the primary driver in current practice of H<sub>2</sub>S removal is not economic potential, but rather environmental regulations.

## **1.4 Fuel Cells for Conversion of Hydrogen Sulfide**

### **1.4.1 Benefits**

The conversion of H<sub>2</sub>S in the Claus process is highly exothermic, releasing a great deal of thermal energy, much of which can be recovered by generating steam. However, it is much more desirable to directly recover this energy as electricity. Advances in fuel cell technology provide promise as a way to utilize hydrogen sulfide as the fuel in a SOFC. Direct electrochemical conversion of H<sub>2</sub>S in SOFC will afford both economical and environmental benefits. The toxic pollutant H<sub>2</sub>S is destroyed. The SO<sub>2</sub> formed could be used either to produce sulfuric acid or to react with H<sub>2</sub>S to produce elemental sulfur, a salable product, using existing Claus technology. The energy of H<sub>2</sub>S oxidation is recovered as electrical power, a high-grade energy, with intrinsic high efficiencies of the SOFC. The electrical power generated could be used to operate Claus plants or other manufacturing facilities. A stack of SOFCs that utilize H<sub>2</sub>S as the fuel, coupled in series with Claus units or tail-gas clean-up units, could render cleaner effluent streams and improved economics for Claus plants. In addition, this hydrogen sulfide fuel cell technology would make it economically feasible to open some shut-in natural gas wells as the value of natural gas increases.

### 1.4.2 Objectives

The primary goal of this study is to investigate the potential use of H<sub>2</sub>S as fuel in SOFCs. H<sub>2</sub>S-powered SOFC differs from conventional H<sub>2</sub>-powered SOFC only on the anode side of the cell due to the different anodic reactions. Therefore, commonly used electrolytes such as YSZ and cathode materials such as LSM can be employed in SOFCs utilizing H<sub>2</sub>S as fuel. However, H<sub>2</sub>S has a disastrous effect on typical anode materials for SOFCs, resulting in severe degradation in cell performance. Intrinsically, suitable anode materials will be developed and examined that exhibit high electrocatalytic activity toward H<sub>2</sub>S oxidation and high stability in concentrated H<sub>2</sub>S streams. Successful development of active H<sub>2</sub>S-tolerant anode materials will have implications for use of other fuel cell feeds (e.g. hydrocarbon fuels containing H<sub>2</sub>S).

### References

- [1] Energy Information Administration (EIA), '*International Energy Outlook 2002*', Office of Integrated Analysis and Forecasting, U.S. Department of Energy, Washington, DC (2002).
- [2] International Energy Agency (IEA), '*Energy Technologies for the 21st Century*', Chapter 8, Organization for Economic Co-operation and Development (OECD), Paris, France (1997).
- [3] D. Bodansky, '*Nuclear Energy: Principles, Practices, and Prospects*', AIP Press, Woodbury, NY (1996).
- [4] G. W. Frey and D. M. Linke, *Energy Policy*, **30**, 1261 (2002).

- [5] Natural Gas Supply Association (NGSA), '*Natural Gas and the Environment* (<http://www.naturalgas.org/environment/naturalgas.asp>)', viewed 28 July 2003.
- [6] J. Colls, '*Air Pollution: An Introduction*', E & FN Spon, London, UK (1997).
- [7] IPCC, '*Climate Change 2001: the Scientific Basis, Contribution of Working Group I to the Third Assessment Report of the Intergovernmental Panel on Climate Change*', Cambridge University Press, Cambridge, UK and New York, NY, USA (2001).
- [8] IEA, '*Energy Technology and Climate Change: A Call to Action*', OECD, Paris, France (2000).
- [9] S. Rahman, '*Proceedings of the IEEE Power Engineering Society Transmission and Distribution Conference*, **1**, 551 (2001).
- [10] C. Song, '*Catalysis Today*, **77**, 17 (2002).
- [11] A. Bauen and D. Hart, '*Journal of Power Sources*, **86**, 482 (2000).
- [12] A. B. Stambouli and E. Traversa, '*Renewable and Sustainable Energy Reviews*, **6**, 297 (2002).
- [13] W. R. Grove, '*Philosophical Magazine and Journal of Science*, Ser. 3, **14**, 127 (1839).
- [14] K. Kordesch and G. Simader, '*Fuel Cells and Their Applications*', John Wiley & Sons, Inc., New York (1996).
- [15] J. Larminie and A. Dicks, '*Fuel Cell Systems Explained*', John Wiley & Sons, Inc., New York (2000).
- [16] M. Cropper, S. Geiger, D. Jollie, '*Fuel Cell Systems: A Survey of Worldwide Activity*', On-line publication (<http://www.fuelcelltoday.com/FuelCellToday>)

- /FCTFiles/FCTArticleFiles/Article\_696\_WorldWideSurvey1103.pdf), Johnson Matthey plc., 5 November 2003.
- [17] BCC, '*Fuel Cell Industry Review*', Business Communications Company, Inc., May 2003.
- [18] S. Srinivasan, R. Mosdale, P. Stevens and C. Yang, *Annual Review of Energy and the Environment*, **24**, 281 (1999)
- [19] G. Hoogers, '*Fuel Cell Technology Handbook*', Chapter 1, CRC Press LLC, Boca Raton, FL (2002).
- [20] G. F. McLean, T. Niet, S. Prince-Richard and N. Djilali, *International Journal of Hydrogen Energy*, **27**, 507 (2002).
- [21] J. H. Hirschenhofer, D. B. Stauffer, R. R. Engleman and M. G. Klett, '*Fuel Cell Handbook*', 4th ed., DOE/FETC-99/1076, U.S. Department of Energy, Federal Energy Technology Center, Morgantown, WV (1998).
- [22] M. L. Perry and T. F. Fuller, *Journal of the Electrochemical Society*, **149**, S59 (2002).
- [23] Renewable Energy Policy Project (REPP), '*Fuel Cells: A REPP Issue Brief*', On-line publication ([http://www.crest.org/hydrogen/hydrogen\\_fuelcell\\_intro.html](http://www.crest.org/hydrogen/hydrogen_fuelcell_intro.html)), October 2002.
- [24] Office of Energy Efficiency and Renewable Energy (EERE), '*Fuel Cells*', On-line publication (<http://www.eere.energy.gov/hydrogenandfuelcells/fuelcells>), Hydrogen, Fuel Cells and Infrastructure Technologies Program, U. S. Department of Energy, viewed 5 August 2003.

- [25] A. B. Stambouli and E. Traversa, *Renewable and Sustainable Energy Reviews*, **6**, 433 (2002).
- [26] W. Nehb and K. Vydra, Chapter 6, "Sulfur", '*Ullmann's Encyclopedia of Industrial Chemistry (Online)*', 6th Ed, Wiley-VCH Verlag GmbH & Co. KGaA (2002).
- [27] M. Capone, Chapter 2, "Sulfur Removal and Recovery", '*Kirk-Othmer Encyclopedia of Chemical Technology (Online)*', 4th Ed, John Wiley & Sons, Inc., (1997).
- [28] EPA, '*Compilation of Air Pollutant Emission Factors*', AP-42, Fifth Edition, Volume I: Stationary Point and Area Sources, U.S. Environmental Protection Agency, Research Triangle Park, NC (1995).

# CHAPTER 2

## PRINCIPLES OF FUEL CELLS

### 2.1 Introduction

As early as 1839, Sir William Grove discovered the basic operating principle of fuel cells by reversing water electrolysis to generate electricity from the reactions of hydrogen and oxygen at separate electrodes [1,2]. All types of fuel cells developed since then are based on the same principle that he discovered. Fuel cells are highly efficient, environmentally friendly power-generating systems that produce electrical energy by combining fuel and oxidant electrochemically. Generally, a fuel cell consists of a positive and a negative electrode separated by an electrolyte that transfers ions but not electrons. When the two electrodes are connected through an external load, electrochemical reactions occurring at the anode and cathode and the transport of ions in the electrolyte spontaneously produce direct-current electricity through the flow of electrons. Unlike batteries that store reactants internally, a fuel cell is only an energy conversion device; it does not need recharging, and continuously produces power as long as external fuel and oxidant are supplied. Although fuel cells bear similarities to heat engines in terms of continuous consumption of fuel and generation of electricity, they are considerably different regarding the energy conversion process. Operation of a heat engine involves multiple processes of energy transformation between a high temperature source from a combustion process and a low temperature sink. The limit of its efficiency is determined by the Carnot cycle. In contrast, a fuel cell can operate isothermally at a given

temperature [3]. In addition, lack of combustion irreversibility makes fuel cells more efficient than heat engines [4].

## 2.2 Fuel Cell Thermodynamics

### 2.2.1 Theoretical Reversible Potential

As in any other energy converter, the energy conversion process in fuel cells is governed by the First and Second Laws of Thermodynamics. The First Law states that the energy of a system is conserved, which can be expressed as follows [5]:

$$Q - W = \Delta H \quad (2-1)$$

The above relationship is suitable for a stationary control volume under steady-flow conditions, representing the case of a fuel cell. The Second Law of Thermodynamics defines entropy as a measure of the disorder in a system. A process in which there is no entropy generation is called a reversible process. In a reversible process, both the system and its surroundings can be returned to their original states at any point. If a reversible heat transfer is carried out at a constant temperature in a system, the entropy change corresponding to the amount of heat transferred is given by Eq. (2-2) [5]:

$$Q = T\Delta S \quad (2-2)$$

Since the reaction in a fuel cell occurs electrochemically, the work is done by the movement of electrons, which is driven by the electrical potential difference  $E_r$  between anode and cathode. If one component of the overall reaction involves transfer of  $n$  electrons, the maximum electrical work that can be done is

$$W = nFE_r \quad (2-3)$$

where  $F$  is Faraday's constant (96,485 C/mol).

Substituting Eqs. (2-2) and (2-3) into (2-1):

$$\Delta H = T\Delta S - nFE_r \quad (2-4)$$

For a chemical reaction at constant temperature, the enthalpy change is related to the Gibbs free energy change  $\Delta G$  by the following equation [5]:

$$\Delta G = \Delta H - T\Delta S \quad (2-5)$$

in which  $\Delta G$  is a measure of the maximum useful or available work that can be obtained from the reaction. It should be noted that for most fuel cell reactions,  $\Delta S$  is negative, signifying that some heat is released to the surroundings [6]. As a result, even in a reversible (ideal) fuel cell, there is a portion of heat  $T\Delta S$  that cannot be converted to electrical energy.

By comparison of Eq. (2-4) with Eq.(2-5), we see that:

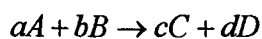
$$\Delta G = -nFE_r \quad (2-6)$$

Eq. (2-6) is applicable to a fuel cell operating reversibly and isothermally at constant pressure. The Gibbs free energy is a state function and varies with temperature and pressure. If the reactants and products are all in their standard states, Eq. (2-6) becomes

$$\Delta G^\circ = -nFE_r^\circ \quad (2-7)$$

where  $E_r^\circ$  is the standard thermodynamic reversible potential of the cell.

For a chemical reaction occurring at constant temperature and pressure, in which the gaseous reactants A and B form gaseous products C and B,



the free energy change  $\Delta G$  of the reaction can be related to the standard reference state  $\Delta G^\circ$  by Eq. (2-8):

$$\Delta G = \Delta G^\circ + RT \ln \frac{P_C^c P_D^d}{P_A^a P_B^b} \quad (2-8)$$

Substitution of Eqs. (2-6) and (2-7) into (2-8) gives:

$$-nFE_r = -nFE_r^\circ + RT \ln \frac{P_C^c P_D^d}{P_A^a P_B^b} \quad (2-9)$$

where  $P$  is the partial pressure of each reactant or product gas.

Dividing Eq. (2-9) by  $(-nF)$  gives the *Nernst Equation*:

$$E_r = E_r^\circ - \frac{RT}{nF} \ln \frac{P_C^c P_D^d}{P_A^a P_B^b} \quad (2-10)$$

The Nernst equation allows the thermodynamic reversible potential  $E_r$  of a fuel cell to be calculated at various temperatures and partial pressures of reactants and products with reference to the standard cell voltage  $E_r^\circ$ .

### 2.2.2 Fuel Cell Efficiencies

Based on the First Law, the thermal efficiency of an energy conversion device is defined as the net work output divided by the heat input. The total thermal energy change of a reaction is provided by the enthalpy change  $\Delta H$  between the reactants and products. In a fuel cell working ideally, all the free energy change  $\Delta G$  may be completely and directly converted to electrical energy; thus the maximum thermal efficiency of the cell is expressed by the equation [7]:

$$\varepsilon_{th} = \frac{\Delta G}{\Delta H} = 1 - \frac{T\Delta S}{\Delta H} = \frac{-nFE_r}{\Delta H} \quad (2-11)$$

For most fuel cell reactions at ordinary temperature, the value of  $\varepsilon_{th}$  is typically greater than 90% [6]. However, in reality, fuel cells can never approach ideal efficiencies due to

some irreversible losses, which are expressed as the voltage efficiency and Faradaic efficiency.

The voltage efficiency is defined as

$$\varepsilon_V = \frac{E_{cell}}{E_r} \quad (2-12)$$

When a current is drawn from a practical fuel cell, the actual cell voltage  $E_{cell}$  falls from the thermodynamic reversible voltage  $E_r$  and decreases with increasing cell current output until a limiting value of current is reached. There are three main factors that cause the departure of  $E_{cell}$  from  $E_r$ : activation polarization, concentration polarization and ohmic polarization. These phenomena will be described in Section 2.3. The difference between the reversible and the real electrical energy produced by a fuel cell, which is given by  $nF(E_r - E_{cell})$ , is lost as heat to the surroundings because of the polarizations within the cell.

Another type of efficiency loss in a fuel cell occurs when some of the chemical energy of the fuel is not converted to electrical energy. Such losses are attributable to four causes: crossover of the fuel to the cathode (or oxidant to the anode) where it is consumed through a direct chemical reaction rather than producing any electrons; passing some of the fuel through the fuel cell unreacted; chemical side-reactions of either fuel or oxidant, catalyzed by electrodes; or undesirable incomplete electrochemical oxidation of the fuel [8]. This type of loss is accounted for by the current efficiency,  $\varepsilon_I$ , also termed Faradaic efficiency, which is given by [9]:

$$\varepsilon_I = \frac{I}{-nFN_{fuel}} = \frac{1}{fuel\ stoichiometry} \quad (2-13)$$

where  $I$  is the actual current generated in the cell and  $N_{fuel}$  is the flow rate of fuel. The inverse of  $\varepsilon_I$  is termed the “fuel stoichiometry”, which is the amount of fuel fed to the cell compared to amount the cell requires to provide the electrons demanded.

The overall cell efficiency  $\varepsilon$  of a fuel cell is the product of these three efficiencies:

$$\varepsilon = \varepsilon_{th} \varepsilon_V \varepsilon_I \quad (2-14)$$

Since  $\varepsilon_{th}$  is a thermodynamically defined quantity and  $\varepsilon_I$  is very close to unity for most practical fuel cell systems, a main goal of fuel cell research is to improve the value of voltage efficiency, i.e., reduce parasitic losses due to the irreversibilities of fuel cell processes.

### 2.3 Fuel Cell Polarization and Current-Potential Relationships

As stated above, to maximize the fuel cell efficiency it is imperative to reduce the cell voltage losses. In an ideal fuel cell, the cell voltage would remain constant ( $E_r$ ) as different amounts of current were drawn from the cell. However, when a current is flowing through a practical fuel cell, the cell voltage falls due to consequent polarizations. The higher the current, the greater the voltage drop. Three distinct types of polarization contribute to voltage losses: activation, concentration and ohmic polarization. Activation polarization ( $\eta_{act}$ ) is caused by the slow charge transfer process across the electrode-electrolyte interface. Concentration polarization ( $\eta_{conc}$ ) is often related to the transport resistance of reactants/products to/from the electrochemical reaction sites at the electrode-electrolyte interface. Ohmic polarization ( $\eta_{ohm}$ ) is mainly due to the electrical resistance of various cell components.

In fuel cells, activation and concentration polarization can exist at both anode and cathode. The total polarization at these electrodes is the sum of the two terms:

$$\eta_a = \eta_{act,a} + \eta_{conc,a} \quad (2-15)$$

and

$$\eta_c = \eta_{act,c} + \eta_{conc,c} \quad (2-16)$$

where  $\eta_a$  and  $\eta_c$  represent anode and cathode polarization, respectively.

The effect of polarization is to shift the anode potential positively and the cathode potential negatively. Thus, the electrode potentials at anode and cathode can be expressed as:

$$V_a = V_{r,a} + \eta_a \quad (2-17)$$

and

$$V_c = V_{r,c} - \eta_c \quad (2-18)$$

where  $V_{r,a}$  and  $V_{r,c}$  are the corresponding reversible potentials for anode and cathode.

The overall cell potential includes the contribution of anode and cathode potentials and ohmic polarization:

$$E_{cell} = V_c - V_a - \eta_{ohm} \quad (2-19)$$

Substituting Eqs. (2-17) and (2-18) into Eq. (2-19), it follows that

$$E_{cell} = E_r - \eta_a - \eta_c - \eta_{ohm} \quad (2-20)$$

where  $E_r$  is given by  $(V_{r,c} - V_{r,a})$ .

Use of Eqs. (2-15) and (2-16) in Eq. (2-20) yields:

$$E_{cell} = E_r - \eta_{act,a} - \eta_{act,c} - \eta_{conc,a} - \eta_{conc,c} - \eta_{ohm} \quad (2-21)$$

However, in practical fuel cells, cell voltage at zero current is often lower than the reversible value  $E_r$  due to low but unavoidable crossover of fuels or side-reactions. Therefore, in most cases,  $E_r$  in Eq. (2-21) is replaced by the open circuit potential,  $E_{ocv}$ . Figure 2-1 shows a typical plot of the cell potential as a function of current for fuel cells, indicating the regions dominated by each type of polarization.

### 2.3.1 Activation Polarization

As shown in Figure 2-1, activation polarization is responsible for the initial semi-exponential drop in voltage in the low current region. It arises from slow electrocatalytic (electron transfer) reactions across the phase boundary between the electronically conducting electrode and ionically conducting electrolyte. Similar to chemical reactions in which the reactants must overcome an activation energy barrier, electrochemical reactions involve a potential energy barrier that must be overcome by the reacting species. Therefore, a portion of cell potential is lost in reducing the energy barrier so that the charge transfer reactions at both electrodes can proceed. Activation polarization may be reduced by increasing temperature and using suitable electrocatalysts.

For a single rate-determining reaction, the relationship between the activation overpotential and the current density is normally expressed by the Butler-Volmer equation [10]:

$$i = i_o \left[ \exp\left(\alpha_a \frac{nF\eta_{act,a}}{RT}\right) - \exp\left(-\alpha_c \frac{nF\eta_{act,a}}{RT}\right) \right] \quad (2-22a)$$

for the anode or

$$i = i_o \left[ \exp\left(\alpha_c \frac{nF\eta_{act,c}}{RT}\right) - \exp\left(-\alpha_a \frac{nF\eta_{act,c}}{RT}\right) \right] \quad (2-22b)$$

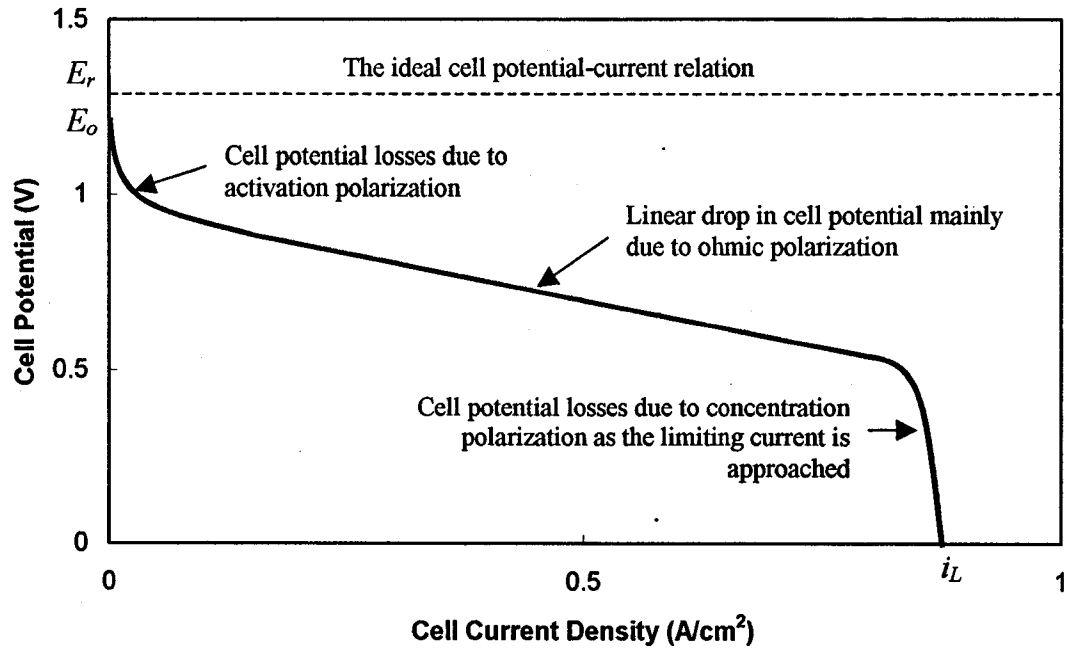


**Figure 2-1** Typical relationship of cell potential to current for fuel cells, showing which regions are controlled by various types of polarization [7]

for the cathode, where  $\alpha_a$  and  $\alpha_c$  are the anodic and cathodic charge transfer coefficients, respectively, and  $\alpha_a + \alpha_c = 1$  ( $0 \leq \alpha_a \leq 1, 0 \leq \alpha_c \leq 1$ );  $\eta_{act}$  is always positive, as defined in Eqs. (2-15) and (2-16).

The charge transfer coefficients represent the fraction of the applied overpotential  $\eta_{act}$  used to drive the anodic or cathodic reaction and are a measure of the symmetry of the corresponding energy barrier. The exchange current density  $i_o$  is the current flowing equally in both directions at the equilibrium potential, which is defined in Eq. (2-23) [9]:

$$i_o \equiv nFk_f C_{ox} = nFk_b C_{red} \quad (2-23)$$

As can be seen from Eq. (2-23), exchange current densities are concentration-dependent. However, the variation of  $i_o$  with concentration is usually not as significant as its dependence on temperature. In addition, it has been shown that, in a SOFC system, the exchange current density may also be affected by other factors, including the electrode microstructure and the ionic conductivity of the electrolyte [11,12]. Because the exchange current density incorporates the kinetic terms  $k_f$  and  $k_b$  that include the chemical portion of the electrochemical free energy of activation, it can be used to compare the activities of different electrocatalysts: the smaller the activation energy, the larger the  $i_o$  value, and therefore the better the performance of the catalyst [9].

There are two limiting cases of the Butler-Volmer equation that are often used in practical work. At low activation polarizations ( $\eta_{act} \ll RT/anF$ ), the exponential terms in Eq. (2-22) can be expanded in a Taylor-MacClaurin series [13]. Neglecting the terms higher than the linear terms gives:

$$\eta_{act} = \frac{RT}{nF} \ln \frac{i}{i_o} \quad (2-24)$$

Thus, the exchange current density may be estimated from a plot of  $i$  vs.  $\eta_{act}$  in the low polarization region.

Under high activation polarization, the second exponential term in the Butler-Volmer equation becomes negligible. The resulting Tafel equation [7] is expressed as:

$$\eta_{act,a} = -\frac{RT}{\alpha_a nF} \ln i_o + \frac{RT}{\alpha_a nF} \ln i \quad (2-25a)$$

or

$$\eta_{act,c} = -\frac{RT}{\alpha_c nF} \ln i_o + \frac{RT}{\alpha_c nF} \ln i \quad (2-25b)$$

Assuming  $i_o$ ,  $\alpha_a$  and  $\alpha_c$  are constant for a given reaction and temperature, the Tafel equation can be written as:

$$\eta_{act} = a + b \log i \quad (2-26)$$

which allows estimation of exchange current density and transfer coefficients from the intercept and slope of a  $\log i \sim \eta_{act}$  plot.

### 2.3.2 Ohmic Polarization

The pseudo-linear portion in Figure 2-1 corresponds to an intermediate current density region in which the decrease in cell voltage with increase of current density is dominated by ohmic polarization. Ohmic losses arise because of the transport resistance of ions flowing through the electrolyte, and of electrons moving through the electrode materials and terminal connections. This type of voltage loss obeys Ohm's law and can be expressed by the equation:

$$\eta_{ohm} = iR_o \quad (2-27)$$

where  $R_o$  is the total cell ohmic resistance, including electronic, ionic and contact resistance. In order to minimize ohmic polarization, it is necessary to use thin, highly ionic conductive electrolytes, to choose highly electric conductive electrodes, and to improve the contact of electrodes with electrolytes and current collectors. In SOFCs, a portion of cell ohmic resistance stems from electrolyte resistance, which is given by:

$$R_e = \frac{L_e}{\sigma_e} \quad (2-28)$$

Thus, cell designs having anode or cathode supported ultra-thin electrolyte layers have been developed to reduce ohmic resistance.

### 2.3.3 Concentration Polarization

Concentration polarization is encountered at very high current densities, when the mass transport of gaseous species through electrodes or the supply of  $O^{2-}$  through the electrolyte becomes limiting. As the reactants in the electrode-electrolyte interfaces are consumed at high rates, the species concentrations at the reaction sites (normally three-phase boundaries) are lower than in the bulk supply. Hence, concentration gradients across electrodes are built up, leading to a corresponding loss in output voltage. Several processes may contribute to concentration polarization, including slow transport of gases in the electrode pores, limited diffusion of reactants to the electrochemical reaction sites, and over-accumulation of products near the surface of electrodes. Concentration polarization can be reduced by increasing gas pressures, appropriate design of anode and cathode compartments, use of porous and thinner electrodes and optimization of

electrode-electrolyte interfaces. Eq. (2-29) gives an expression for concentration polarization, which can be used for either anode or cathode [14]:

$$\eta_{conc} = -\frac{RT}{nF} \ln\left(1 - \frac{i}{i_L}\right) \quad (2-29)$$

The limiting current density  $i_L$  occurs when the reactant concentration at the surface of electrode is zero. It is a measure of the maximum rate at which a reactant can be supplied to an electrode. The value of  $i_L$  is mainly affected by the microstructures of electrodes, such as porosity, permeability, pore size and tortuosity, and electrode-electrolyte interfaces. As this current limitation is approached, the cell potential drops off dramatically, as seen for the high current density region in Figure 2-1. Whether or not the limiting current will be reached in the operation of a fuel cell largely depends on the magnitude of ohmic and activation polarization.

## 2.4 Power Characteristics

As seen in earlier sections, the various cell polarizations may be expressed in terms of the current density drawn from the cell. The cell potential-current density relation is the most essential one for a fuel cell, from which the characteristics of voltage efficiency and power density for the cell can be derived. The variation of voltage efficiency with current density is proportional to that of cell potential, as given by Eq. (2-12). The electrical power density,  $P$ , generated by a fuel cell is the product of cell voltage and current density:

$$P_{cell} = iE_{cell} \quad (2-30)$$

Plots of voltage efficiency and power density as functions of current density are shown in Figure 2-2. The voltage efficiency decreases monotonously with increasing current density. However, the power density vs. current density curve is highlighted by an apex. When no current is drawn from the cell, no power is produced. The power initially increases with increasing current density, then passes through a maximum and finally decreases to zero when cell potential reaches zero. When concentration polarization dominates cell performance, the maximum power density occurs near the limiting current, as displayed in Figure 2-2. However, if cell ohmic resistance or activation polarization is sufficiently high that the cell voltage approaches zero before the limiting current is reached, the power curve tends to be parabolic and the maximum power density occurs at about half of the open circuit potential.

Operating a fuel cell at maximum power is usually not desirable in most applications. As seen in Figure 2-2, the highest power output corresponds to a fairly low cell efficiency. Optimizing the operating point of a fuel cell always involves some trade-offs between cell efficiency and maximum power density. In stationary applications, fuel efficiency is of primary importance. Consequently, cell power output has to be shifted to higher cell potentials, and thus to lower power densities.

## **2.5 Electrochemical Impedance Spectroscopy**

Electrochemical impedance spectroscopy (EIS) is a powerful technique for characterization of solid oxide fuel cells. It has been widely used to measure the bulk and grain boundary resistance of solid electrolytes [15,16] and to investigate various physicochemical processes at electrode-electrolyte interfaces [17]. Moreover, EIS can

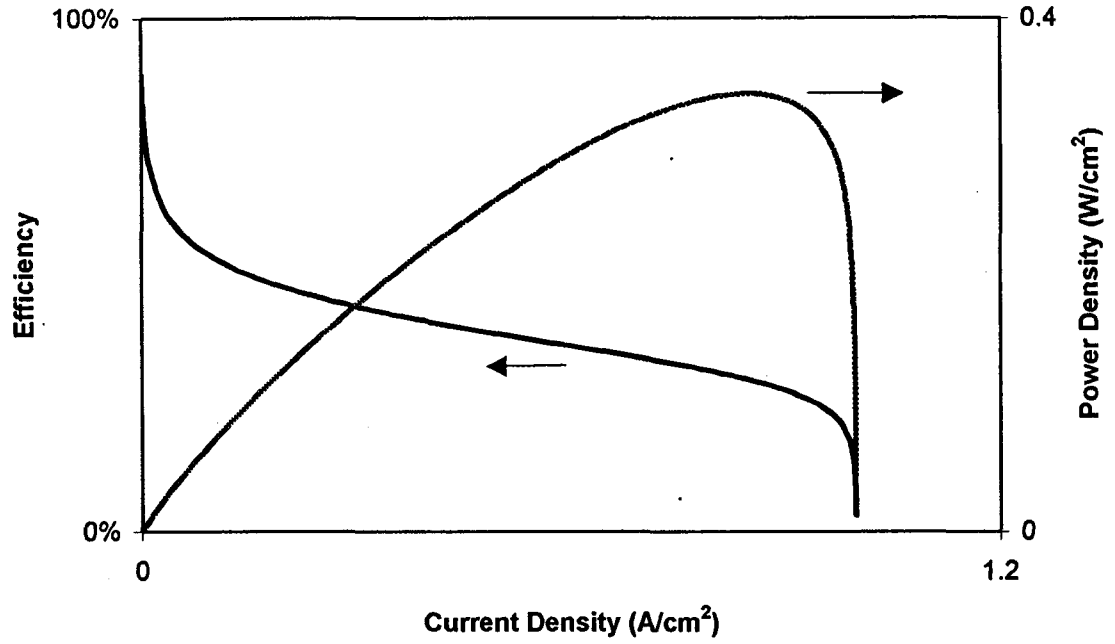


**Figure 2-2** Typical cell efficiency and power density vs. current density plots

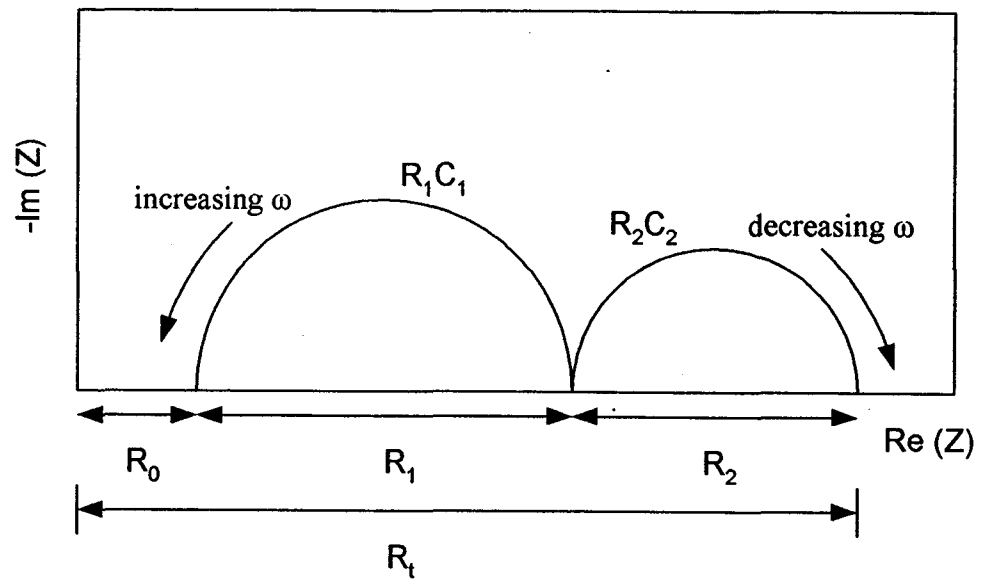
provide valuable information for effective improvement of overall cell performance by distinguishing the contributions of each component or process to the internal resistance of a fuel cell.

The fundamentals of EIS rely on the fact that by applying a small alternating potential of a given frequency  $\omega$  across an electrochemical cell, the current response is measured and then the complex impedance  $Z(\omega)$  can be determined based on the acquired information. This procedure is repeated over a wide range of frequencies so that a series of  $Z(\omega)$  data are obtained. The expression for  $Z(\omega)$  is composed of a real and an imaginary part [18]:

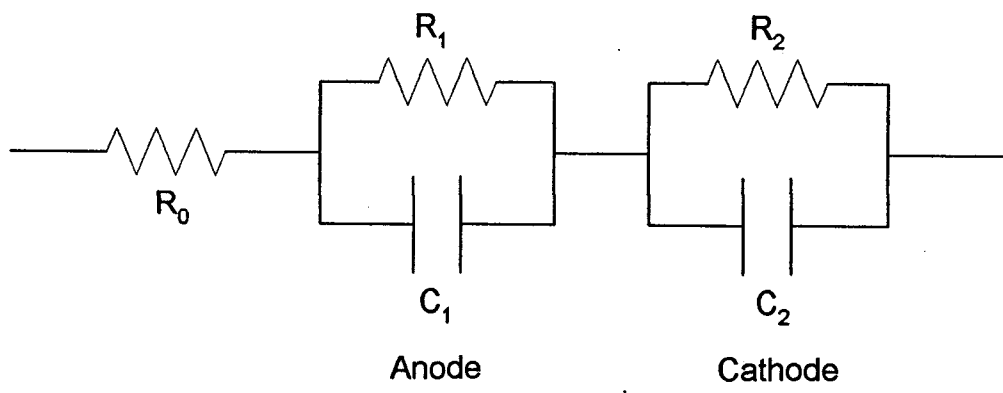
$$Z(\omega) = \text{Re}\{Z(\omega)\} + j \text{Im}\{Z(\omega)\} \quad (2-31)$$

where  $j = \sqrt{-1}$ .

Plotting the imaginary impedance (Y axis) against the real impedance (X axis) in a complex plane at different frequencies generates a Nyquist plot. Nyquist plots are particularly useful for the characterization of dynamic processes. Based on the impedance spectrum, the behavior of various processes in an electrochemical system can be modeled using an equivalent circuit consisting of electrical elements like resistors, capacitors and inductors in parallel or series arrangements. Figure 2-3 gives a simple impedance diagram of a fuel cell system and its simulated equivalent circuit.  $R_t$  represents the total cell resistance. The resistance  $R_o$  can be attributed to the ohmic losses in electrolytes, leads and contacts. Each parallel connection of a resistor and a capacitor (RC) is related to a simple electrode polarization process. The resistance  $R_1$  or  $R_2$  represents the total polarization loss of anode or cathode, while the capacitance  $C_1$  or  $C_2$  corresponds to the charge double layer or adsorption occurring at each electrode surface. In general, in a



(a)



(b)

**Figure 2-3** (a) An impedance spectrum and (b) simplified equivalent circuit for a fuel cell

complex plane plot, processes that usually manifest themselves as semicircles with time constants directly corresponding to the peak frequency of the semicircle can be interpreted in terms of a RC circuit [18].

In Figure 2-3, the impedance plot shows a full semicircle with respect to each RC circuit. However, in real fuel cell systems, experimentally obtained spectra often contain depressed or distorted semicircular arcs. This can be attributed either to Warburg diffusion processes connected with different concentrations of electroactive species in the system or to the variation of cell parameters (temperature, gas composition, electrical current and interface morphology) with position in the electrode/electrolyte interface plane or within the electrolyte, resulting in the changes of resistances and capacitances [18]. For such cases, a constant-phase element  $Q$  is used instead of the capacitance.

In practice, several physicochemical processes in fuel cells may proceed in parallel, and the difference of their time constants may not be sufficiently high. As a result, multiple, overlapping arcs are often observed from the Nyquist plot. In such circumstances, appropriate data analysis techniques have to be used in order to identify the dynamic processes and estimate the parameter values of the corresponding equivalent circuit elements, which involve choosing empirical equivalent circuits based on physical assumptions and conducting numerical fit procedures. However, the interpretation of impedance spectra based on equivalent circuits and subsequent curve fitting can be ambiguous without a physical meaning assigned to each circuit element or due to the high complexity of the systems and inadequate interpretation techniques [18]. In most cases for this project, EIS was utilized to characterize the overall behavior of the fuel cell systems under investigation, without the modeling of equivalent circuits. One cell

parameter (current, operating temperature, etc.) is varied from measurement to measurement while others are kept constant. A series of impedance spectra are then plotted as Nyquist-plot in the same complex plane. By comparing the changes of total cell resistance, cell ohmic resistance and cell polarization resistance against the varied parameter, individual processes contributing to the intrinsic loss of fuel cell operation could be distinguished and useful information on the prediction and optimization of fuel cell performance could be obtained.

## References

- [1] W. R. Grove, *Philosophical Magazine and Journal of Science*, Ser. 3, **14**, 127 (1839).
- [2] G. Hoogers, '*Fuel Cell Technology Handbook*', Chapter 1, CRC Press LLC, Boca Raton, FL (2002).
- [3] X. Li, *International Journal of Global Energy Issues*, **17**, 68 (2002).
- [4] C. Haynes, *Journal of Power Sources*, **92**, 199 (2001).
- [5] J. R. Howell and R. O. Buckius, '*Fundamentals of Engineering Thermodynamics*', McGraw-Hill Book Co., New York (1987).
- [6] A. J. Appleby and F. R. Foulkes, '*Fuel Cell Handbook*', Chapter 2, Van Nostrand Reinhold, New York (1989).
- [7] J. O'M. Bockris and S. Srinivasan., '*Fuel Cells: Their Electrochemistry*', McGraw-Hill Book Co., New York (1969).
- [8] S. Srinivasan, R. Mosdale, P. Stevens and C. Yang, *Annual Review of Energy and the Environment*, **24**, 281 (1999).

- [9] E. Chen, *Fuel Cell Technology Handbook*, Chapter 3, CRC Press LLC, Boca Raton, FL (2002).
- [10] A. J. Bard and L. R. Faulkner, *Electrochemical Methods: Fundamental and Applications*, John Wiley & Sons Ltd., New York (2001).
- [11] H. Zhu and R. J. Kee, *Journal of Power Sources*, **117**, 61 (2003).
- [12] H. Uchida, M. Yoshida and M. Watanabe, *Journal of the Electrochemical Society*, **146**, 1 (1999).
- [13] S. H. Chan, K. A. Khor and Z. T. Xia, *Journal of Power Sources*, **93**, 130 (2001).
- [14] J. H. Hirschenhofer, D. B. Stauffer, R. R. Engleman and M. G. Klett, *Fuel Cell Handbook*, Chapter 2, 4th ed., DOE/FETC-99/1076, U.S. Department of Energy, Federal Energy Technology Center, Morgantown, WV (1998).
- [15] J. Van Herle, A. J. McEvoy and K. R. Thampi, *Journal of Materials Science*, **29**, 3691 (1994).
- [16] J. R. MacDonald, *Impedance Spectroscopy: Emphasizing Solid Materials and Systems*, Wiley Interscience, New York (1987).
- [17] V. Stancovski, S. Sridhar and U. B. Pal, *Journal of Electroceramics*, **3**, 279 (1999).
- [18] E. Ivers-Tiffée, A. Weber and H. Schichlein, *Handbook of Fuel Cells*, Vol. 2, Part 3, John Wiley & Sons Ltd., West Sussex, England (2003).

# CHAPTER 3

## LITERATURE REVIEW

### 3.1 Structure and Operation of Solid Oxide Fuel Cells

Solid oxide fuel cells (SOFCs) have attracted substantial interest in recent years primarily due to their high efficiency and versatility as alternative clean power generation systems. Electrical efficiencies up to 50% and overall efficiencies about 70-90% (including thermal power) can be achieved for small stationary SOFC units in the power range 1-100 kW, and electrical efficiencies approaching 70% are expected for larger pressurized SOFC/gas-turbine systems in the 1 MW-range [1]. The high efficiency of SOFCs results in less fuel being consumed to produce a given amount of electricity, which thereby contributes to significant reduction in pollution and emission of greenhouse gases [2]. While the main application of SOFCs is currently focused on the field of stationary power generation, a reduction in operating temperatures to 600°C would enable potential applications of small-scale SOFC systems in the area of transportation, in particular as auxiliary power units (APU) in electric vehicles [3].

SOFCs are composed of all-solid-state materials. This solid-state construction not only eliminates many problems associated with catalyst wetting, electrode flooding and electrolyte migration that are common to other types of fuel cells, but also allows for a wide variety of designs and operating procedures. Two main types of SOFC configuration are being developed at present: tubular and planar cells [4]. Both designs have advantages and disadvantages. Tubular configuration avoids the need for high

temperature seals, but requires relatively expensive fabrication techniques and results in low volumetric power densities. In contrast, recent designs using planar or flat plate cells are promising for mass production using cheaper fabrication methods and have high volumetric power densities. Nevertheless, high temperature sealing and thermal expansion mismatch among cell components present the most severe challenges in design of planar SOFC stacks. Decreasing the operating temperature will alleviate the problems adherent to planar designs and thus make them more attractive for commercialization.

### 3.1.1 Principles of Operation

Solid oxide fuel cells consist of an ion conducting, dense solid electrolyte sandwiched between two porous solid electrodes. There are two types of SOFC electrolytes: oxide ion and proton conductors. Although the conducting mechanisms of electrolytes are different, the operating principles are the same for both types of cells, *i.e.*, electrochemical reactions occurring at the anode and cathode and the transport of ions in the electrolyte, giving rise to a direct current spontaneously.

Figure 3-1 illustrates the basic operating principle of an SOFC with oxide ion conducting electrolyte. During operation, oxygen from air transports through the porous cathode to gas-cathode-electrolyte three phase boundary sites, where it catalytically combines with incoming electrons from the external circuit to form oxide ions. Oxide ions at the cathode-electrolyte interface then move through the gas-tight, oxide-ion conducting electrolyte to the anode-electrolyte interface. At the same time, input fuel ( $H_2S$ ) transports through the porous anode to the anode-electrolyte interface, where it is oxidized electrochemically to liberate electrons and produce water vapor. The electrons,

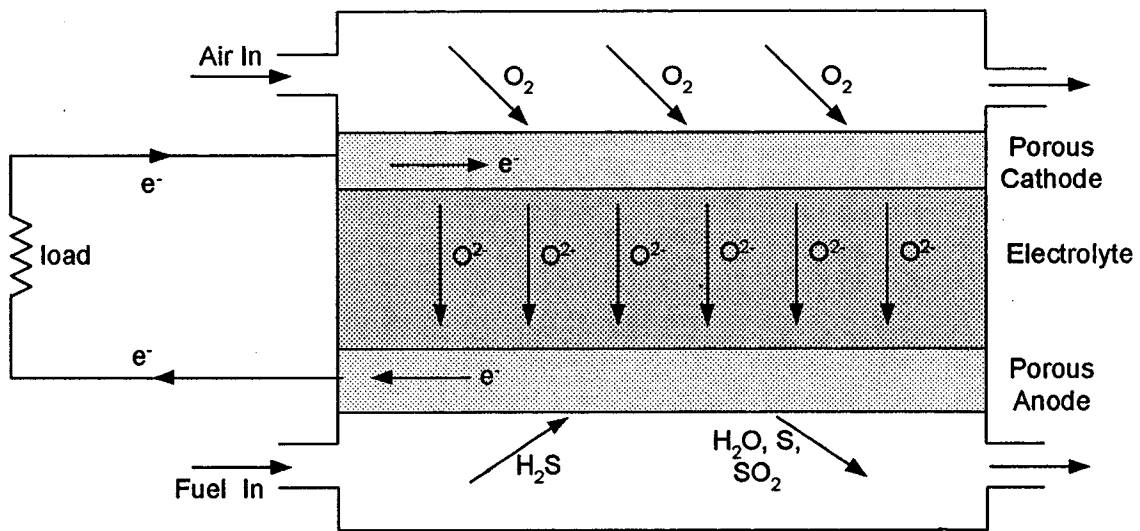


**Figure 3-1** Schematic diagram of a SOFC

which cannot pass through the electrolyte, flow from the anode to the cathode through the external circuit containing a motor or other electric load that consumes the power generated by the cell. Depending on the input fuel and electrolyte, different electrochemical reactions will occur. To achieve the desired power output, individual cells must be bundled into an array of series-parallel electrically connected cells, the fuel cell stack.

### **3.1.2 Materials for Solid Oxide Fuel Cells**

SOFCs are complex, multi-component (electrolyte, cathode, anode, interconnect, seals) devices. Each component performs several functions. The main function of electrodes is to catalyze the electrochemical reactions, *i.e.*, fuel oxidation at anode or oxygen reduction at cathode, as well as chemical reactions if internal steam reforming of hydrocarbons is required. The electrodes also serve as a flow path for gas transport and electron transfer; thus they should possess sufficient porosity and good electronic conductivity. Mixed ionic-electronic conductors are now considered to be preferable electrode materials in that the whole electrode area can be utilized as active reaction sites. The solid electrolyte acts as ion conductor and electron insulator, allowing the flow of ions from one electrode to the other while electrons must travel through the external circuit, thereby continuously producing electricity. High ionic conductivity in the range of 0.01-0.1 S/cm is required to ensure high cell performance [5]. In contrast, electronic conduction of an electrolyte short-circuits the electrolyte internally, resulting in voltage loss and oxygen leakage. The electrolyte must also have a dense structure, so as to serve

as a barrier to prevent the mixing or crossover of reactants, so that high energy-conversion efficiency can be achieved.

The materials selected for cell components have significant effects on fuel cell performance. Each material has to act not only in its own duty but also compatibly with other cell components. Therefore, apart from the special criteria associated with any individual component, the materials of SOFC components have to meet some general requirements [6]:

- (1) Chemical stability and compatibility with adjoining components in their respective atmospheres.
- (2) Low vapor pressure to avoid loss of material.
- (3) Desirable structural (phase) stability and morphological stability (resistance to sintering and minimal grain growth).
- (4) Minimal thermal expansion mismatch among various cell components.
- (5) Sufficient mechanical strength and toughness.
- (6) Economics and ease of cell fabrication.

Despite the fact that various SOFC developers use different cell designs and fabrication techniques, the basic electrode and electrolyte materials used are similar in all cases.

### *3.1.2.1 Electrolyte*

Currently, three groups of electrolyte materials have attracted the most attention for use in solid oxide fuel cells, which are doped zirconia, doped ceria and a new class of perovskites based on  $\text{LaGaO}_3$  ( $\text{ABO}_3$ ) doped at both A- and B-sites. To date, zirconia-based electrolytes are the best choice in terms of conductivity, stability with respect to

other SOFC components and fuel cell operating environments, and mechanical properties. Yttria stabilized zirconia (YSZ) with 8-10 mol%  $Y_2O_3$  is the most commonly used electrolyte in practical SOFCs. In contrast, 3 mol% YSZ is used only in special cases to take advantage of the superior mechanical strength at room temperature, because its ionic conductivity is lower than that of 8 mol% YSZ [5]. Scandia stabilized zirconia (ScSZ) exhibits the highest conductivity in zirconia-based oxides [7] and comparable mechanical properties with YSZ [8]. However, the long-term stability of ScSZ has not been demonstrated and the cost of scandia is relatively high.

Ceria doped with alkaline or rare earth oxides is one of the most promising candidates for low temperature operation of SOFCs. The ceria-based electrolytes have higher ionic conductivities than most zirconia-based electrolytes, with the exception of ScSZ [9]. Their ionic conductivities vary with the kind of dopant, its concentration and the microstructure. A recent study suggested that  $Gd^{3+}$  is the preferred dopant compared to  $Sm^{3+}$  and  $Y^{3+}$  for operation at 500°C [10]. It has also been shown that the highest ionic conductivity is obtained at around 10 mol% for alkaline earth metal oxide or  $Sm_2O_3$  addition and 4 mol% for  $Y_2O_3$  addition [11]. However, the doped ceria electrolytes develop electronic conductivity due to the reduction of  $Ce^{4+}$  to  $Ce^{3+}$  at low oxygen partial pressures prevailing in the anode compartment, resulting in an internal short circuit of the cell. The electronic leakage current by electronic conductivity in the electrolytes increases with increasing temperature or with decreasing electrolyte thickness [12]. Therefore, it is necessary to optimize the operating conditions, the electrolyte thickness and the electrochemical performance of the electrodes in order to attain the maximum efficiency of SOFCs with doped ceria electrolytes. The use of a bi-layer electrolyte with

YSZ is an alternative approach to prevent the reduction of ceria-based electrolytes on the fuel side [13]. However, it is imperative to avoid the direct contact of the two electrolyte materials at temperatures above 1200°C during fabrication because ceria and zirconia react and diffuse into each other at this temperature. The solid solutions so formed have much lower ionic conductivity than either zirconia- or ceria-based electrolytes [14].

More recently, a new family of electrolytes based on LaGaO<sub>3</sub> perovskite has also attracted much attention for reduced temperature operation of SOFCs because of its comparable ionic conductivity and much wider ionic domain than that of doped ceria. Nevertheless, these materials suffer from several defects. They are unstable due to both the reactivity with Ni in the anode and Ga evaporation in reducing atmospheres. However, it has been demonstrated that the reaction of doped LaGaO<sub>3</sub> electrolyte with anodes containing Ni can be suppressed by introducing a CeO<sub>2</sub> interlayer [15]. The high cost of gallium and the low mechanical strength of the perovskite also impede the use of LaGaO<sub>3</sub>-based electrolytes in SOFCs. It has been reported that the addition of aluminum can improve the mechanical stability of this type of electrolyte material [16]. Another issue that has not yet been resolved is that it is difficult to fabricate pure single-phase ceramic electrolytes. Additional non-conductive phases such as SrLaGa<sub>3</sub>O<sub>7</sub> and La<sub>4</sub>Ga<sub>2</sub>O<sub>9</sub> are often detected in the grain boundaries [17].

Other perovskite oxides, such as doped BaCeO<sub>3</sub>, doped SrCeO<sub>3</sub> and doped BaZrO<sub>3</sub>, have high proton conductivity [18,19]. The major disadvantage of BaCeO<sub>3</sub>-based oxides as potential electrolytes for SOFCs is that they are not stable in CO<sub>2</sub>-containing atmospheres. While doped BaZrO<sub>3</sub> offers excellent chemical stability against reaction with CO<sub>2</sub>, this material is exceptionally refractory; consequently processing of

dense electrolyte membranes with low grain boundary resistance remains a significant challenge [20].

Table 3-1 gives ionic conductivities of several electrolytes presently used or showing promise for future SOFC applications, and their known operating temperatures.

### 3.1.2.2 Cathode

Optimization of the composition of cathode, its microstructure and electrical conductivity are of particular importance for a high performance SOFC, especially at low operating temperatures. A variety of noble metals and oxides have been examined as candidates for SOFC electrodes. Platinum is one of the most popular “standard” electrodes for both cathode and anode, but its usage is limited because of the high price. Gold is less active than Pt as a catalyst. The low melting point (961°C) of silver makes it unsatisfactory for high temperature SOFC applications even though Ag shows higher catalytic activity towards oxygen reduction [5].

The state-of-the-art cathode materials in practical solid oxide fuel cells are based on  $\text{LaMnO}_3$  perovskite in which La is partially substituted by Sr (LSM). At this type of electrode, the reduction of oxygen is sufficiently fast at high temperatures. Moreover, reactivity and inter-diffusion studies have shown that any interactions between doped  $\text{LaMnO}_3$  and YSZ electrolyte are minimal at operating temperatures up to 1000°C [23]. However, undesired reactions between these two materials do take place at temperatures above 1200°C leading to the formation of one or both of  $\text{La}_2\text{Zr}_2\text{O}_7$  and  $\text{SrZrO}_3$ , depending on the composition of the cathode materials. These reaction products not only deactivate the cathode catalyst but also increase the interface resistance due to their low

**Table 3-1** Ionic conductivity of some typical or candidate SOFC electrolytes

<i>Electrolyte</i>		$\sigma [S cm^{-1}]$				<i>Ref</i>
		1000°C	800°C	700°C	500°C	
Oxide Ion	$(ZrO_2)_{0.97}(Y_2O_3)_{0.03}$	0.056	0.018	--	--	8
	$(ZrO_2)_{0.92}(Y_2O_3)_{0.08}$	0.16	0.03	--	--	8
	$(ZrO_2)_{0.92}(Sc_2O_3)_{0.08}$	0.38	0.13	--	--	8
	$(ZrO_2)_{0.89}(Sc_2O_3)_{0.11}$	0.32	0.12	--	--	8
	$Ce_{0.9}Gd_{0.1}O_{1.95}$	--	--	0.0544	0.0095	10
	$Ce_{0.8}Gd_{0.2}O_{1.9}$	--	--	0.047	0.0053	10
	$Ce_{0.9}Sm_{0.1}O_{1.95}$	--	--	0.02	0.0033	10
	$Ce_{0.887}Y_{0.113}O_{1.9435}$	--	--	0.1015	0.0087	10
	$La_{0.8}Sr_{0.2}Ga_{0.83}Mg_{0.17}O_{0.2815}$	--	0.17	0.08	--	21
Proton	$BaCe_{0.9}Y_{0.1}O_{2.95}$	--	--	0.02	--	22
	$BaZr_{0.9}Y_{0.1}O_{2.95}$	--	--	0.007	0.0064	19

conductivities, resulting in relatively poor cell performance. The electronic conductivity of LSM increases with increasing Sr concentration up to a maximum around 50 mol%, but the cathode containing more than 30 mol% Sr reacts with YSZ electrolyte to form  $\text{SrZrO}_3$  [24]. It has been reported that incorporation of around 10 mol% excess of Mn can effectively suppress the formation of those resistive layers [25]. Because the ionic conductivity of LSM is quite low, a second ionic conducting phase is often added to LSM to extend the reaction zone into the electrode bulk. LSM-YSZ composite electrodes have been shown to have high electrocatalytic activity to oxygen reduction at lower operating temperatures [26]. Similarly, the addition of a small amount of noble metal catalysts to LSM is known to considerably enhance oxygen reduction rates [27].

Alternative perovskites with Co and/or Fe at the B-site, such as Sr-doped  $\text{LaCoO}_3$  (LSC) and Sr-doped  $\text{LaFeO}_3$  (LSF), have also been investigated with respect to their suitability as cathode materials. LSC exhibits much higher electronic and ionic mixed conductivity as well as superior catalytic activity for oxygen reduction [5]. Unfortunately, however, LSC reacts readily with YSZ forming the insulating inter-phases  $\text{La}_2\text{Zr}_2\text{O}_7$  and  $\text{SrZrO}_3$ . To solve this problem, a thin layer of ceria solid solutions may be used as a diffusion barrier between the YSZ electrolyte and the cobalt mixed-conducting cathode. No reactions occur when coupling doped ceria and LSC. But this approach complicates the fabrication procedure and creates a further increase in resistance by introducing the ceria-zirconia interface [28]. Therefore, LSC is favorable for use with ceria-based electrolytes in SOFCs at low operating temperatures. Unfortunately, use of large amounts of Co in cathode materials leads to an increased thermal expansion coefficient, resulting in delamination at the cathode/electrolyte interface and cracking of the electrolyte [1].

One solution is to reduce the thermal expansion coefficient of LSC by replacing a portion of Co with another element. More recently,  $\text{La}_{1-x}\text{Sr}_x\text{Fe}_{1-y}\text{Co}_y\text{O}_3$  (LSFC) has been examined extensively and this material shows good electrical conductivity, high oxygen surface exchange coefficient and high oxygen self diffusion coefficient [11]. Furthermore, LSFC does not react with ceria-based electrolytes, and low cobalt content LSFC has a thermal expansion coefficient compatible with ceria [8]. Cell consisting of doped ceria electrolyte and an LSFC cathode with new microstructures displayed excellent performance at the low operating temperature of  $500^\circ\text{C}$ , indicating good compatibility between these two materials and the inherent high catalytic activity of LSFC [29].

### *3.1.2.3 Anode*

The Ni-YSZ cermet is now employed as the anode material by a majority of SOFC developers. As anode catalyst, Ni offers good catalytic activity for hydrogen dissociation and oxidation, and high electronic conductivity [11]. Partly coating nickel particles with YSZ improves the thermal expansion match with the electrolyte, controls Ni grain growth, increases the three phase boundary area for fuel oxidation and improves the long term stability of the anode [6]. Composite anodes with Ni content about 40% are good electronic conductors and possess a thermal expansion coefficient close to that of YSZ [30]. The Ni-YSZ cermet electrodes show good electrochemical performance when the cell is operated on hydrogen or pre-reformed natural gas fuels at  $800\text{-}1000^\circ\text{C}$ . However, the cermets are unsatisfactory for use with unreformed natural gas or hydrocarbon fuels because of the high catalytic activity of Ni for hydrocarbon

dissociation accompanied by carbon deposition. The carbon deposits block pores and active reaction sites and consequently deteriorate the anode performance. Another disadvantage of Ni-YSZ cermets is the re-oxidation of Ni, which is accompanied by a deleterious volume expansion, when the environment of Ni in the anode compartment becomes too oxidizing [17]. Furthermore, the sulfur tolerance of Ni is relatively low (< 10 ppm), and higher levels of sulfur quickly degrade the anode performance due to catalyst deactivation.

Some ceria solid solutions have been tested in place of YSZ in cermet anodes [24]. Ceria is advantageous in that it develops electronic conductivity in reducing fuel environments and has higher ionic conductivity than YSZ at lower temperatures. In addition, it has been shown that the presence of ceria in the anode promotes direct hydrocarbon oxidation and reduces the carbon deposition rate [31]. To avoid the detrimental effects of Ni, alternative doped ceria compounds were used to replace Ni-ceria cermets as anode materials in low-temperature SOFCs. These materials show very low or even negligible activity for coking and are redox stable at cell operating conditions [32]. Doped ceria anodes incorporating highly dispersed noble metal catalysts, such as Pt and Ru, on the surface have shown significantly improved catalytic activities, especially at reduced temperatures [11]. Recently, promising ceria-based composite anodes Cu/CeO<sub>2</sub> or Sr-doped CeO<sub>2</sub>/YSZ have been developed for the direct oxidation of various hydrocarbon fuels [33]. No carbon deposition was observed when using a variety of alkanes and alkenes as fuels. It has been shown that the novel SOFC anodes can have reasonably high sulfur tolerance, to at least 100 ppm, a level sufficiently high to allow direct feeding of some present hydrocarbon fuels [34].

Other materials based on the perovskite structure, such as doped CaTiO<sub>3</sub> and doped LaYO<sub>3</sub>, have also been considered as potential anode catalysts. However, the materials developed to date each require incorporation of a second phase of electronic conducting oxide or metal as electronic conductor and current collector [35].

## 3.2 H<sub>2</sub>S-powered Solid Oxide Fuel Cells

### 3.2.1 Electrochemical and Chemical Reactions

When hydrogen sulfide is utilized as the fuel and air is the oxidant in a solid oxide fuel cell with an oxide-ion conducting electrolyte, the half-cell reaction occurring at the cathode is the same as in a fuel cell operating on hydrogen fuel, *i.e.*, the electrochemical reduction of oxygen to oxide ions as follows:



The anode reactions by which hydrogen sulfide is oxidized are much more complicated when compared with that of hydrogen oxidation. Depending on the operating condition, one or both of two possible reactions may take place at the anode, which are accompanied by the migration of oxide ions through the electrolyte:



Combining the two possible anode half-cell reactions with reaction (3-1), the two possible overall fuel cell reactions can be expressed as follows:





Neither of these reactions is thermodynamically strongly favored over the other. Table 3-2 shows the thermodynamic values for reactions (3-4) and (3-5) (HSC Chemistry software, Version 4.0, Outokumpu Research). The similar reversible potentials at fuel cell operating temperatures make it difficult to electrochemically distinguish between the two reaction pathways.

It is well known that hydrogen sulfide will thermally decompose at elevated temperatures into hydrogen and sulfur. Table 3-3 gives the equilibrium compositions of different species at fuel cell operating temperatures of 750-850°C and atmospheric pressure. These values were also calculated using HSC Chemistry software (Version 4.0, Outokumpu Research). The basic decomposition reaction can be represented by the equation:



which is facilitated by a wide variety of metal and metal sulfide catalysts [36]. It should be noted that S<sub>2</sub> is the dominant gaseous sulfur species over the temperature range (750-850°C) of our investigation, as shown in Table 3-3. The hydrogen and sulfur originating from the above equilibrium can be directly electrochemically oxidized at the anode forming H<sub>2</sub>O and SO<sub>2</sub>, respectively:



The sulfur formed by the electrocatalytic oxidation of H<sub>2</sub>S in reaction (3-2) can also be

**Table 3-2** Thermodynamic data for different fuel cell reactions

Temperature (°C)	Overall Reaction					
	$H_2S + \frac{1}{2}O_2 \rightarrow H_2O + \frac{1}{2}S_2$			$H_2S + \frac{3}{2}O_2 \rightarrow H_2O + SO_2$		
	$\Delta H^\circ$	$\Delta G^\circ$	$E^\circ_{rev.}$	$\Delta H^\circ$	$\Delta G^\circ$	$E^\circ_{rev.}$
	(kJ/mol)	(kJ/mol)	(V)	(kJ/mol)	(kJ/mol)	(V)
750	-158.377	-151.327	0.784	-519.955	-438.297	0.757
800	-158.606	-150.977	0.782	-520.070	-434.303	0.750
850	-158.837	-150.616	0.780	-520.182	-430.305	0.743

**Table 3-3** Equilibrium compositions of species from the decomposition reaction of H<sub>2</sub>S

<i>Temperature</i> (°C)	<i>Equilibrium Composition (mol%)</i>									
	H <sub>2</sub> S	H <sub>2</sub>	S <sub>2</sub>	S <sub>3</sub>	S <sub>4</sub>	S <sub>5</sub>	S <sub>6</sub>	S	S <sub>7</sub>	S <sub>8</sub>
750	92.2	5.22	2.57	2.74E-02	1.11E-03	3.07E-05	9.43E-06	1.40E-07	7.14E-07	2.58E-08
800	89.4	7.10	3.50	3.30E-02	1.15E-03	2.18E-05	5.44E-06	5.41E-07	3.69E-07	1.04E-08
850	86.0	9.32	4.60	3.86E-02	1.17E-03	1.58E-05	3.24E-06	1.85E-06	1.99E-07	4.48E-09

consumed in a consecutive step via reaction (3-8).

Another important non-electrochemical reaction that may proceed in the anode compartment is the second step of the Claus process. If sulfur dioxide is present in an excess amount of  $H_2S$  at high temperatures, it will be chemically consumed by the excess hydrogen sulfide to produce sulfur and water, as shown by reaction (1-2). As a result, lack of sulfur dioxide in the anode effluent is not itself sufficient evidence for a mechanism including reaction (3-2) over the combination of reactions (3-3) and (1-2).

As described above, several competing electrochemical and chemical reactions can take place at anodes of  $H_2S$ -powered solid oxide fuel cells. These are associated with each other, which may lead to various possible reaction mechanisms. Establishing the actual reaction pathway under different fuel utilization and operating conditions is essential for understanding and, ultimately, optimizing the process.

### 3.2.2 Results from Earlier Studies

Electrochemically oxidizing  $H_2S$  in a solid oxide fuel cell was unexploited until the late 1980s when Pujare *et al* showed that a SOFC based on yttria-stabilized zirconia (YSZ) electrolyte could operate on high concentrations of  $H_2S$  (99.5%) fuel at  $900^\circ C$  [37]. In addition, this pioneering study found that the thiospinel ( $CuFe_2S_4$ ) anode appeared to possess good electronic conductivity and stability. Subsequent studies by the same group investigated electrode kinetics for the fuel cells with either yttria (8 wt%) or calcia (5 wt%) stabilized zirconia as the electrolyte [38]. Sr-doped  $LaMnO_3$  (LSM) was used as the cathode material and various thiospinels and  $WS_2$  were evaluated as potential anodes. All the thiospinels demonstrated high intrinsic electronic conductivity. The

relative activities of the anode electrocatalysts, based on empirical kinetics, were found to be in the order:  $\text{NiFe}_2\text{S}_4 > \text{WS}_2 > \text{CuCo}_2\text{S}_4 > \text{CuFe}_2\text{S}_4 \approx \text{NiCo}_2\text{S}_4 > \text{CuNi}_2\text{S}_4$ . The dependency of electrode kinetic data on the anode fuel compositions and the close to 1 V open circuit potentials at 900°C suggested that the predominant electroactive species present in the anode compartment was hydrogen arising from the initial thermal dissociation of  $\text{H}_2\text{S}$  at fuel cell operating temperatures [38], as indicated in reaction (3-6) and Table (3-3).

Studies on metal anode catalysts were performed by Ong *et al* in low levels of  $\text{H}_2\text{S}$  streams [39]. The current-overpotential curves indicated that no sulfur poisoning occurred at Pt, Au or Ni anodes in the subject fuel cells. These authors believed that the electrocatalytic sites for gaseous anode reactions were the oxygen vacancies with trapped electrons present in the YSZ electrolyte, and that the electrodes only served as paths for electron transfer. It was proposed that the oxygen vacancies could be formed by electrolytically removing oxide ions from the electrolyte.

Yentekakis and Vayenas examined the nature of the electrochemical oxidation of  $\text{H}_2\text{S}$  and the product distribution in a solid electrolyte fuel cell with YSZ electrolyte and porous Pt as both anode and cathode [40]. Both thermal catalytic and electrocatalytic reactions were believed to occur at the Pt anode. However, the authors accepted the possibility that some electrocatalytic reactions could take place at the oxygen vacancies on the electrolyte surface. They determined that product selectivity and power output performance of the cell strongly depended on the ratio of the fluxes of oxide ions pumped through the electrolyte and hydrogen sulfide reaching the anode [40]. Operating the cell at low ratios favored the formation of sulfur, which could block the transfer of  $\text{H}_2\text{S}$  to the

three phase boundary sites and hence led to degradation of cell power output. It was shown that excessive sulfur deposition caused irreversible losses in electrocatalytic activity of the anode, extensive sintering or even detachment of the Pt electrode from the solid electrolyte. This study indicated that it was advantageous to operate the fuel cell under high ratio conditions, which may eliminate sulfur formation and lead to the majority of H<sub>2</sub>S conversion to SO<sub>2</sub>. It was shown that when the ratio exceeded 0.33, the product selectivity to SO<sub>2</sub> was greater than 90% and the cell performance was stable.

The stabilized zirconia electrolytes employed in the earlier studies were very thick, typically 1.5-2 mm, which contributed strongly to high cell resistance and thus resulted in low current densities. Efforts then were directed to the development of alternative highly conductive, H<sub>2</sub>S-tolerant electrolyte materials. Several ceria-based electrolytes were first studied by Kirk and Winnick because doped ceria has superior ionic conductivity at lower temperatures [41]. Although x-ray diffraction analysis confirmed no conversion of the oxide-ion conductors, yttria- or samaria-doped ceria, by H<sub>2</sub>S, the proton-conducting ytterbia-doped strontium cerate electrolyte was found to react with H<sub>2</sub>S causing a decay of the cell performance.

Studies on selecting suitable electrolyte materials other than zirconia were then pursued by the same group [42,43]. Pt was used as electrodes in all the experiments. It was observed that the mixed-ion conducting electrolyte composed of samaria-doped barium cerate also suffered from gradual degradation caused by the formation of a layer of nonconductive sulfate, BaSO<sub>4</sub>, upon exposure to H<sub>2</sub>S fuel [42]. Preliminary tests using pure Li<sub>2</sub>SO<sub>4</sub> as a proton conductor showed no conversion of the electrolyte by hydrogen sulfide at an intermediate temperature around 700°C [42]. The composite electrolyte

$\text{Li}_2\text{SO}_4\text{-Al}_2\text{O}_3$  exhibited much better performance than  $\text{Li}_2\text{SO}_4$  alone [44]. Fuel cell performance was sensitive to the impurity contents in  $\text{Li}_2\text{SO}_4$  samples. Ceria doped with 20 mol% samaria provided the best performance among the doped ceria electrolyte materials tested under operation with  $\text{H}_2\text{S}$  fuel [43]. Power density of  $10.2 \text{ mW/cm}^2$  was obtained for this cell at about  $700^\circ\text{C}$ . However, this material developed electronic conductivity in the anode environment, which resulted in reduced cell performance. Analysis of the product distribution for the ceria-based solid oxide fuel cell indicated that two electrochemical processes for  $\text{H}_2\text{S}$  oxidation occurred simultaneously at the anode. This analysis also confirmed Yentekakis and Vayenas' findings that, at high utilization of hydrogen sulfide, sulfur dioxide was the favored product, as opposed to sulfur. Nevertheless, because of the complexity of the system, the exact nature and sequence of the anode reactions could not be determined unambiguously [43].

The most recent study on utilizing  $\text{H}_2\text{S}$  as fuel in SOFCs was carried out by Yates and Winnick [45]. YSZ was used as electrolyte, and Pt or LSM as the cathode. Several metal sulfides were investigated as anode materials. Cobalt sulfide rapidly degraded over time and had poor adherence to the YSZ electrolyte. Tungsten sulfide and lithium cobalt sulfide were stable in the presence of  $\text{H}_2\text{S}$  for an extended period of time. The best power outputs were obtained using lithium cobalt sulfide as the anode material, nearly  $90 \text{ mW/cm}^2$  at  $830^\circ\text{C}$  for thick (0.4-0.5 mm) YSZ disks and  $400 \text{ mW/cm}^2$  at  $770^\circ\text{C}$  for thin (0.04 mm) tubular YSZ films, respectively. However, cell performance decreased slowly over time. In this study, gas analysis results showed that both sulfur and sulfur dioxide were formed in the fuel cell, which was consistent with Peterson and Winnick's analysis [43].

Though some progress has been made through these previous studies, development of practical solid electrolyte fuel cells utilizing hydrogen sulfide as fuel still needs substantial further research before their maturity can be compared with the most extensively developed hydrogen-powered SOFCs.

The research presented in this thesis is intended to further investigate the effectiveness of using pure H<sub>2</sub>S as fuel in SOFCs, as opposed to diluted H<sub>2</sub>S as employed in almost all the previous studies except the initial works done by Pujare *et al.* Thin 8 mol% YSZ disks were used as the electrolytes and platinum as the model cathode material. Special attention was paid to the development of anode materials and the improvement of fuel cell stability. Both metal and metal sulfide catalysts were examined as potential anodes. Gas analysis of the anode effluent streams was also conducted in trying to better understand the nature of the electrochemical oxidation of hydrogen sulfide.

## References

- [1] E. Ivers-Tiffée, A. Weber and D. Herbristrit, *Journal of the European Ceramic Society*, **21**, 1805 (2001).
- [2] A. B. Stambouli and E. Traversa, *Renewable and Sustainable Energy Reviews*, **6**, 433 (2002).
- [3] M. Cassir and E. Gourba, *Annales de Chimie des Matériaux*, **26** (4), 49 (2001).
- [4] N. Q. Minh, *Journal of the American Ceramic Society*, **76**, 563 (1993).
- [5] T. Kawada and J. Mizusaki, '*Handbook of Fuel Cells*', Vol. 4, Chapter 70, John Wiley & Sons Ltd., West Sussex, England (2003).

- [6] S. P. S. Badwal and K. Foger, *Materials Forum*, **21**, 187 (1997).
- [7] Y. Arachi, H. Sakai, O. Yamamoto, Y. Takeda and N. Imanishi, *Solid State Ionics*, **121**, 133 (1999).
- [8] O. Yamamoto, *Electrochimica Acta*, **45**, 2423 (2000).
- [9] S. P. S. Badwal, *Solid State Ionics*, **143**, 39 (2001).
- [10] B. C. H. Steele, *Solid State Ionics*, **129**, 95 (2000).
- [11] O. Yamamoto, '*Handbook of Fuel Cells*', Vol. 4, Chapter 71, John Wiley & Sons Ltd., West Sussex, England (2003).
- [12] M. Godickemeier and L. J. Gauckler, *Journal of the Electrochemical Society*, **145**, 414 (1998).
- [13] T. Tsai, E. Perry and S. Barnett, *Journal of the Electrochemical Society*, **144**, L130 (1997).
- [14] A. Tsoga, A. Gupta, A. Naoumidis, D. Skarmoutsos and P. Nikolopoulos, *Ionics*, **4**, 234 (1999).
- [15] K. Huang, J. Wan and J. B. Goodenough, *Journal of the Electrochemical Society*, **148**, A788 (2001).
- [16] I. Yasuda, Y. Matsuzaki, T. Yamakawa and T. Koyama, *Solid State Ionics*, **135**, 381 (2000).
- [17] B. C. H. Steele and A. Heinzl, *Nature*, **414**, 345 (2001).
- [18] H. Uchida, N. Maeda and H. Iwahara, *Solid State Ionics*, **11**, 117 (1983).
- [19] H. G. Bohn and T. Schober, *Journal of the American Ceramic Society*, **83**, 768 (2000).
- [20] S. M. Haile, *Materials Today*, **6**(3), 24 (2003).

- [21] K. Huang, R. S. Tichy and J. B. Goodenough, *Journal of the American Ceramic Society*, **81**, 2565 (1998)
- [22] T. Schober, *Solid State Ionics*, **162-163**, 277 (2003).
- [23] S. C. Singhal, *Solid State Ionics*, **135**, 305 (2000).
- [24] J. M. Ralph, A. C. Schoeler and M. Krumpelt, *Journal of Materials Science*, **36**, 1161 (2001).
- [25] H. Yokokawa, T. Horita, N. Sakai, M. Dokiya and T. Kawada, *Solid State Ionics*, **86-88**, 1161 (1996).
- [26] J. Kim, A. V. Virkar, K. Fung, K. Mehta and S. C. Singhal, *Journal of the Electrochemical Society*, **146**, 69 (1999).
- [27] J. W. Erning, T. Hauber, U. Stimming and K. Wippermann, *Journal of Power Sources*, **61**, 205 (1996).
- [28] A. J. McEvoy, *Journal of Materials Science*, **36**, 1087 (2001).
- [29] R. Doshi, V. L. Richards, J. D. Carter, X. Wang and M. Krumpelt, *Journal of the Electrochemical Society*, **146**, 1273 (1999).
- [30] P. Holtappels and U. Stimming, '*Handbook of Fuel Cells*', Vol. 1, Chapter 20, John Wiley & Sons Ltd., West Sussex, England (2003).
- [31] E. P. Murray, T. Tsai and S. A. Barnett, *Nature*, **400**, 649 (1999).
- [32] O. A. Marina, C. Bagger, S. Primdahl and M. Mogensen, *Solid State Ionics*, **123**, 199 (1999).
- [33] S. Park, R. J. Gorte and J. M. Vohs, *Applied Catalysis A: General*, **200**, 55 (2000).
- [34] R. J. Gorte, H. Kim and J. M. Vohs, *Journal of Power Sources*, **106**, 10 (2002).

- [35] B. C. H. Steele, 'Oxygen Ion and Mixed Conductors and Their Technological Applications', H. L. Tuller *et al.* (eds.), Kluwer Academic Publishers, Dordrecht, pp. 423-447.
- [36] E. D. Weil and S. R. Sandler, Chapter 4, "Sulfur Compounds", *Kirk-Othmer Encyclopedia of Chemical Technology* (Online), 4<sup>th</sup> Ed, John Wiley & Sons, Inc. (1997).
- [37] N. U. Pujare, K. W. Semkow and A. F. Sammells, *Journal of the Electrochemical Society*, **134**, 2639 (1987).
- [38] N. U. Pujare, K. J. Tsai and A. F. Sammells, *Journal of the Electrochemical Society*, **136**, 3662 (1989).
- [39] B. G. Ong, T. A. Lin, and D. M. Mason, 'Electrode Materials and Processes for Energy Conversion and Storage', S. Srinivasan *et al.* (eds.), PV 87-12, p. 295, The Electrochemical Society Proceedings Series, Pennington, NJ (1987).
- [40] I. V. Yentekakis and C. G. Vayenas, *Journal of the Electrochemical Society*, **136**, 996 (1989).
- [41] T. J. Kirk and J. Winnick, *Journal of the Electrochemical Society*, **140**, 3494 (1993).
- [42] D. Peterson and J. Winnick, *Journal of the Electrochemical Society*, **143**, L55 (1996).
- [43] D. R. Peterson and J. Winnick, *Journal of the Electrochemical Society*, **145**, 1449 (1998).
- [44] B. Zhu and S. Tao, *Solid State Ionics*, **127**, 83 (2000).

- [45] C. Yates and J. Winnick, *Journal of the Electrochemical Society*, **146**, 2841 (1999).

## CHAPTER 4

# H<sub>2</sub>S-POWERED SOLID OXIDE FUEL CELL USING PLATINUM ELECTRODES

### 4.1 Introduction

Solid oxide fuel cells using hydrogen as fuel have been investigated extensively in recent years, and may soon provide a viable commercial option for power generation. However, much less effort has been made in the development of H<sub>2</sub>S-powered SOFCs. A major factor is that hydrogen sulfide is an extremely corrosive and noxious gas, which puts stringent requirements on cell materials, especially at high temperatures.

State of the art yttria-stabilized zirconia (YSZ) is the favored electrolyte material in practical SOFCs, due to its relatively high ionic conductivity and superior chemical stability in numerous gas streams [1]. Alternative oxide ion or proton conductive electrolytes have been shown to either deteriorate over time in the presence of H<sub>2</sub>S gas or have other undesirable performance characteristics [2,3]. Platinum is one of the most popular SOFC electrodes for oxygen reduction. Moreover, the ability of Pt to electrochemically catalyze the oxidation of H<sub>2</sub>S at temperatures above 650°C has been demonstrated [3,4]. It was also observed that platinum exhibits greater resistance to sulfur poisoning in comparison with other metals such as Ni, Fe, Co and Ru [5]. The aim of this phase of study is to investigate the feasibility of utilizing both diluted and pure H<sub>2</sub>S as fuel in SOFCs composed of YSZ electrolytes and Pt electrodes, at 1 atm and 750–850°C.

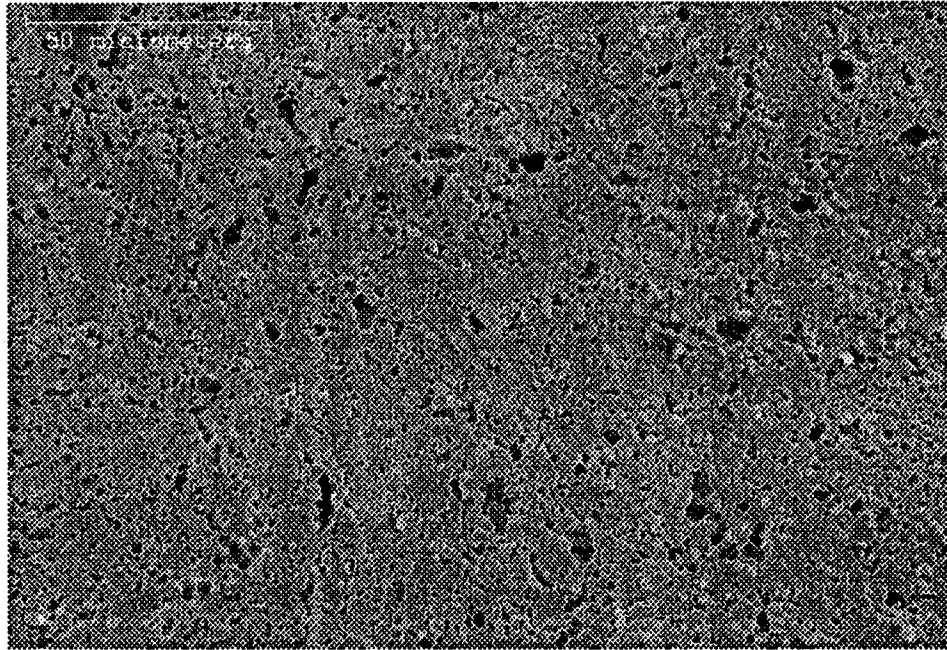
Meanwhile, the contributing factors to overall cell voltage loss will be identified with the help of reference electrode and impedance analysis. The compositions of the anode feed and effluent gases will also be examined in trying to explore the possible reactions taking place in the anode chamber.

## **4.2 Experimental**

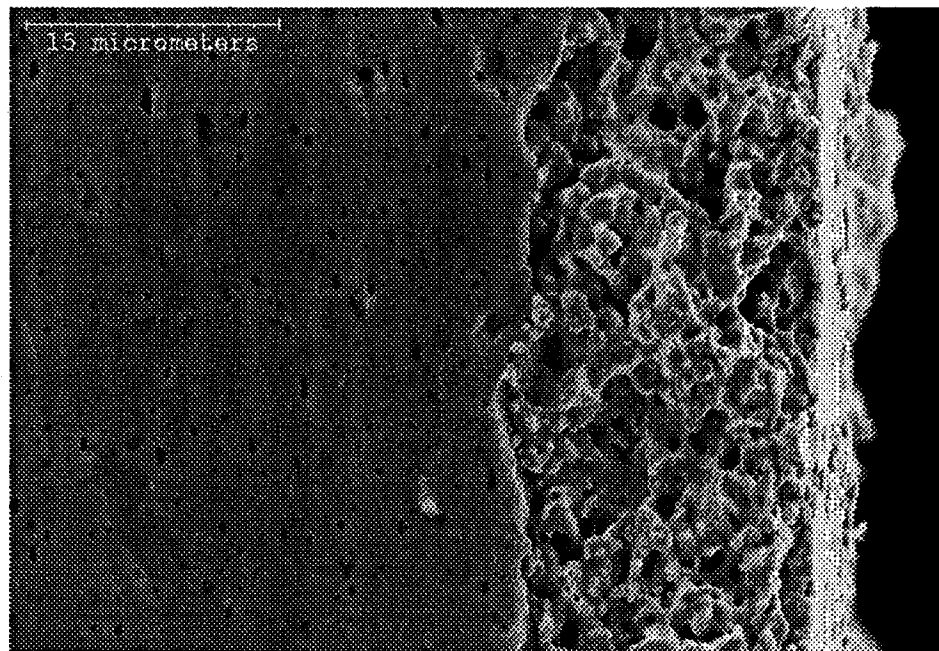
### **4.2.1 Cell Preparation**

Tape-casted 8 mol% YSZ disks with a thickness of 0.2 mm and a diameter of 2.54 cm, supplied by MarkeTech International Inc., were used as electrolytes. Both cathode and anode catalysts were platinum, prepared by screen-printing platinum paste (Heraeus CL11-5100) onto the corresponding surfaces of the YSZ electrolyte. In the case where the anode and cathode overpotentials were to be determined, a reference electrode was painted as a ring surrounding the cathode using the same platinum paste. After drying in the atmosphere for 3 h, the platinum paste was further dried at 130°C for 10 min and then fired at 1050°C for 30 min to remove the organic binder and to increase adhesion to the electrolyte. The superficial surface area of anode or cathode was approximately 1 cm<sup>2</sup>.

The microstructures of the resulting electrode and the electrode/electrolyte interface were inspected using a Hitachi S-2700 scanning electron microscope. Figure 4-1a shows that the fired platinum electrode was uniform and sufficiently porous. The SEM micrograph of the cross section of a typical Pt/YSZ interface (Figure 4-1b) shows that the electrode was in good intimate contact with the dense YSZ electrolyte, and that the thickness of each electrode layer was about 17 μm.



(a)



(b)

**Figure 4-1** (a) Microstructure of a Pt electrode. (b) SEM micrograph of cross section of a Pt/YSZ interface

#### 4.2.2 Fuel Cell System Design

A schematic diagram of the experimental H<sub>2</sub>S-air fuel cell system with planar cell geometry is shown in Figure 4-2. This system comprises anode and cathode compartments, each consisting of two co-axial alumina or mullite tubes. The inner tube extended from outside the heated reaction zone to a position close to the respective electrode of the cell. The two tubes were fastened together at the remote end with a tailing gas outlet. The cell was sandwiched between the outer tubes of the anode and cathode compartment. The outer perimeter of each outer tube was sealed to the cell by applying a thin layer of ceramic adhesive (Aremco 503). Platinum gauze (52 mesh) was applied as the current collector for both anode and cathode. One end of a platinum lead wire was spot-welded to each current collector and the other end was connected to an external circuit. In the case that a reference electrode was used at the cathode side, a third platinum wire was attached to the reference electrode with platinum paste to ensure good contact. Each platinum wire was *ca.* 50 cm long.

The assembled cell was placed in a tubular furnace (Thermolyne F79300) having a uniform temperature zone:  $\pm 0.6^{\circ}\text{C}$  over the central 7.62 cm length of the cell and  $\pm 3.0^{\circ}\text{C}$  to distances up to 7.62 cm each side of the cell. The seals were cured gradually as the cell was heated to the prescribed temperature for testing, prior to operation of the cell under reaction conditions. During the heating procedure, nitrogen was passing through the anode chamber and air through the cathode chamber.

All the fuel cell experiments were carried out in the temperature range of  $750^{\circ}\text{C}$ - $850^{\circ}\text{C}$ . After the cell had stabilized at the operating temperature, the anode feed was switched to fuel gas containing either 5% H<sub>2</sub>S balanced with nitrogen or pure H<sub>2</sub>S. Air or

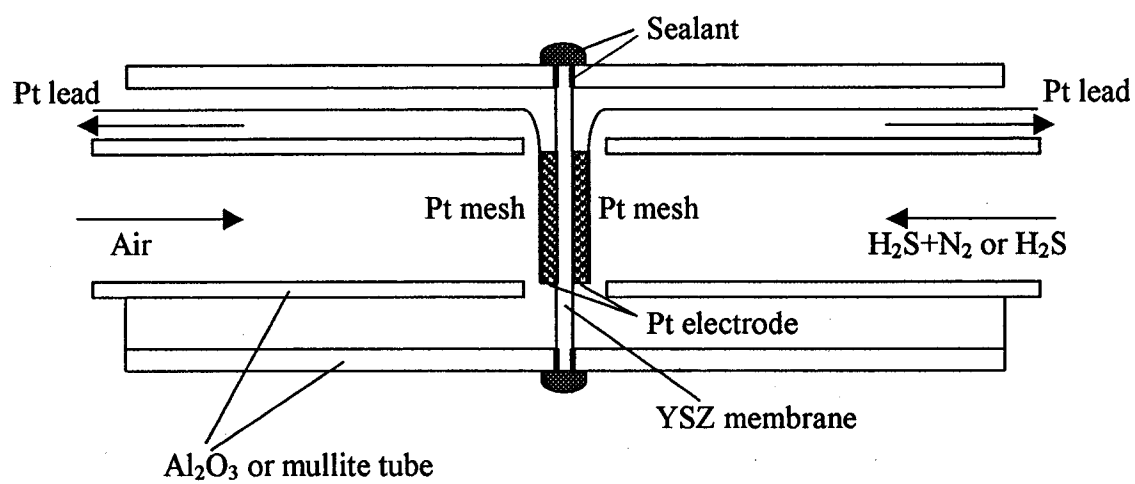


**Figure 4-2** Configuration of first experimental  $H_2S$ -air fuel cell assembly

pure oxygen was supplied to the cathode side as oxidant via the inner tube. The gas flow rates were carefully controlled with mass flow controllers. The effluent gases of the fuel cell exited through the outlet in the annular space of each compartment. Each outlet gas then flowed out via tubing, of which the end was submerged in water. The formation of gas bubbles was monitored to ensure that there was no leakage of gases.

#### **4.2.3 Electrochemical Apparatus**

The open circuit voltage (OCV) between anode and cathode was monitored using a Keithley 199 digital multimeter. When the cell had no leaks, a steady OCV value typically was attained after providing fuel gas for about 60 min. An OCV that fluctuated or had a lower value than 0.7V indicated possible leaks in the cell and therefore no further experiments would be conducted using that system. Potentiodynamic current-potential measurements were performed by operating a Pine AFRED5 potentiostat/galvanostat in potentiostat mode. The scanning rate was kept at 1 mV/s. The potentiostat was used in conjunction with a Virtual-Bench data acquisition system to acquire data automatically. Cell electrochemical impedance analysis was carried out using a Gamry CMS 100/300 impedance measurement system combined with a Stanford SR810 DSP Lock-in amplifier under open-circuit voltage and polarization conditions. Impedance data typically were obtained over the frequency range 50 kHz to 1 Hz. The cell was allowed to equilibrate for at least one hour after each change in operating conditions before conducting further measurements.

#### 4.2.4 Gas Analysis

Gas analysis of the anode effluent streams performed during fuel cell experiments was intended to identify the extent of electrochemical and chemical reactions taking place at the anode. Two gas chromatographs (GC) were included in the gas analysis system, as shown in Figure 4-3. A 3-way valve was used to connect the sample gas inlet of the two GCs with the outlet gas from the anode compartment.

A gas chromatograph (Hewlett-Packard Model 5890 II) coupled with both thermal conductivity detector (TCD) and a Sievers Model 350B sulfur chemiluminescence detector (SCD) was employed to determine the concentrations of hydrogen sulfide and sulfur dioxide in the streams under different operating conditions. Helium was supplied as the carrier gas. The original carrier gas was split into two streams: one for SCD and another for TCD, and its flow rate was controlled by a separate mass flow controller. SCD and TCD were arranged in parallel so that each of the detectors analyzed an effluent from separate GC columns [6]. A CP-Sil 5CB capillary column (50 m x 0.32 mm x 5  $\mu$ m, fused-silica WCOT supplied by Chrompack) with high intrinsic sensitivity was connected to SCD, and a Porapak Q packed column made from stainless steel tube (3 m x 3.2 mm O.D.) was connected to the TCD. Each detector had its own sampling loop connected by a 10-way valve. This combination of equipment enabled precise analysis of the sulfur-containing gases with either high or low concentrations of sulfur species. The temperature program, the flow rates of the carrier gas and the length of the columns were all selected, after empirical evaluation, to obtain the best separation. The parameters under which this GC and the two detectors worked are given in Appendix A, Table A-1. Hewlett-Packard ChemStation software was

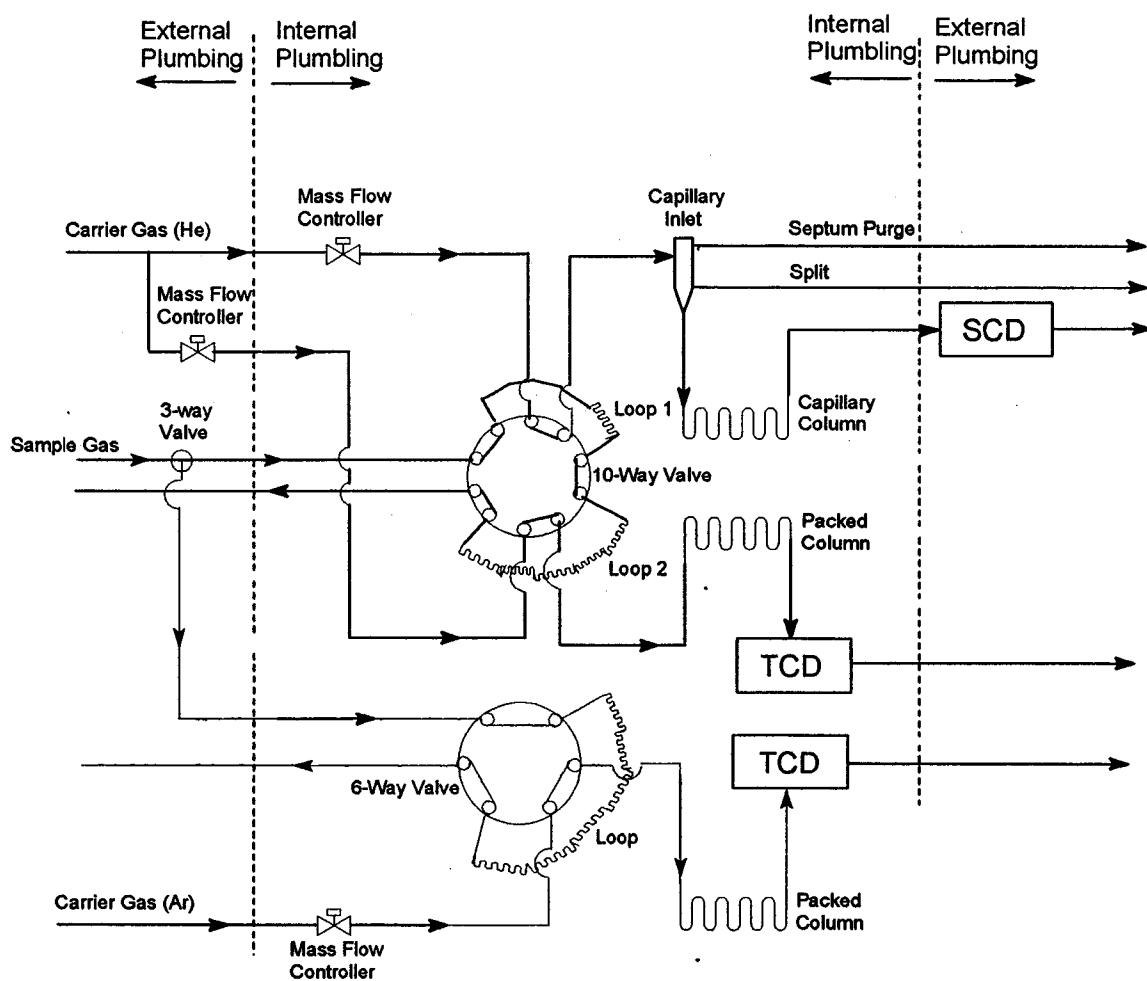


**Figure 4-3** Schematic drawing of the gas analysis system for anode effluent streams

utilized for data acquisition and chromatogram analysis. This software enabled simultaneous data processing of two sets of detector signals.

Another Hewlett-Packard Model 5890 II GC with a TCD detector and an integrator (Hewlett-Packard 3396A) was used to analyze the concentrations of hydrogen in the anode effluents. The packed column also was made from stainless steel tubing (3 m × 3.2 mm O.D.) with Porapak R packing. Argon was used as the carrier gas because of the large thermal conductivity difference between hydrogen and argon. The parameters under which this GC and TCD worked are given in Appendix A, Table A-2.

### 4.3 Results and Discussion

#### 4.3.1 Use of 5% Hydrogen Sulfide as Fuel

##### 4.3.1.1 Open Circuit Voltage

The open circuit voltages of the solid oxide fuel cell using 5% H<sub>2</sub>S as anode feed and air as cathode feed at 750-850°C were all above 1 V. The calculated standard potential values  $E^\circ(T)$  are well below the measured OCVs, which are 0.782 V and 0.750 V at 800°C for reaction (3-4) and reaction (3-5), respectively (Table 3-2).

There are two reasons for the apparent discrepancy between the measured OCV values and the calculated  $E^\circ$  values. The calculated  $E^\circ$  values are based on standard conditions. The equilibrium potentials for reaction (3-4) and reaction (3-5) can be expressed by the following Nernst equations (4-1) and (4-2):

$$E_N = E^\circ(T) - \frac{RT}{2F} \ln\left(\frac{P_{H_2O} P_{S_2}^{1/2}}{P_{H_2S} P_{O_2}^{1/2}}\right) \quad (4-1)$$

$$E_N = E^\circ(T) - \frac{RT}{6F} \ln\left(\frac{P_{H_2O} P_{SO_2}}{P_{H_2S} P_{O_2}^{3/2}}\right) \quad (4-2)$$

where  $E^\circ(T)$  is the cell potential calculated from thermodynamic data  $\Delta G^\circ$  at standard conditions, *i.e.* the potential when the partial pressures of all reactants and products are 1 atm. However, in the experiments under open circuit conditions,  $P_{H_2S}$  was 0.05 atm and  $P_{O_2}$  was 0.21 atm. The equilibrium partial pressures of SO<sub>2</sub> or sulfur vapor and water vapor in the anode compartment were very low at open circuit condition, because of the good sealing, the dense electrolyte film and the "extra dry" grade of feed gases. If it is assumed that the concentrations of water vapor and SO<sub>2</sub> or sulfur vapor are each less than 10 ppm in the anode chamber, the calculated equilibrium potential  $E_N$  is higher than 1.406 V for reaction (3-4) and 1.023 V for reaction (3-5) at 800°C. These values suggested that low partial pressures of products at open circuit conditions could contribute to the high measured OCVs.

A second effect that may contribute to the apparently high OCVs is the presence of hydrogen. The equilibrium concentration of hydrogen produced from the thermal decomposition of H<sub>2</sub>S (Eq. 3-6) is 7.1% at 800°C, as shown in Table 3-3. As a result, competitive electrochemical oxidation of hydrogen will also occur at the Pt anode (reaction 3-7). The Nernst equation for oxidation of H<sub>2</sub> is expressed as follows:

$$E_N = E^\circ(T) - \frac{RT}{2F} \ln\left(\frac{P_{H_2O}}{P_{H_2} P_{O_2}^{1/2}}\right) \quad (E^\circ = 0.98 \text{ V at } 800^\circ\text{C}) \quad (4-3)$$

Assuming the equilibrium concentration for hydrogen and 10 ppm for the concentration of water vapor, the equilibrium potential  $E_N$  in Equation (4-3) is 1.215 V. This value is close to the  $E_N$  values calculated for H<sub>2</sub>S oxidation and could enhance the open cell

voltages. Thus, the measured OCVs may be mixed reaction voltages, the value of which depends on the proportions of each electroactive species present at the anode and their reaction potentials.

#### *4.3.1.2. Current-voltage and Power Density Performance*

Figure 4-4 displays the cell potential vs. current density relationships as well as the generated power curves, obtained using 5% H<sub>2</sub>S as the fuel at 750-850°C. Initially, the current density increases very slowly with reduction in cell voltage above 0.8 V. The current density then quasi-linearly increases with decrease in potential generated. There is no slope deviation in the high current density region, showing that mass transfer is not a limitation for the system [7]. The maximum current density at 850°C is the same as at 800°C. This behavior is abnormal; for most SOFCs the current increases with temperature due to an increase in the electrochemical reaction rate and ionic conductivity of the electrolyte. The cause of these unusual behaviors is the deterioration of the anode, as will be discussed below (Section 4.3.1.3). The maximum current densities achieved were 87 mA/cm<sup>2</sup> at 750°C and 100 mA/cm<sup>2</sup> at 800°C and 850°C. These improved values obtained using our system when compared with the published data for comparable systems [3,4,8] are attributed in part to our use of much thinner self-supporting electrolyte membranes and good sealing to prevent gas mixing due to crossover or leakage. The cells with YSZ or ceria-based electrolytes and Pt electrodes described in the literature are typically 0.6 mm - 1.5 mm thick, and the low values reported for the open circuit potential indicate that related systems may not have had completely gas-tight seals [3, 8].

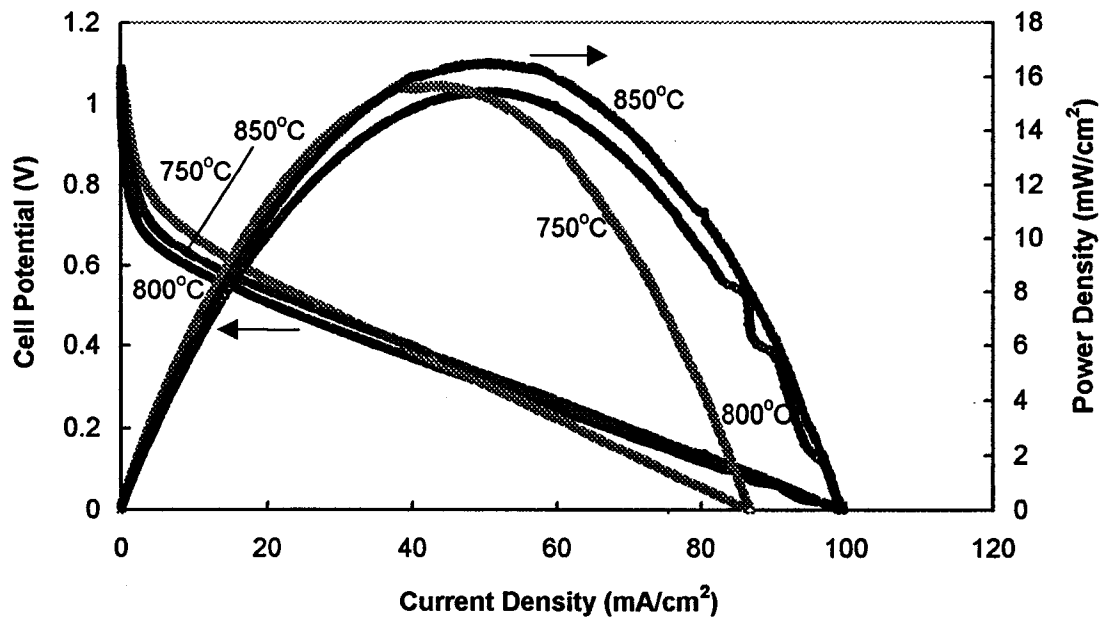


**Figure 4-4** Current-voltage measurements and power curves of a cell tested using 5% H<sub>2</sub>S at 750°C, 800°C and 850°C

The maximum power densities attained at the three different temperatures are similar: 15.6 mW/cm<sup>2</sup> at 750°C, 15.4 mW/cm<sup>2</sup> at 800°C and 16.5 mW/cm<sup>2</sup> at 850°C. The optimum operating values are slightly different. Maximum power density is produced at a current density of 44 mA/cm<sup>2</sup> at 750°C, 49 mA/cm<sup>2</sup> at 800°C and 52 mA/cm<sup>2</sup> at 850°C. Generally, power output is expected to increase with increasing temperature for the same cell configuration [8,9]. The similarity between the three maxima is attributed to similar impedance performance at each temperature, as will now be discussed.

#### *4.3.1.3. Impedance Characteristics*

As described earlier, the impedance spectroscopy (IS) of a solid oxide fuel cell usually comprises several overlapping semicircles. The intercept of the first high frequency semicircle with the real-axis is related to the ionic conductivity of electrolyte as well as additional ohmic losses in electrical connection wire and contact resistance. The distance between the intercepts at the lowest frequency and at the highest frequency represents the effective polarization resistance for electrode reactions.

Impedance spectra for the Pt/YSZ/Pt cell operating with 5% H<sub>2</sub>S at 750°C and 800°C are shown in Figures 4-5 and 4-6a. Measurements were made under open circuit conditions (Figure 4-5) and polarization conditions (at 0 V) (Figure 4-6a). At OCVs, the semicircles for polarization processes evidently are not well developed due to the very high electrode reaction impedance and the insufficient low limit of the frequencies used in the IS tests. However, at 0 V, two overlapping semicircles can be seen for both temperatures. The centers of the semicircles are slightly below the real axis, as a result of

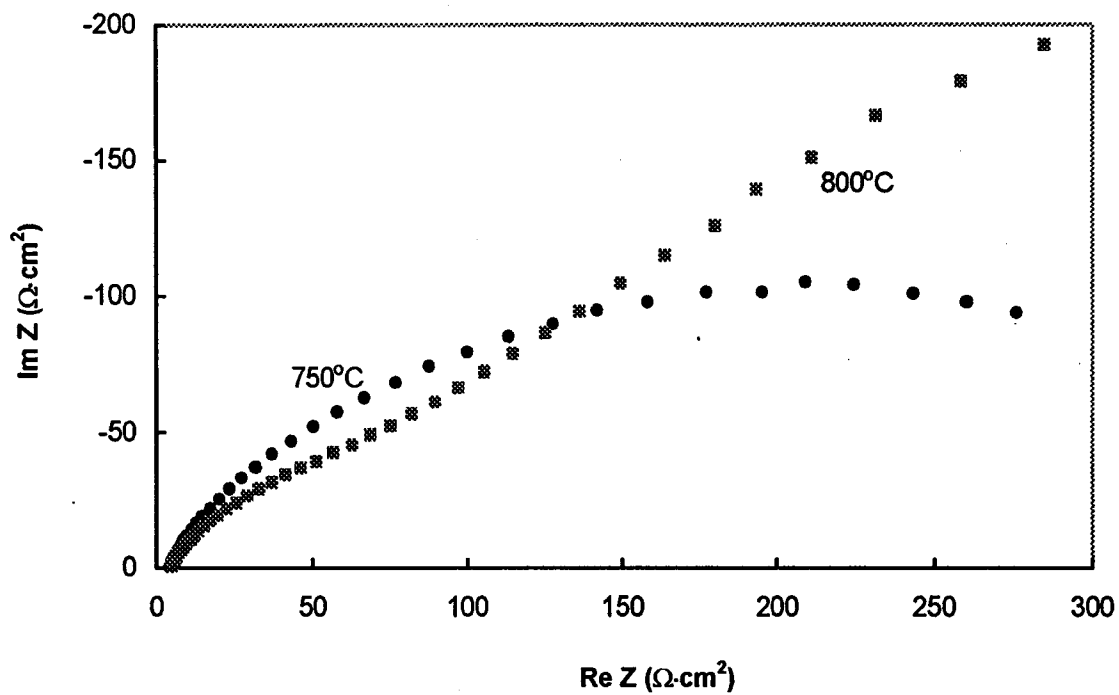
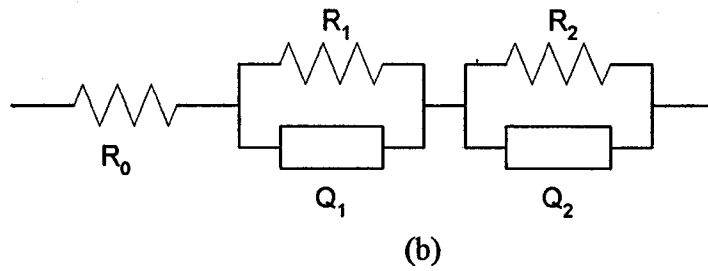
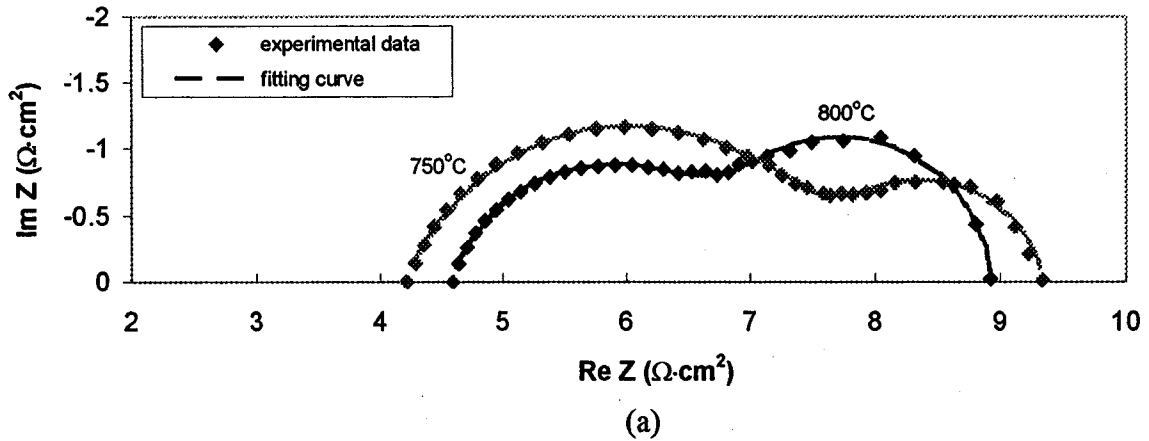


Figure 4-5 Impedance spectra for 5% H<sub>2</sub>S, Pt/8% YSZ/Pt, air fuel cell at 750°C and 800°C under open circuit conditions



**Figure 4-6** (a) Cell impedance spectra using 5% H<sub>2</sub>S as fuel at 750°C and 800°C under polarization condition; (b) simulated equivalent circuit. The fitting parameter values are  $R_0=4.19$ ,  $R_1=3.58$ ,  $R_2=1.58$ ,  $A_1=2150$ ,  $\alpha_1=0.723$ ,  $A_2=60.4$ ,  $\alpha_2=0.877$  at 750°C and  $R_0=4.57$ ,  $R_1=2.36$ ,  $R_2=2$ ,  $A_1=1880$ ,  $\alpha_1=0.765$ ,  $A_2=288$ ,  $\alpha_2=0.96$  at 800°C, where  $A$  and  $\alpha$  are parameters for constant-phase element  $Q$  and the impedance of  $Q$  has the form of  $A(j\omega)^{-\alpha}$ .

either diffusion effects (Warburg impedance) related to different concentrations of electro-active species in the system or a distribution of time constants around an ideal value due to the inhomogeneous cell parameters at the electrode/electrolyte interface or within the materials [10]. Figure 4-6b shows the simulated equivalent circuit for the measured cell impedance spectra at 0 V. Besides the ohmic resistance  $R_o$ , the equivalent circuit contains two parallel combinations of resistance  $R$  and a constant-phase element  $Q$ , which describes the polarization behavior at anode and cathode.

The first real-axis intercepts ( $R_o$ ) are the same under both polarization and non-polarization conditions,  $4.2 \Omega \cdot \text{cm}^2$  at  $750^\circ\text{C}$  and  $4.6 \Omega \cdot \text{cm}^2$  at  $800^\circ\text{C}$ . The majority of the high-frequency area specific resistance was contributed by the cell connecting lead, which was found to be about  $2.6 \Omega$  at room temperature. The total resistance of the connecting wires increased with operating temperature in part because a section of the platinum wire was heated with the cell in the furnace. As the temperature coefficient of resistance of platinum is  $0.00392^\circ\text{C}^{-1}$ , the increase in wire resistance is less than  $0.06 \Omega$  from  $750^\circ\text{C}$  to  $800^\circ\text{C}$ . However, the resistance increased by  $0.4 \Omega$  when the temperature increased from  $750^\circ\text{C}$  to  $800^\circ\text{C}$ . Therefore, the largest part of increase in the resistance is ascribed to increase in the contact resistance between Pt anode and the electrolyte as well as the electronic connection resistance between the current collector and Pt anode. As the data at  $800^\circ\text{C}$  were acquired after the I-V curve and impedance measurements at  $750^\circ\text{C}$ , the long exposure time and pre-polarization of the cell in the  $\text{H}_2\text{S}$  stream resulted in the formation of PtS, and consequently increased the instability of the Pt/YSZ interface and the electronic connection resistance at  $800^\circ\text{C}$ . This interpretation is supported by results

from experiments in which the cell was cycled between 750°C and 800°C, to be described below (Section 4.3.2.3).

The intercepts of the impedance spectra at the lowest frequencies determined at 0 V corresponds to the total cell resistance ( $R_t$ ), in which the polarization resistance ( $R_t - R_o$ ) was 5.1  $\Omega \cdot \text{cm}^2$  at 750°C and 4.3  $\Omega \cdot \text{cm}^2$  at 800°C (Figure 4-6a). The smaller polarization and total cell resistance at 800°C contributed to the higher maximum current density at this temperature. The similar maximum power densities at 800°C and at 750°C can be attributed to the mixed effects of the increased ohmic resistance and reduced polarization resistance. The first depressed semicircle for each temperature in Figure (4-6a) was assigned to the electrochemical process occurring at the cathode, while the second one arose from the anode reactions. This phenomenon is contrary to most standard solid oxide fuel cells operating on hydrogen fuel, where the hydrogen oxidation at Ni/YSZ cermet is typically faster than the oxygen reduction at LSM cathode, and accordingly is responsible for the semicircle at high frequencies in the complex plane plot [11]. Another abnormal behavior of the acquired impedance spectra in our experiment is that the anode polarization resistance increased with increasing temperature, which is inconsistent with the Arrhenius relationship. In contrast, the cathode polarization resistance decreased as temperature increased to 800°C, due to a reduction in activation energy. The increase of anode reaction resistance observed at 800°C can be ascribed to the deterioration of the platinum anode in the H<sub>2</sub>S streams.

#### *4.3.1.4 Identification of Limiting Factors to Cell Performance*

In order to identify the contribution of each cell component to overall cell

performance, a reference electrode made from Pt paste was applied to the cathode side of the cell. Figure 4-7 displays the various potential losses and the overall performance for this specific cell. The loss due to the resistance of the electrolyte is plotted based on its resistivity at 800°C (20  $\Omega\cdot\text{cm}$ ) and its thickness. The total cell ohmic resistance was determined from the first intercept of the impedance spectra, which is about 3.7  $\Omega\cdot\text{cm}^2$ . The cathode polarization curve was measured with the reference electrode placed at the same side of the electrolyte. As can be seen, anode polarization was responsible for a large fraction of the total voltage drop throughout the whole current region, whereas the cathode polarization made a smaller contribution to cell potential loss. The quasi-linear polarization curves indicate that the mass transfer limitations were minimal. The cell ohmic drop increased with increasing current and represented about 40 percent of cell voltage loss at the highest current densities. As discussed in Section 4.3.1.3, the majority of the ohmic loss is attributable to contact resistance between electrode and electrolyte or electrode and current collector as well as electronic resistance arising from the connecting wires. The electronic resistance is inherent in the experimental apparatus used in this experiment, but can be reduced by optimizing the cell design.

## **4.3.2 Use of Pure Hydrogen Sulfide as Fuel**

### *4.3.2.1 Cell Performance*

Figure 4-8 shows the voltage-current density relationship for a fresh fuel cell with the use of pure H<sub>2</sub>S feed at 750°C and 800°C. Initially, experiments were done at 750°C. Then the temperature was increased to 800°C for further tests. The cell voltage-current performance at each temperature unexpectedly was worse than that in 5% H<sub>2</sub>S feed.

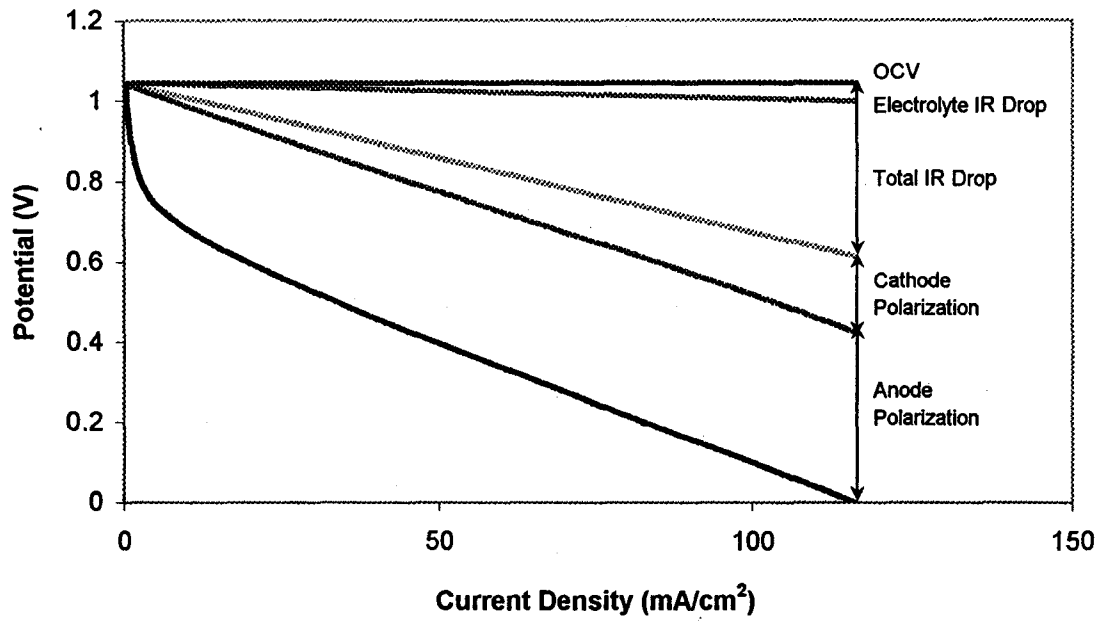


**Figure 4-7** Contribution of various component effects to polarization for a H<sub>2</sub>S-O<sub>2</sub> cell at 800°C

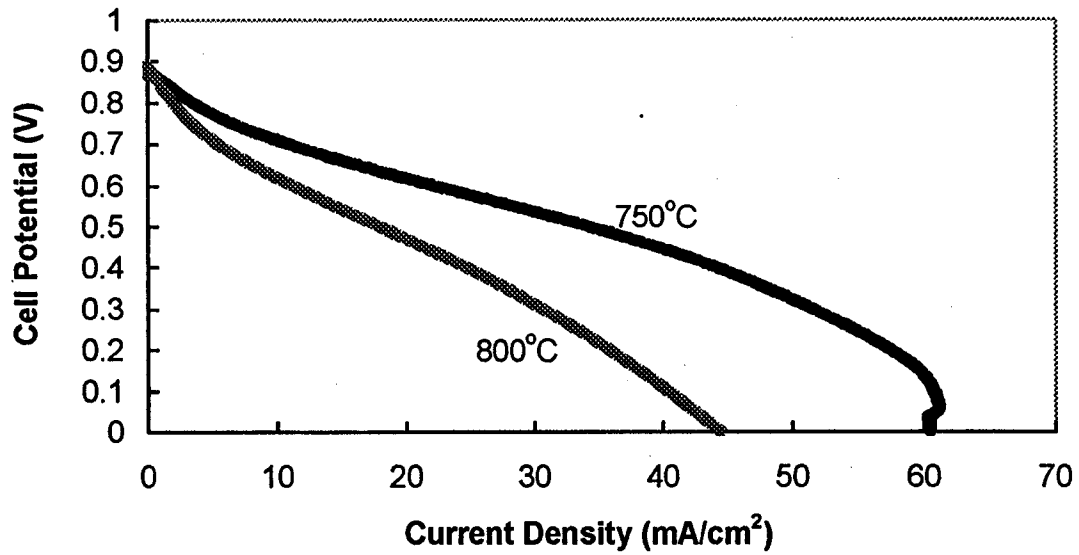


**Figure 4-8** Current-potential curves for a cell using pure H<sub>2</sub>S at 750°C and 800°C

The lower maximum current density in pure H<sub>2</sub>S than in diluted H<sub>2</sub>S is attributed to rapid platinum anode deterioration in the concentrated fuel stream. It was found that the platinum anode detached gradually from the YSZ electrolyte with time on stream. The curvature at the high-current end of the I-V curve at 750°C indicates the beginning of the detachment of the Pt anode and the occurrence of diffusion control. The appearance of diffusion polarization can be attributed to the slow transfer of H<sub>2</sub>S to the electrocatalytic active sites, which may be blocked by the excessive sulfur formation on the Pt surface at high current densities. Total lifetime of this cell under polarization condition at 800°C was about 6 hr, after which time the cell failed. After the test, the Pt anode was found to be completely detached from the electrolyte, while the bonding of the Pt cathode to the electrolyte remained intact.

#### *4.3.2.2 Impedance Characteristics*

A series of cell impedance spectra were measured at 800°C and at OCV. One measurement at OCV was conducted first; then the cell was polarized at a constant voltage of 0.6 V for 10 min. The system was then operated at OCV for about 30 min to allow equilibration, then the second measurement was taken at OCV. The cycle of polarization and equilibration followed by impedance measurement was repeated three times. After passing direct current through the cell, the polarization resistance at OCV was reduced significantly compared to the initial value, as shown in Figure 4-9. Though the change for the individual electrode cannot be estimated without use of a reference electrode, it can be concluded that the electrodes were activated by this procedure. The

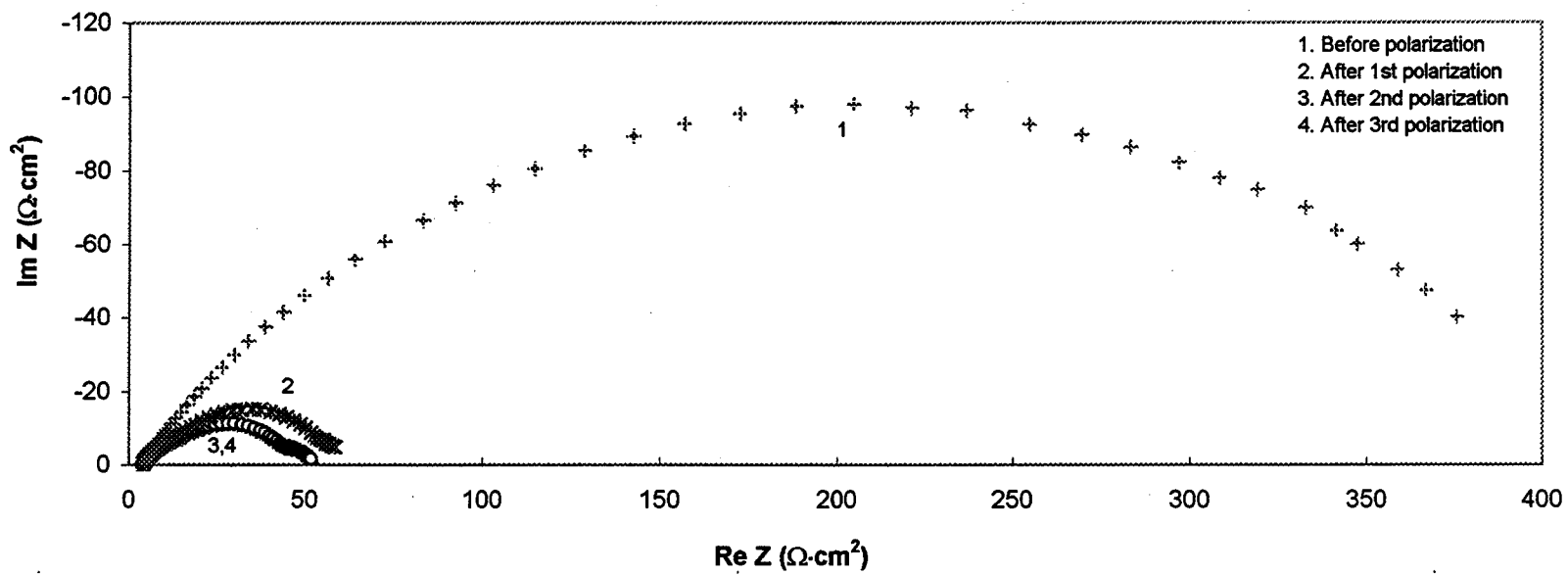


**Figure 4-9** Impedance spectra of the Pt/YSZ/Pt cell at OCV under the influence of an applied potential at 800°C

almost identical impedance spectra for the third and fourth measurement indicate that longer polarization time is not necessary to further activate the electrodes. A similar activation effect also has been reported as a common feature for LSM electrodes in solid oxide fuel cells [12-14]. However, the nature of the activation process has so far not been revealed. The activation effect explains why nominally identical electrodes prepared the same way do not always exhibit similar performance in an initial measurement, and why sometimes the same electrode renders better results for later measurements [14]. This suggests that the electrodes might not be at the same state of activation when the tests are conducted. Therefore, in order to obtain results which can be compared, each electrode has to be pretreated with the same amount of current to be sure they reach the same fully activated state.

The impedance spectra of the Pt/YSZ/Pt cell using pure H<sub>2</sub>S gas under polarization condition (at 0 V) are given in Figure 4-10. The electrical resistance of the wiring in this cell was lower than that in the previous cell using 5% H<sub>2</sub>S as fuel due to the use of shorter connecting wires. Again, the cell specific ohmic resistance  $R_o$  increased with temperature: the resistance at 800°C was almost two times larger than at 750°C. During these tests, IS data at 800°C were acquired after the measurements of I-V curve and impedance at 750°C. Consequently, the resistance of  $R_o$  was found to be larger at higher temperature due to the prior deterioration of the contacts (Figure 4-10). Further, the I-V relationship (Figure 4-8) determined in polarization experiments also showed abnormal behavior: the maximum current density decreased with increasing temperature.

The IS plots using pure H<sub>2</sub>S as feed (Figure 4-10) could not be easily deconvoluted into a series of semicircles. However, the total cell resistance ( $R_t$ ) was

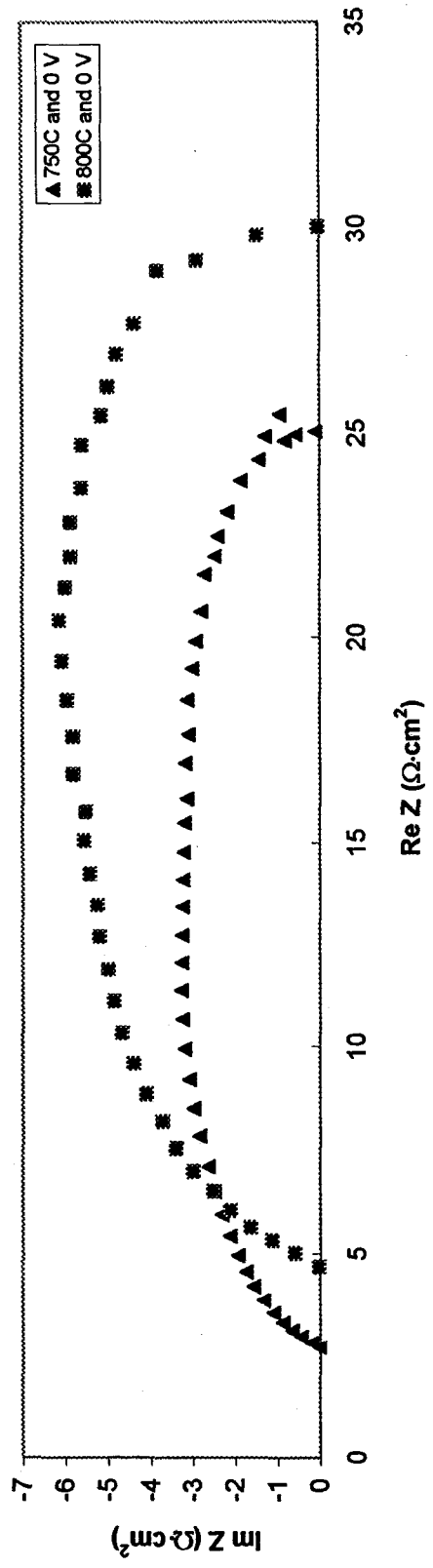


**Figure 4-10** Impedance spectra of the Pt/YSZ/Pt cell using pure H<sub>2</sub>S fuel at 750°C and 800°C under polarization at 0 V

readily distinguished at the low frequency intercept for each temperature, and was found to be higher than the corresponding value in Figure 4-6a for use of 5% H<sub>2</sub>S feed. The increase in resistance was consistent with degradation of the Pt anode in the H<sub>2</sub>S stream, as discussed above. That is, Pt anode degradation in the pure H<sub>2</sub>S stream was more pronounced than in the 5% H<sub>2</sub>S stream. The formation of PtS at the Pt/YSZ interface led to an increase of contact resistance between the Pt anode and YSZ electrolyte. Evidence will be shown in Figure 5-5 and details will be discussed in Chapter 5. Thus, using pure H<sub>2</sub>S adversely affected cell performance due to rapid formation of PtS, which had the effect of deactivation of the anode electrocatalyst and increasing the contact resistance.

#### *4.3.2.3 Stability Test of Pt Anode Using Impedance Technique*

Hydrogen sulfide in the anode feed attacked the Pt surface to form PtS at elevated temperatures, and thereby reduced electrical conductivity. Further, it was observed that the high-frequency intercept ( $R_o$ ) of impedance spectrum at different temperatures changed with duration of exposure and polarization time (Figure 4-11 and Figure 4-12).

Figure 4-11 shows the change in cell ohmic resistance ( $R_o$ ) with exposure time under open circuit conditions using pure H<sub>2</sub>S feed. The temperature of the cell was cycled three times per day between 750°C and 800°C, starting at either 750°C or 800°C in different experiments. The slight variance in values for  $R_o$  (less than 0.05  $\Omega\cdot\text{cm}^2$ ) at the same temperature between the three testing times indicated that thermal cycling had no major effect on cell performance. The higher resistance at 750°C compared with 800°C was consistent with the lower ionic conductivity of YSZ membrane at this temperature. During operation over 5 days without polarization,  $R_o$  increased by 1.2  $\Omega\cdot\text{cm}^2$  at 750°C,

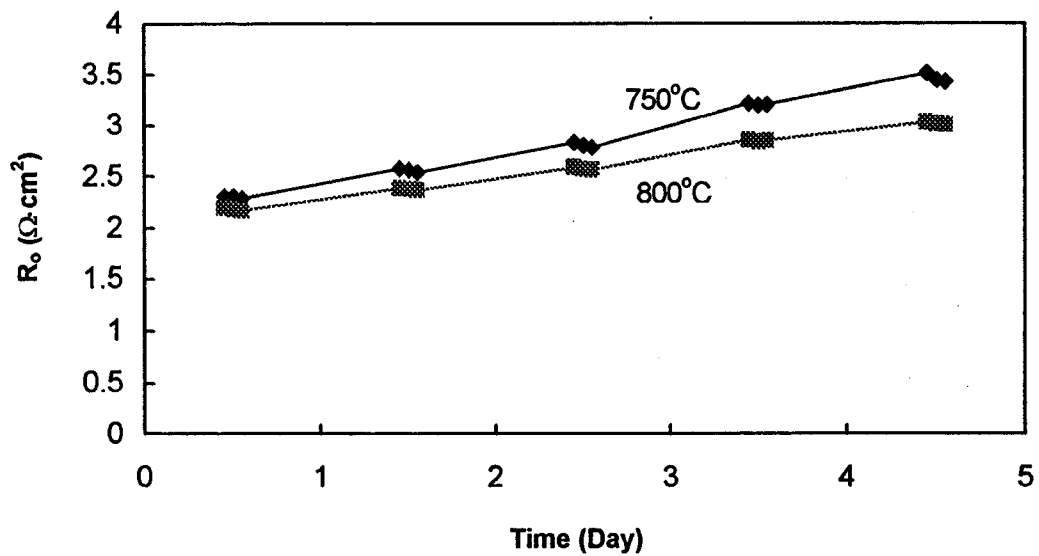


**Figure 4-11** Cell specific ohmic resistance ( $R_o$ ) changes with exposure time under open circuit conditions when using pure  $\text{H}_2\text{S}$  feed

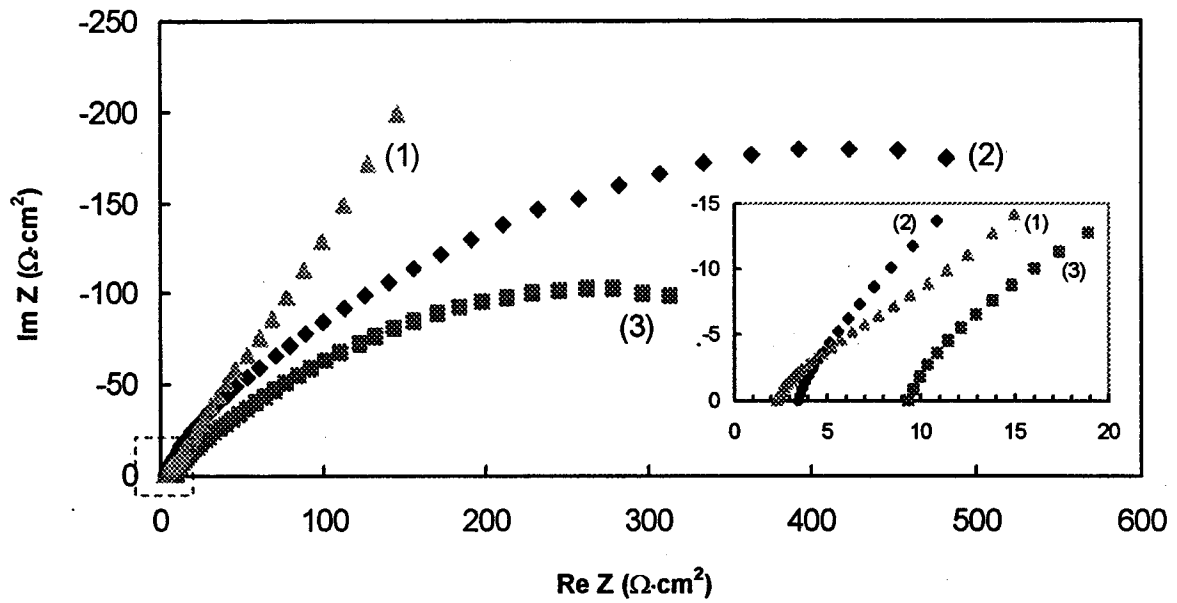


**Figure 4-12** Impedance spectra of a Pt/8% YSZ/Pt cell using pure H<sub>2</sub>S at 750°C: (1) first day exposure in pure H<sub>2</sub>S without polarization; (2) after 5 day operation without polarization; (3) after polarization for 20 min; Inset: expanded region 0-20 Ω·cm<sup>2</sup>

as shown in Figure 4-12, which is attributable to formation of PtS, as described above. However, increased polarization was the primary source of the large increment in the resistance ( $R_o$ ): about  $5.7 \Omega\text{-cm}^2$  after polarization at 0.4 V for 20 min, as displayed in the inset of Figure 4-12. Polarization aggravated the instability of the electrochemical interface between anode and membrane and thus accelerated degradation of the Pt anode.

### 4.3.3 Gas Analysis

Both 5% H<sub>2</sub>S balanced with nitrogen and pure H<sub>2</sub>S were utilized as anode feed in order to obtain an idea of how the Pt/YSZ/Pt fuel cell system would respond to diluted and concentrated streams of hydrogen sulfide. The anode outlet gas was passed through a sulfur trap to remove the product elemental sulfur produced. The tubing segments between the exit port of anode chamber and the sulfur condenser were wrapped with heating tape. The concentrations of hydrogen, hydrogen sulfide and sulfur dioxide under different fuel cell operating conditions were determined by using two on-line gas chromatographs. A SCD was employed to get a better estimate of the concentrations of sulfur species in the effluent of diluted H<sub>2</sub>S streams.

The gas analyses showed that the hydrogen sulfide concentration at open circuit conditions typically decreased with increasing operating temperature, whereas the hydrogen yield was enhanced at higher temperatures. This was in accordance with the thermal decomposition of hydrogen sulfide catalyzed by the porous Pt electrode (reaction 3-6) [15]. Detection of the presence of hydrogen in the exit gases indicated that H<sub>2</sub> was an electroactive species contributing to the experimental open circuit voltages. It was also observed that both hydrogen sulfide and hydrogen were consumed as current was

generated by the cell, which was more evident for diluted H<sub>2</sub>S streams due to high fuel utilizations in the single cell arrangement of the present system. Therefore, a dilute stream consisting of 5% H<sub>2</sub>S was used more extensively in subsequent experiments.

Figure 4-13 shows the consumption rate of hydrogen, as a function of current density with 5% hydrogen sulfide as fuel at 800°C. Increasing cell current caused an increase in the hydrogen reaction rate, which verified the occurrence of hydrogen oxidation by reaction (3-7). The rapid increase in  $r_{H_2}$  at low current densities suggested that hydrogen was active at the three phase boundaries. At a total cell current density of 26 mA/cm<sup>2</sup>, about 75% of the initial amount of hydrogen arising from reaction (4-4) was electrochemically oxidized. It appeared that the hydrogen reaction rate nearly reached a plateau at high current densities, indicating that hydrogen present at the anode was almost completely consumed.

Along with the hydrogen oxidation reaction there were three other possible electrochemical reactions that could take place at the anode with hydrogen sulfide as fuel. Two of these, reactions (3-2) and (3-3), are the direct oxidation of hydrogen sulfide to either elemental sulfur or sulfur dioxide and water vapor. The sulfur formed from the electrocatalytic oxidation of hydrogen sulfide in reaction (3-2) and the hydrogen sulfide decomposition in reaction (3-6) can be further oxidized to sulfur dioxide and spontaneously generate electricity via reaction (3-8). Whether sulfur dioxide is produced in one step via reaction (3-3) or two steps with sulfur as the intermediate product, reactions (3-2) or (3-6) followed by (3-8), is difficult to resolve because both overall processes involve the transfer of six electrons and the reactants and final products are

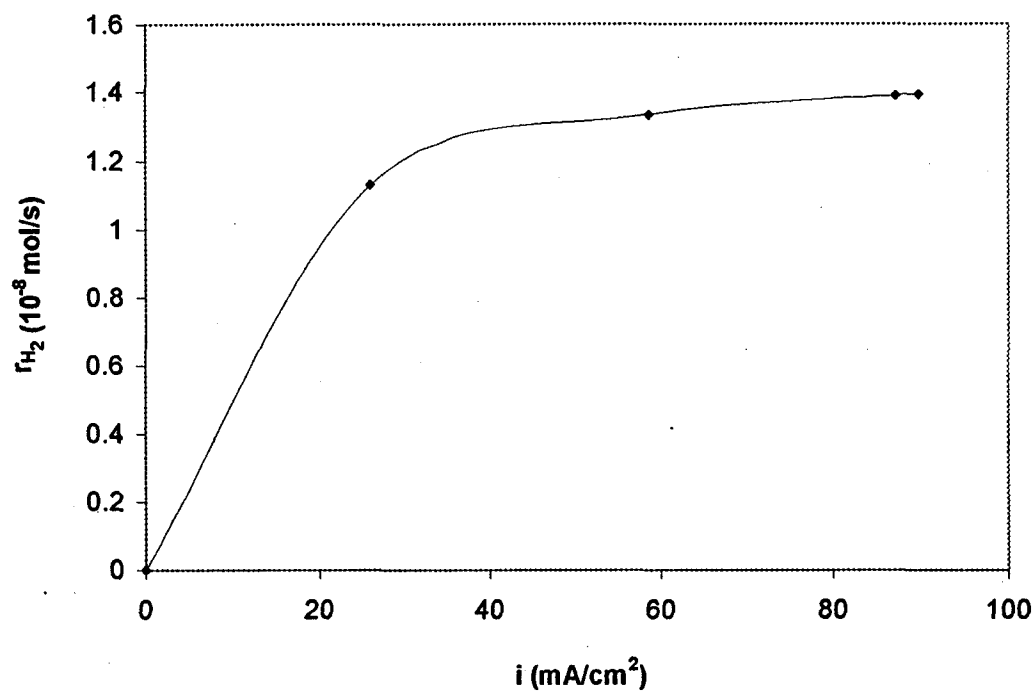


**Figure 4-13** Reaction rate of H<sub>2</sub> as a function of cell current for a 5% H<sub>2</sub>S fuel stream at 800°C

exactly the same. However, this matter was not a priority. Herein, the higher concern was to determine whether utilizing hydrogen sulfide in a solid oxide fuel cell resulted in the production of sulfur or sulfur dioxide.

Figure 4-14 displays the variation of the  $\text{H}_2\text{S}$  reaction rates with corresponding current density for 5%  $\text{H}_2\text{S}$  fuel stream at a temperature of  $800^\circ\text{C}$ . The current density was solely from the hydrogen sulfide source, i.e., the current density contributed by the electrochemical oxidation of hydrogen had been deducted from the total cell current density. The purpose of using the reduced current density was to eliminate any misunderstanding so that the investigation of the possible  $\text{H}_2\text{S}$  reaction route could be made more accurately. Based on the initial concentration at open circuit conditions, the expected stoichiometric reaction rates of  $\text{H}_2\text{S}$  were also plotted in Figure 4-14. For example, if the partial oxidation of hydrogen sulfide to sulfur (reaction (4-7)) was the only one taking place at the anode, the relationship of the  $\text{H}_2\text{S}$  reaction rate with current would follow the stoichiometric trend where the number of electrons transferred per molecule of  $\text{H}_2\text{S}$  is two. However, the experimental determined reaction rates of hydrogen sulfide were not fully consistent with either route throughout the whole current region.

As can be seen in Figure 4-14, at low current density, the  $\text{H}_2\text{S}$  consumption rate coincided with that predicted for the  $n=2$  line, suggesting that sulfur was the final product. Similar to that of hydrogen, electrochemical oxidation of  $\text{H}_2\text{S}$  is rapid. About 70%  $\text{H}_2\text{S}$  was consumed at the total cell current density of  $26 \text{ mA/cm}^2$ . Since both hydrogen and hydrogen sulfide were shown to be strongly electroactive species, it was

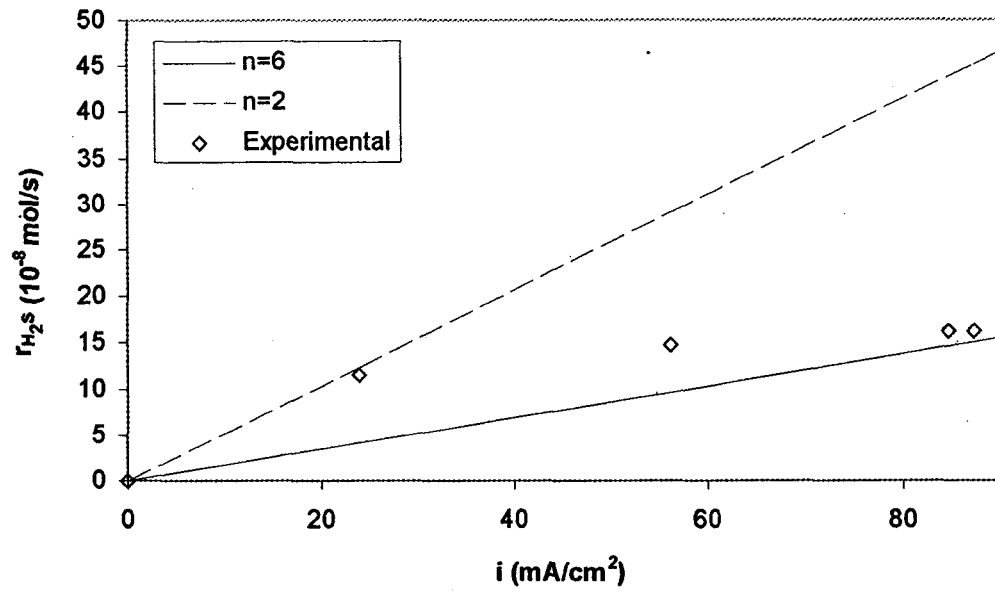


**Figure 4-14** Reaction rate of H<sub>2</sub>S as a function of current for a 5% H<sub>2</sub>S fuel stream at 800°C as well as the expected stoichiometric values

impossible to identify which one was dominant in the half-cell reactions from the acquired data. The data obtained at intermediate current density fell between the two lines for  $n=2$  and  $n=6$ , which indicated that there was a combination of the two reactions occurring in the cell. The consumption rate of hydrogen sulfide at high current densities most closely followed the expected response for formation of sulfur dioxide as the only product. However, it was not possible to discern whether sulfur dioxide was produced from reaction (3-3) or as a result of reaction (3-2) and (3-8). The maximum rate was approached at the highest current, indicating that the fuel cell was operating at very high fuel utilization.

Figure 4-15 presents the generation rate of  $\text{SO}_2$  in the anode chamber, measured at  $800^\circ\text{C}$  for 5%  $\text{H}_2\text{S}$  feed stream. The current contribution from the hydrogen oxidation was also subtracted from the total cell current, and the resulting current data are for reaction of hydrogen sulfide alone. Initially, there was no production of  $\text{SO}_2$  at low current, which agreed with the above finding that only the half-cell reaction producing sulfur proceeded at the anode under this condition. With increasing current, sulfur dioxide was generated and the amount approached the value expected from the complete oxidation of  $\text{H}_2\text{S}$  to  $\text{SO}_2$ , with corresponding currents. At high current densities, the rates of  $\text{SO}_2$  production are well above the line for  $n=6$ , suggesting that the electrochemical oxidation of sulfur to sulfur dioxide (reaction 3-8) also was taking place at the anode.

When pure  $\text{H}_2\text{S}$  was used as the fuel, sulfur dioxide was never detected in the anode exit gases. This is not surprising since, at high concentrations of  $\text{H}_2\text{S}$  and elevated temperatures, any  $\text{SO}_2$  generated would further chemically react rapidly with the excess hydrogen sulfide present via the Claus process, reaction (1-2).

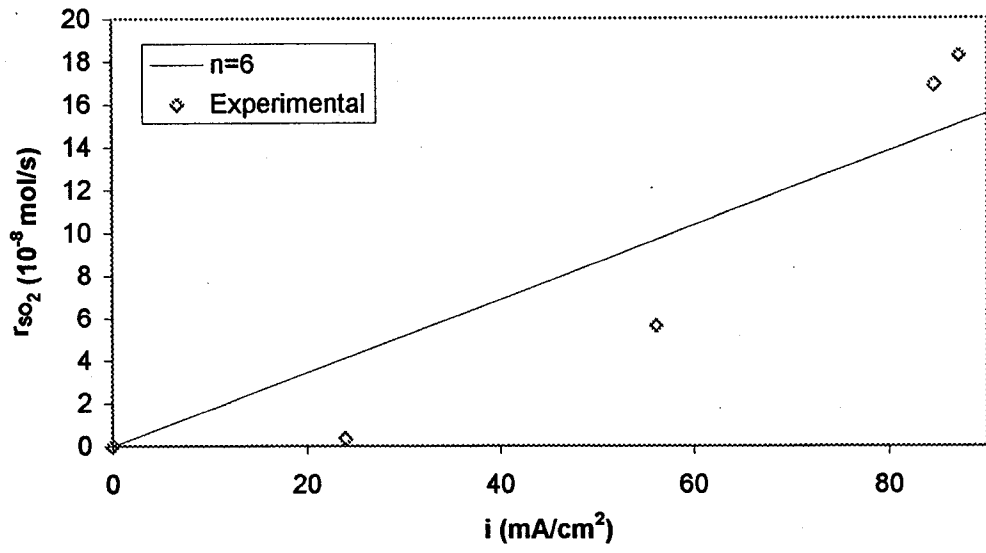


**Figure 4-15** Comparison of SO<sub>2</sub> generation rate vs. current for a 5% H<sub>2</sub>S fuel stream at 800°C to calculated stoichiometric values

#### 4.4 Conclusions

The promising values for current and power output using the present system show that hydrogen sulfide has potential value as a suitable fuel for a zirconia-based solid electrolyte fuel cell operating at the temperature range of 750°C-850°C. However, platinum deposited on YSZ is not a suitable anode material for used in an H<sub>2</sub>S stream. The formation of PtS contaminates the anode surface and increases the interface resistance between Pt and YSZ, ultimately leading to detachment of the Pt anode from the electrolyte. While electrochemical polarization accelerates degradation of the Pt anode significantly, a short-time low current polarization may activate some electrodes. Superior current density and longer lifetime of the fuel cell are found when using dilute H<sub>2</sub>S feed compared with using pure H<sub>2</sub>S feed. Alternative anode catalyst systems are required, that do not deteriorate over time in an atmosphere of H<sub>2</sub>S. Electrochemical impedance analysis shows that ohmic drops arising from electrical wire connections and contact resistance also contribute a significant part of the overall cell voltage drop. Shorter connecting wires and improved electrical contacts are both required to improve cell performance.

Gas analysis results have shown that both hydrogen sulfide and hydrogen, formed from the decomposition of H<sub>2</sub>S, were actively involved in the half-cell reactions occurring at the anode. However, it is not possible to unequivocally identify the dominant species based on the acquired data. For dilute H<sub>2</sub>S streams, it appears that the product distribution changes from primarily sulfur to primarily sulfur dioxide with increasing

current. No sulfur dioxide was detected in the anode effluents for pure H<sub>2</sub>S feed. These results can be attributable to consumption of SO<sub>2</sub> in the Claus reaction.

## References

- [1] O. Yamamoto, *Electrochimica Acta*, **45**, 2423 (2000).
- [2] D. Peterson and J. Winnick, *Journal of the Electrochemical Society*, **143**, L55 (1996).
- [3] D. R. Peterson and J. Winnick, *Journal of the Electrochemical Society*, **145**, 1449 (1998).
- [4] I. V. Yentekakis and C. G. Vayenas, *Journal of the Electrochemical Society*, **136**, 996 (1989).
- [5] J. G. McCarty, K. M. Sancier and H. Wise, *Journal of Catalysis*, **82**, 92 (1983).
- [6] H. Wang, Q. Zhang, I. G. D. Lana and K. T. Chuang, *Journal of Chromatographic Science*, **36**, 605 (1998).
- [7] J. O'M. Bockris and S. Srinivasan., 'Fuel Cells: Their Electrochemistry', Chapter 4, McGraw-Hill, New York (1969).
- [8] T. J. Kirk and J. Winnick, *Journal of the Electrochemical Society*, **140**, 3494 (1993).
- [9] S. J. Visco, L. Wang, S. De Souza and L. C. De Jonghe, *Materials Research Society Symposia Proceedings*, **369**, 683 (1998).
- [10] J. R. Macdonald, 'Impedance Spectroscopy: Emphasizing Solid Materials and Systems', John Wiley & Sons, Inc. (1987).
- [11] M. Liu and A. Khandkar, *Solid State Ionics*, **52**, 3 (1992).

- [12] M. J. Jørgensen, S. Primdahl and M. Mogensen, *Electrochimica Acta*, **44**, 4195 (1999).
- [13] A. J. McEvoy, *Proceeding of 7th SOFC International Energy Agency Workshop*, Wadahl, Norway, p127 (1994).
- [14] T. Jacobsen, B. Zachau-Christiansen, K. West and S. Skaarup, *Proceeding of 2nd Nordic Symposium on High Temperature Fuel Cells*, March Geilo, Norway, p139, (1994).
- [15] M. E. D. Raymont and J. B. Hyne, *Alberta Sulfur Research Ltd. Quarterly Bulletin*, **12**(2), 3 (1975).

## CHAPTER 5

# USE OF AN INTERMEDIATE TiO<sub>2</sub> LAYER TO IMPROVE STABILITY OF PLATINUM ANODE CATALYST IN A H<sub>2</sub>S-Air SOFC

### 5.1 Introduction

Due to its stability and catalytic activity, platinum is commonly used as anode catalyst and/or current collectors in solid oxide fuel cells operating on hydrogen sulfide fuels [1-8]. It has been demonstrated in previous studies that hydrogen sulfide is a potentially valuable fuel in fuel cells with Pt anode catalyst. However, hydrogen sulfide can attack Pt surfaces at elevated temperatures and thereby cause instability of the interface between Pt anode and YSZ electrolyte [8]. Under the influence of current and high concentrations of H<sub>2</sub>S, the Pt anode deteriorates rapidly and ultimately leads to a significant degradation in cell performance.

In this chapter, I will identify the cause of the instability of Pt anode by correlating cell performance in pure H<sub>2</sub>S streams with physical and chemical characterization of the anode materials. Then I will show that it is possible to take advantage of the high electrocatalytic activity of platinum for the oxidation of hydrogen sulfide, by improving its stability by applying a thin (submicron) intermediate layer of titania between the platinum anode and YSZ electrolyte. Cell performance and stability of the supported platinum anode catalysts under pure H<sub>2</sub>S atmosphere and operating

temperatures of 700-850°C will be described and the role of the intermediate titania layer will be discussed.

## **5.2 Experimental**

### **5.2.1 Cell Preparation and Construction**

Tape-casted 8YSZ disks were again used as the electrolytes, which had a thickness of 0.2 mm and a diameter of 25.4 mm. Platinum cathode and anode were prepared by following the same procedure as stated in Chapter 4, section 4.2.1. The superficial surface area of each electrode was about 1 cm<sup>2</sup>. Platinum mesh placed in intimate contact with the surface of anode or cathode acted as current collector. Platinum leads were spot-welded to the meshes to carry the current to a load exterior to the cell.

Details of the experimental fuel cell system construction have been described previously (Chapter 4, section 4.2.2). However, after initial trials mainly performed using dilute H<sub>2</sub>S streams, it was found that the self supporting YSZ electrolytes were very fragile and easy to crack, leading to failure during many cell tests. To solve this problem, a Pyrex holder was designed to provide mechanical support for the electrolyte, as shown in Figure 5-1. The cathode side of the electrolyte was bonded to the glass holder using the ceramic adhesive, Aremco 503. Then the holder was mounted and sealed to the outer tube of each chamber with the same sealant. Nitrogen was fed into the anode compartment until the cell reached operating temperature, so as to prevent undesirable low-temperature reactions. In all experiments, once the prescribed temperature had been reached, pure hydrogen sulfide was fed as fuel and air was used as the oxidant.

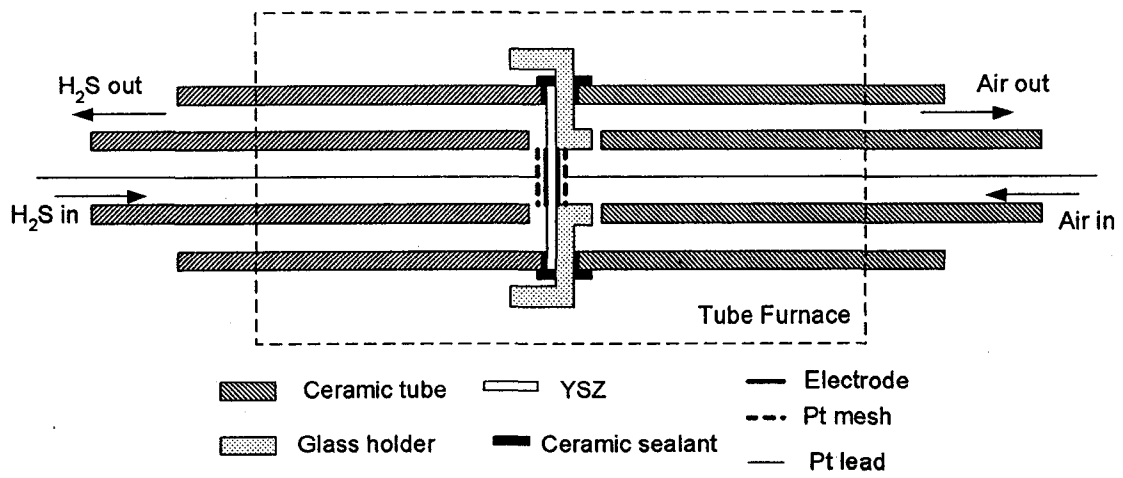


**Figure 5-1** Configuration of modified H<sub>2</sub>S-air fuel cell with a glass holder

### 5.2.2 Preparation of TiO<sub>2</sub>/YSZ Wafer

A titania interlayer was applied to the anode surface of the YSZ wafer using sol-gel and paste painting techniques, before depositing the Pt anode. Titania sol was made as described elsewhere [9] and spin-coated onto one surface of the electrolyte. The TiO<sub>2</sub>/YSZ wafer was fired in air at a heating rate of 3°C/min, and then held at 900°C for 2 h. The TiO<sub>2</sub> layer formed at the YSZ surface has a typical thickness of *ca.* 0.2-0.5 μm using sol-gel technique and 0.5 μm by paste painting. Titania in this layer was shown by XRD to have a rutile structure. The sintering temperature of the TiO<sub>2</sub> interlayer was maintained below 1000°C to minimize penetration of Ti ions into YSZ [10], as described below.

### 5.2.3 Electrochemical Measurements

The open circuit voltage (OCV) of the fuel cell was monitored using a Keithley 199 digital multimeter. Potentiodynamic current-potential measurements were conducted using a Pine AFRED5 potentiostat in conjunction with a Virtual-Bench data acquisition system to acquire data automatically. Cell impedance analysis was carried out using a Gamry CMS 100/300 impedance measurement system and a Stanford SR810 DSP Lock-in amplifier.

### 5.2.4 Characterization of Solids

Scanning Electron Microscopy (SEM) and Energy Dispersive X-ray (EDX) measurements were conducted using a Hitachi Model S-2700 Scanning Electron

Microscope and PGT Imix system with a Prism IG. XRD spectra were obtained using a Rigaku Rotaflex X-ray diffractometer.

### 5.3 Results and Discussion

#### 5.3.1 Cell Performance and Stability of Pt anode in Pure H<sub>2</sub>S Stream

Previously we had shown that pure H<sub>2</sub>S feed gave a reduced cell performance when compared with use of 5% H<sub>2</sub>S feed [8]. After further investigation, it was found that the current-voltage performance varied with the exposure time of the anode to pure H<sub>2</sub>S streams prior to data acquisition. Cell performance obtained after exposing the anode to pure H<sub>2</sub>S atmosphere for a prolonged period of time was usually worse than that of a fresh fuel cell and current-potential plots often showed diffusion tails. Figure 5-2 presents typical current-voltage curves for Pt anodes using pure H<sub>2</sub>S feed at different temperatures. The data acquisition started at 700°C, after providing pure H<sub>2</sub>S gas for about 5 h. Clearly, the curves at operating temperatures of 700°C to 800°C show a precipitous decline in the high current density range, which is characteristic of mass transport limitation [11]. From 750°C to 850°C, the voltage-current performance of the H<sub>2</sub>S-air fuel cell improved with increasing temperature. However, at 900°C, the voltage-current performance (curve 5 in Figure 5-2) dropped significantly. This decline was irreversible, *i.e.* the original performance could not be restored by reducing the temperature of operation. After the experiment at 900°C, it was found that the cell had failed.

The observed mass transport limitations at temperatures lower than 850°C can be ascribed to a reduction in active reaction sites. Hydrogen sulfide is known to chemisorb

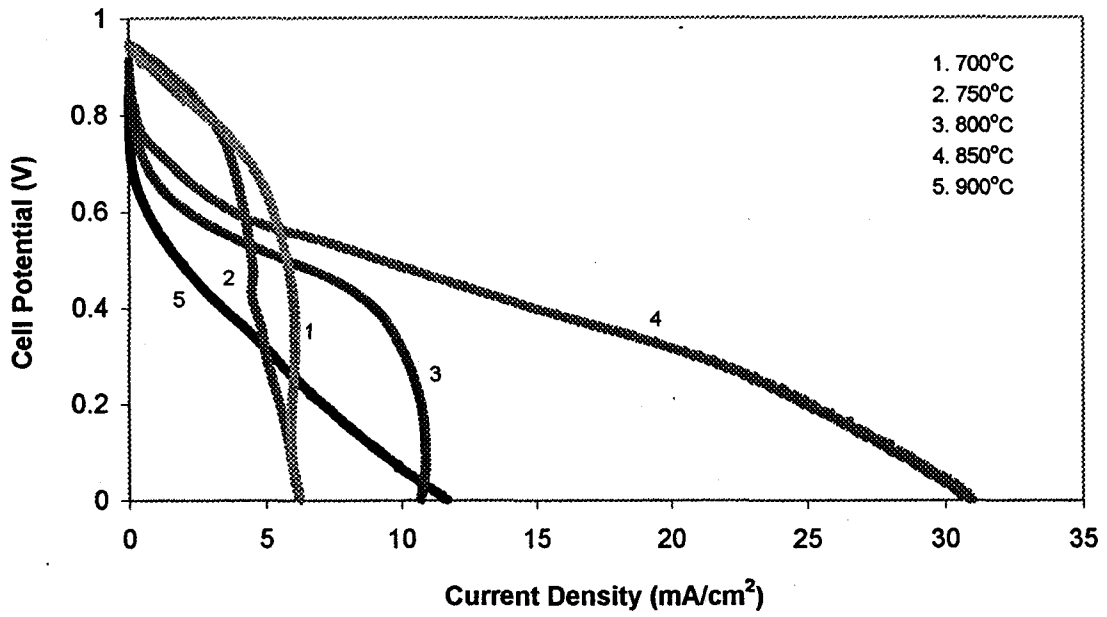


**Figure 5-2** Relationship of current density to cell potential as a function of temperature after prolonged exposure time in pure H<sub>2</sub>S stream

dissociatively on platinum and to form multilayer adsorbed sulfur “islands” [3], which may block the active reaction sites on the electrode. Moreover, the platinum surface can reversibly form platinum sulfide (PtS) in a H<sub>2</sub>S atmosphere at elevated temperatures. The heat of the bulk sulfide formation is lower than the heat of sulfur chemisorption at half coverage [12]. When the exposure time in the concentrated H<sub>2</sub>S stream is extended, more active Pt sites are covered by sulfur, and more PtS will be formed. Both effects reduce the number of available active Pt sites and impede the transport of the reactant gas onto the three-phase reaction zone, and diffusion of the products away those sites. Thermodynamic calculations indicate that the equilibrium content of PtS exponentially decreases with increasing temperature (Figure 5-3), due to thermal decomposition of PtS into sulfur vapor and platinum. However, the initial sharp voltage drop at higher temperatures 800-900°C in the low current region (Figure 5-2) indicated the lack of electrocatalytic activity, suggesting that the poisoning of Pt catalyst was more severe at such temperatures. Therefore, PtS formation was not reduced at higher temperatures as expected from the thermodynamic calculations. As shown in Figure 5-2, the maximum current density increased with increasing temperature from 750°C to 850°C. This probably was attributable to the desorption of sulfur from the active sites at three-phase boundary at higher temperatures, resulting in reduced concentration polarization. No obvious mass transport limitation was observed at 850°C. The reduced cell performance at 900°C is ascribed to deterioration of the interface between the Pt anode and the electrolyte after polarization at 850°C. Impedance spectroscopy measurements revealed that the cell specific ohmic resistance increased from 3.3 Ω·cm<sup>2</sup> at 850°C to about 8 Ω·cm<sup>2</sup> at 900°C. In contrast, there was no increase in cell ohmic resistance as the

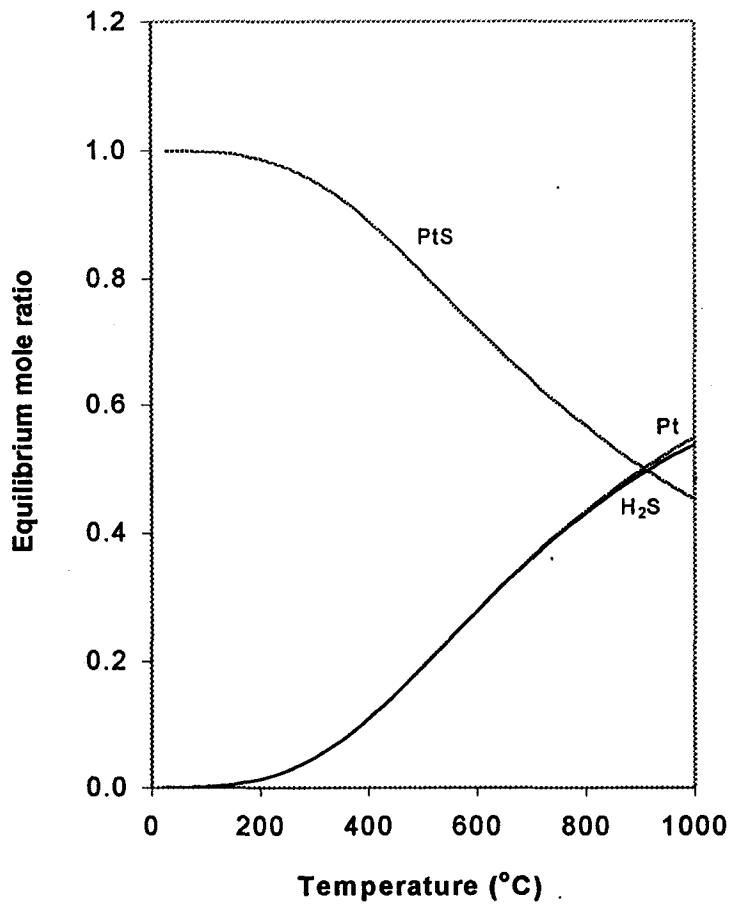


**Figure 5-3** Equilibrium components in the system Pt/PtS/H<sub>2</sub>S as a function of temperature (HSC Chemistry, Version 1.12, Outokumpu Research)

the temperature was increased to 750°C and only slightly increased by about 0.6  $\Omega\cdot\text{cm}^2$  from 750°C to 850°C, due to the low maximum current density at temperatures below 850°C.

Further evidence for degradation of the Pt anode due to contamination in pure H<sub>2</sub>S stream was demonstrated by the current-voltage curves for operation over an extended time at 700°C (Figure 5-4). Curve 2 was recorded 5 h later than curve 1, during which the cell was exposed to pure H<sub>2</sub>S feed and operated for measuring voltage-current curves several times. It can be seen that the maximum current density for the cell operated for 6 h is just one-tenth the value obtained after 1 h operation. Curve 3 shows the voltage-current performance after switching the feed gases to both chambers from H<sub>2</sub>S and air to H<sub>2</sub>, and polarizing the electrode between 1.0 and -1.0 V vs. H<sup>+</sup>/H<sub>2</sub> electrode at 20 mV/s for one cycle. Voltage-current performance was partially regenerated when the catalyst surface was polarized in hydrogen atmosphere at 700°C. Polarization of the contaminated electrode in hydrogen partly cleaned the platinum surface and restored the cell performance to a certain degree.

After completion of the H<sub>2</sub>S-air fuel cell tests, the Pt anode was easily peeled off from the YSZ electrolyte, suggesting that the anode was no longer strongly bonded to the electrolyte. The postmortem XRD analysis of the Pt anode showed that PtS had formed on the electrode (Figure 5-5). On the YSZ surface, Pt, PtS and YSZ were all present. However, no new zirconia-based phase was detected on YSZ, which showed that hydrogen sulfide did not affect the cubic fluorite structure of YSZ during the experiment.

The poor voltage-current performance of the H<sub>2</sub>S-air fuel cell at 900°C (Figure 5-2) was a direct consequence of detachment of the Pt anode from the YSZ wafer. Anode

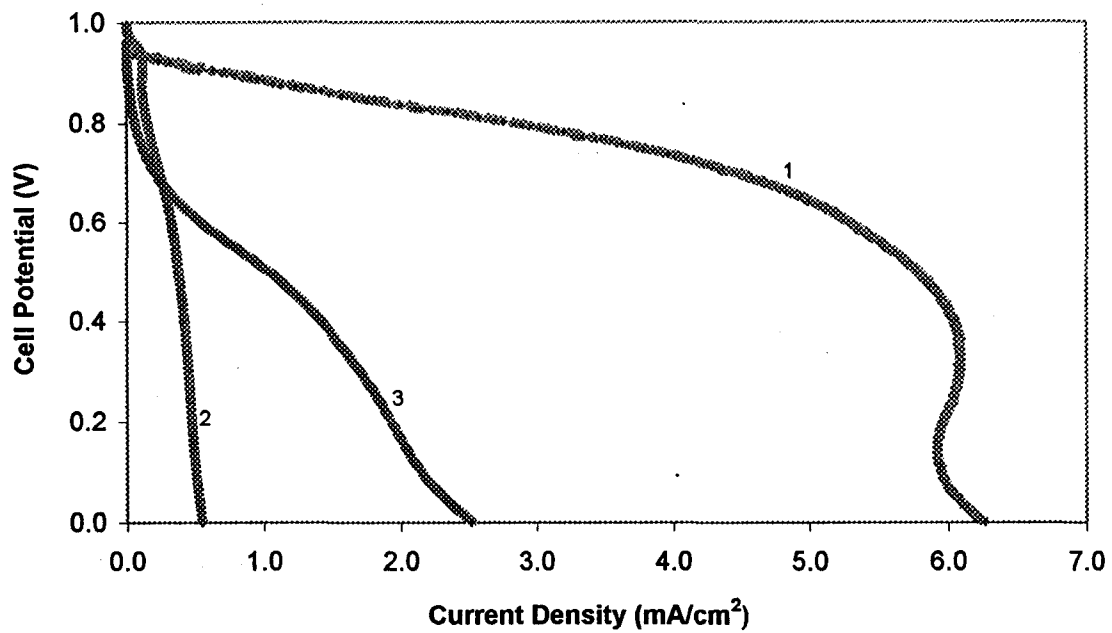


**Figure 5-4** Current-voltage curves for a H<sub>2</sub>S-air fuel cell at 700°C with pure H<sub>2</sub>S feed. Curve 1: after 1 h operation; Curve 2: after 6 h operation; Curve 3: after polarization of the cell in H<sub>2</sub> atmosphere

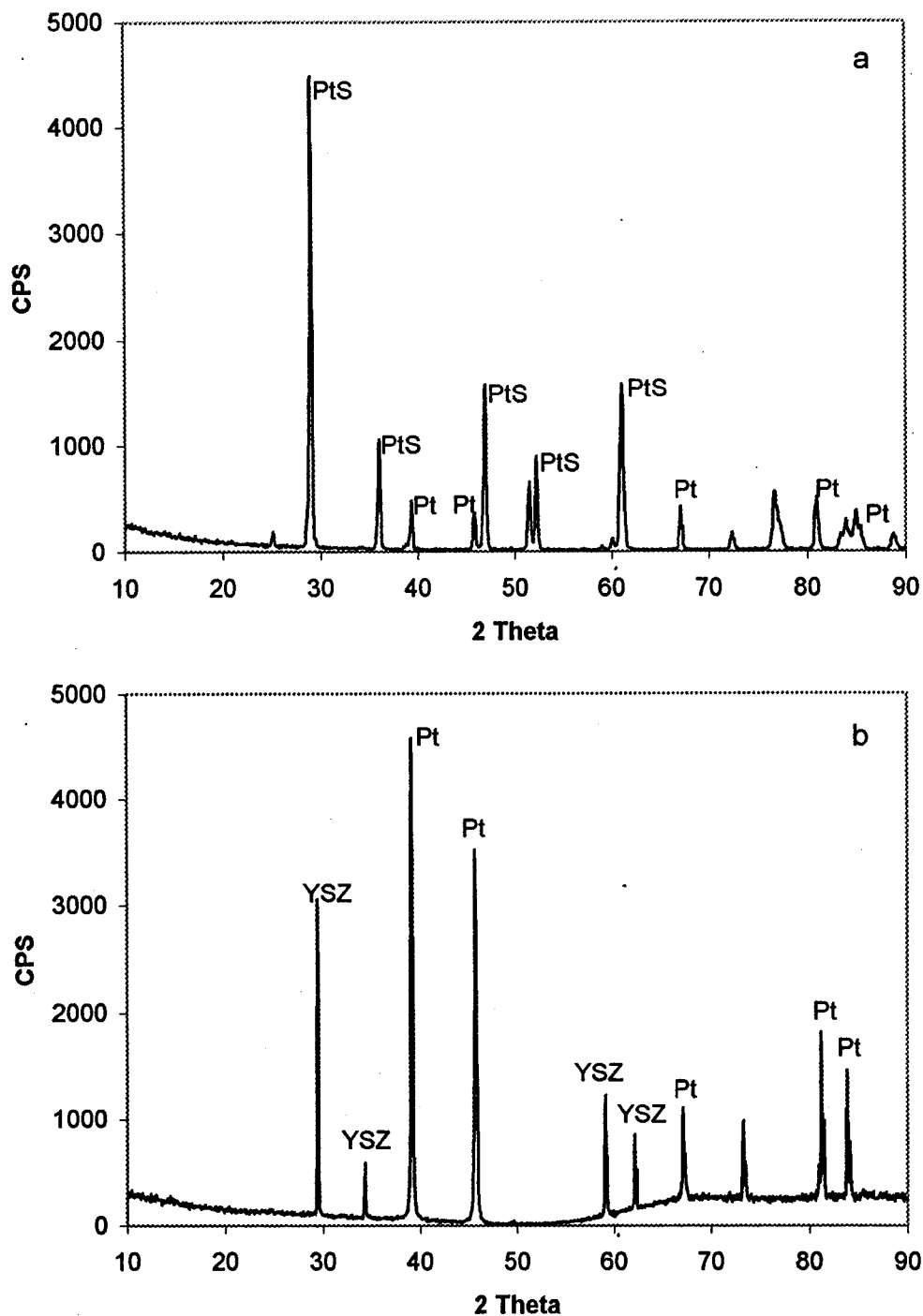


**Figure 5-5** XRD spectra of Pt anode and YSZ surface after fuel cell test in pure H<sub>2</sub>S stream: (a) disconnected Pt anode cooled down without passing N<sub>2</sub>; (b) anodic surface of YSZ after cooling down under N<sub>2</sub>

detachment is ascribed to the formation of PtS at the Pt/YSZ interface during the electrochemical reaction processes. At high temperatures, dynamic reversible formation and decomposition of PtS on the platinum surface in pure H<sub>2</sub>S stream affected bonding of Pt to YSZ, and thereby caused instability of the Pt/YSZ interface. The degradation rate of Pt anode depended on the operating current density. A high current density accelerated the mass transport of H<sub>2</sub>S towards the Pt/YSZ interface and formation of PtS, and hence accelerated detachment of the Pt anode from the YSZ wafer. On the cathode side of the electrolyte, no detachment of the Pt cathode from the YSZ interface was ever detected. Thus the detachment of the anode was caused directly by the presence of H<sub>2</sub>S.

When the cell was cooled down slowly under a N<sub>2</sub> atmosphere, no PtS was detected on the anode surface by XRD characterization, which indicated that all PtS formed during the fuel cell operation had decomposed. It was also found that the detached anode had adhered to the Pt mesh current collector. The stability of the Pt-Pt connection is attributed to bonding of the Pt-Pt surface when sulfur in PtS was baked out from the adjacent surfaces of the collector and the anode at high temperatures (700°C to 900°C) under N<sub>2</sub>. A fortuitous consequence was that contact resistance between current collector and the electrode in a H<sub>2</sub>S-air fuel cell was reduced by the sequential exposure to H<sub>2</sub>S atmosphere and baking in N<sub>2</sub>. Impedance measurements showed that the electronic resistance in the H<sub>2</sub>S-air fuel cell had decreased 20% after treating in H<sub>2</sub>S then baking in N<sub>2</sub>, from 2.8 Ω to 2.2 Ω.

### **5.3.2 Improvement of Anode-YSZ Stability by Interposition of a TiO<sub>2</sub> Layer**

The above experiments revealed that the Pt/YSZ interface was unstable in a high

temperature H<sub>2</sub>S environment. The effect of interposition of an intermediate layer between the Pt anode and the YSZ wafer was then studied, with the objective of improving the bonding of the Pt anode and YSZ without compromising the activity of Pt, thereby improving the Pt anode stability in the H<sub>2</sub>S-air fuel cell. An ideal interposed bonding layer should be very thin and have good ionic and electronic conductivity as well as superior stability in pure H<sub>2</sub>S atmosphere. Titanium dioxide was selected, as it is a good catalyst for dissociation and oxidation of H<sub>2</sub>S in the Claus process [13,14]. TiO<sub>2</sub> is stable in the presence of H<sub>2</sub>S at temperatures as high as 950°C, and it has a very high electronic conductivity in reducing atmospheres [15-17]. Hydrogen spillover [18,19] at the interface of Pt/TiO<sub>2</sub> enhances dissociation of H<sub>2</sub>S and electronic conductivity. It has been suggested that titania is a potentially useful candidate as an anode cermet component for SOFCs [15].

A thin layer of TiO<sub>2</sub> was applied to the anode side of the YSZ wafer using the sol-gel technique. Figure 5-6 shows the scanning electron microscopy (SEM) image of a cross-section of the TiO<sub>2</sub>/YSZ interface. The wafer was embedded in epoxy for handling during the measurement. Due to different thermal expansion coefficients of YSZ and TiO<sub>2</sub> and volume reduction after heat-treatment, a large number of cracks formed in the TiO<sub>2</sub> layer, as expected. The thickness of the TiO<sub>2</sub> islands so formed was in the submicron range, *ca.* 0.2~0.5 μm. Platinum paste was then screen-printed onto the same side of the YSZ electrolyte as the TiO<sub>2</sub> layer. The resulting platinum anode occupied the spaces between TiO<sub>2</sub> islands, and was thereby anchored to the YSZ by the TiO<sub>2</sub>. Although the heat treatment temperature of the titanium dioxide layer was below 1000°C,

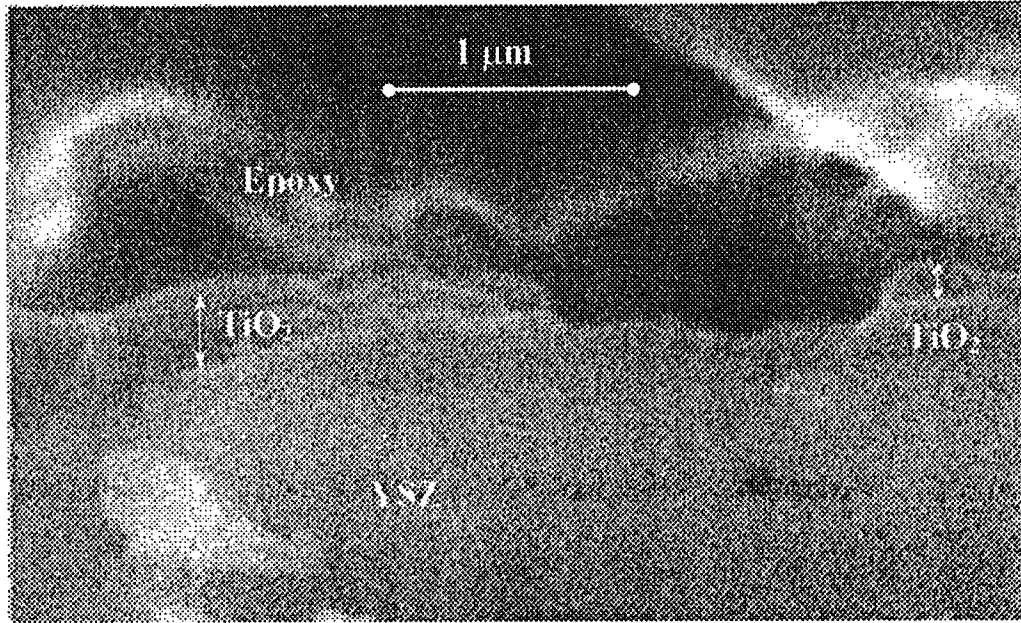
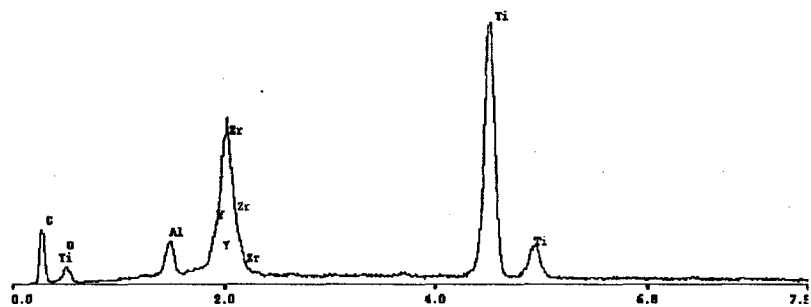


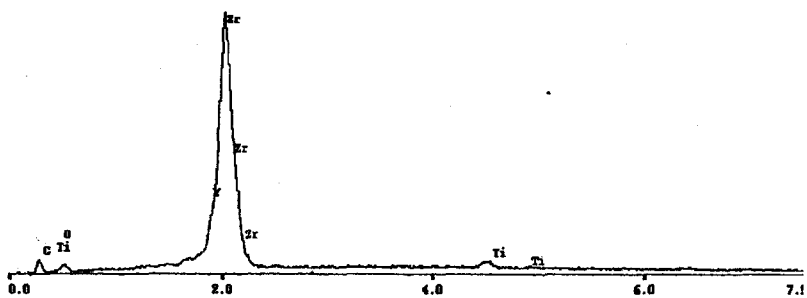
**Figure 5-6** Cross-section SEM image of TiO<sub>2</sub>/YSZ interface (sealed in epoxy)

it was found that  $\text{Ti}^{4+}$  ions had diffused into the surface layer of the YSZ structure after lengthy operation (two weeks) at high temperatures. Figure 5-7 shows the EDX analysis for titanium at different depths below the anode surface of the YSZ wafer. At locations 1  $\mu\text{m}$  beneath the  $\text{TiO}_2/\text{YSZ}$  interface, 1.30 wt% titanium was detected. At 3  $\mu\text{m}$  away from the interface, the content of Ti ions was below the resolution limit (ca. 0.1%) of the EDX instrumentation.

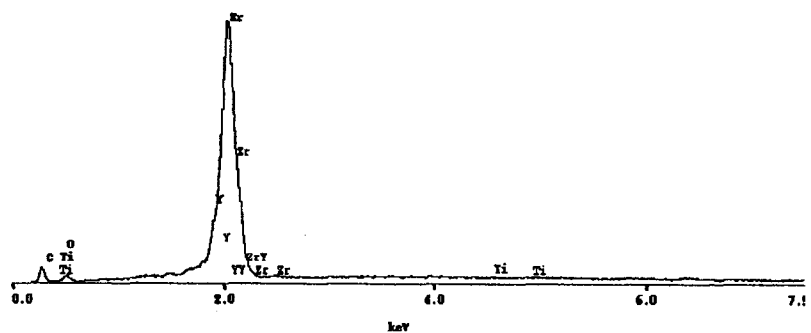
The OCV of the fuel cell having the arrangement: pure  $\text{H}_2\text{S}$ , Pt/ $\text{TiO}_2/\text{YSZ}/\text{Pt}$ , air, showed an unexpected dependence of performance on the flow rates of the anode and cathode streams. After the system had become stable, the OCV changed promptly with the change of flow rate ratio of air to  $\text{H}_2\text{S}$ . Figures 5-8 and 5-9 display the changes of OCV and current-voltage relationships vs. air flow rate for a constant flow rate of  $\text{H}_2\text{S}$ . The higher the air flow rate, the higher the OCV value and the better the voltage-current performance. When the flow rate of air was kept constant and the hydrogen sulfide flow rate was changed, a higher  $\text{H}_2\text{S}$  flow rate gave a lower OCV value. Thus, the OCV increased with increasing the relative flow rate of air and decreased with increasing the relative flow rate of  $\text{H}_2\text{S}$ . A reproducible OCV of 0.83 V was achieved when the flow rate ratio of air to  $\text{H}_2\text{S}$  was 10:1. When the fuel gas was changed from  $\text{H}_2\text{S}$  to  $\text{H}_2$ , a similar relationship was observed, but with a lower OCV value compared to pure  $\text{H}_2\text{S}$  fuel at the same air-to-fuel flow rate ratio. This phenomenon can be attributed to the crossover of fuel gas through the YSZ electrolyte. When the  $\text{H}_2\text{S}$  flow rate was high, the amount of  $\text{H}_2\text{S}$  passing through the electrolyte would increase, and so the water pressure, and perhaps  $\text{SO}_2$ , at the cathode side would also increase due to reaction of  $\text{H}_2\text{S}$  with air in the cathode compartment, leading to a decrease of OCV. On the other hand, the OCV



a



b



c

**Figure 5-7** EDX measurement on the cross-section of YSZ wafer after fuel cell test in pure H<sub>2</sub>S stream, as a function of distance from the TiO<sub>2</sub>/YSZ interface:  
 (a)  $d = 0 \mu\text{m}$ ; (b)  $d = 1 \mu\text{m}$ ; (c)  $d = 3 \mu\text{m}$

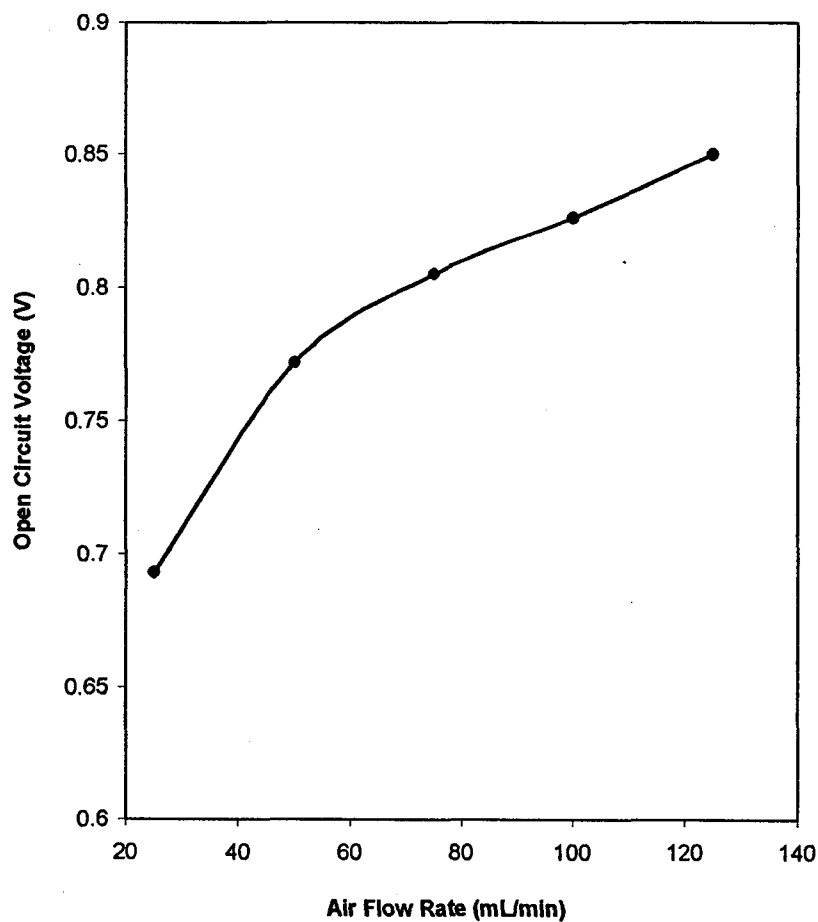


**Figure 5-8** Open circuit voltage of H<sub>2</sub>S-air fuel cell with TiO<sub>2</sub> interlayer as a function of air flow rate at 800°C.  
H<sub>2</sub>S (pure) flow rate: 15 mL/min

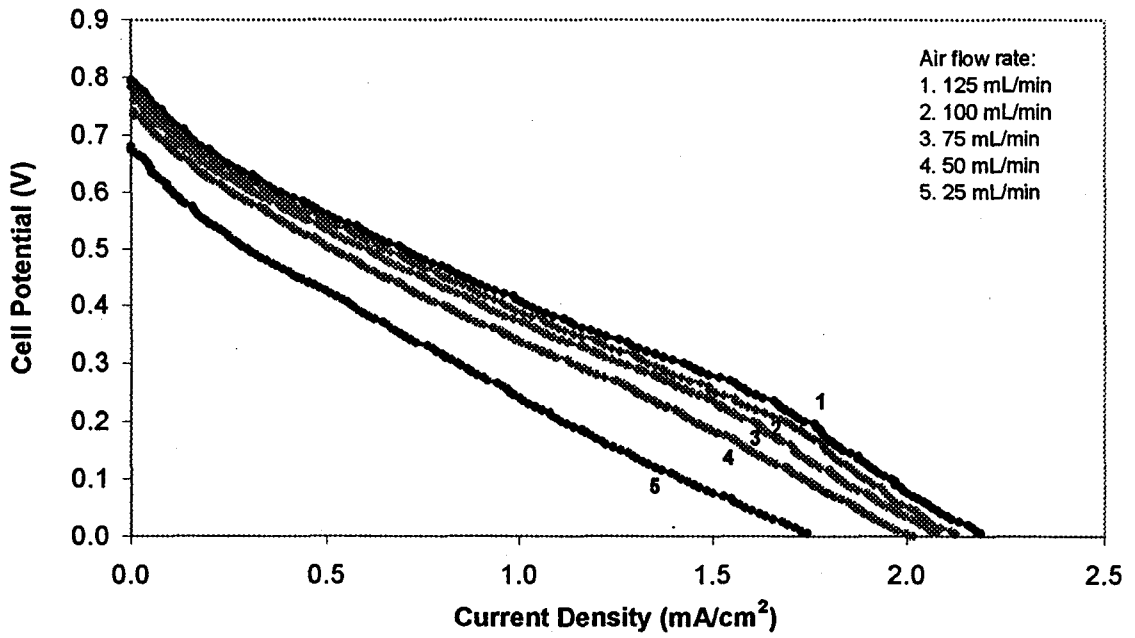


**Figure 5-9** Cell Performance at 800°C as a function of air flow rate for the fuel cell arrangement: pure H<sub>2</sub>S, Pt/TiO<sub>2</sub>/YSZ/Pt, air. H<sub>2</sub>S flow rate: 15 mL/min

would increase when the air flow rate was increased because the high air flow rate would remove H<sub>2</sub>O quickly. When the reactant gas was switched to H<sub>2</sub>, the crossover rate was higher for H<sub>2</sub> than for H<sub>2</sub>S gas, resulting in a higher water vapor pressure at the cathode, and consequently a lower OCV value.

Performance as a function of temperature for the H<sub>2</sub>S-air fuel cell having an intermediate TiO<sub>2</sub> layer (by sol-gel method) is shown in Figure 5-10. Cell performance improved with increasing operating temperature. The maximum current density of this cell was lower when compared to the cell without the TiO<sub>2</sub> interlayer. This decrease may be partially attributed to the lack of three-phase reaction zone. The spin-coated thin TiO<sub>2</sub> layer was very dense and the TiO<sub>2</sub> islands covered most of the YSZ surface. Moreover, TiO<sub>2</sub> is not a good oxide ion conductor. Therefore, the reaction sites for the electrochemical oxidation of H<sub>2</sub>S were limited.

The electronic conductivity of TiO<sub>2</sub> is very sensitive to reducing conditions, such as an atmosphere of hydrogen, carbon monoxide, hydrogen sulfide [16,17], and oxygen partial pressure [18]. The Pt/TiO<sub>2</sub> interface was expected to further enhance the sensitivity of TiO<sub>2</sub> conductivity to reducing conditions due to hydrogen spillover. Spillover is characterized by the local separation of the sites of activation and reaction. Hydrogen sulfide is activated by Pt to form Pt-H species (Eq. 5-1), which then react with oxide ions (Eq. 5-2) [19,20].



Since the electrical conductivity of Pt/TiO<sub>2</sub>/YSZ at the anode side was very sensitive to a

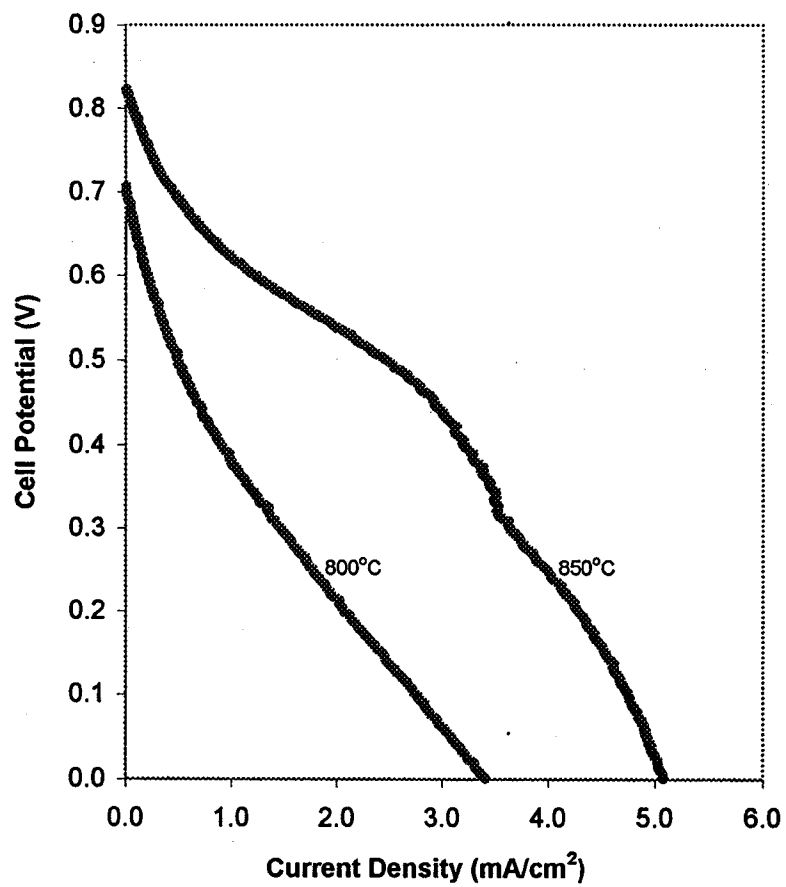


**Figure 5-10** Current as a function of voltage for the fuel cell:  
pure H<sub>2</sub>S, Pt/TiO<sub>2</sub> (sol-gel)/YSZ/Pt, air.  
Flow rates: H<sub>2</sub>S, 25 mL/min; air, 75 mL/min.

reducing atmosphere [19, 21-23], injection of electrons into the TiO<sub>2</sub>/YSZ structure from the spatial polaron layer of TiO<sub>2</sub> would have increased the electronic conductivity of TiO<sub>2</sub>/YSZ.

To improve cell performance, an alternative method of applying TiO<sub>2</sub> was examined. The intermediate TiO<sub>2</sub> layer was applied by painting TiO<sub>2</sub> paste onto the YSZ surface and then was heat-treated at 900°C for 2 h. The Pt electrode was screen-printed onto the resulting porous TiO<sub>2</sub> layer. Consequently, the extent of the TiO<sub>2</sub>/YSZ interface was decreased. The voltage-current performance using this more porous TiO<sub>2</sub> layer was improved significantly when compared with the performance using the spin-coated TiO<sub>2</sub> layer, as shown in Figure 5-11. The improvement was attributed to the significant increase of hydrogen spillover on Pt/TiO<sub>2</sub> during the reaction processes.

The addition of the intermediate TiO<sub>2</sub> layer increased the stability of the H<sub>2</sub>S-air fuel cell. Figure 5-12 gives the plots of OCV and current density at a potential of 0.4 V as the function of time on stream at 750°C. The OCV of the H<sub>2</sub>S-air fuel cell initially decreased over the first day of operation and then remained stable during subsequent operation for periods greater than 1 week. The cell was run at 0.4 V for 5 h during each measurement, with shutdown of applied potential between tests. The output current at a potential of 0.4 V dropped sharply during the first day and then decreased slightly with time on stream for remaining days. So far, the possible reason for the decline of the OCV and the current density at the beginning of the operation cannot be determined. The Pt/TiO<sub>2</sub> interface was stable during operation, which enhanced the stability of the system by anchoring the Pt anode onto the YSZ electrolyte, thereby preventing detachment.

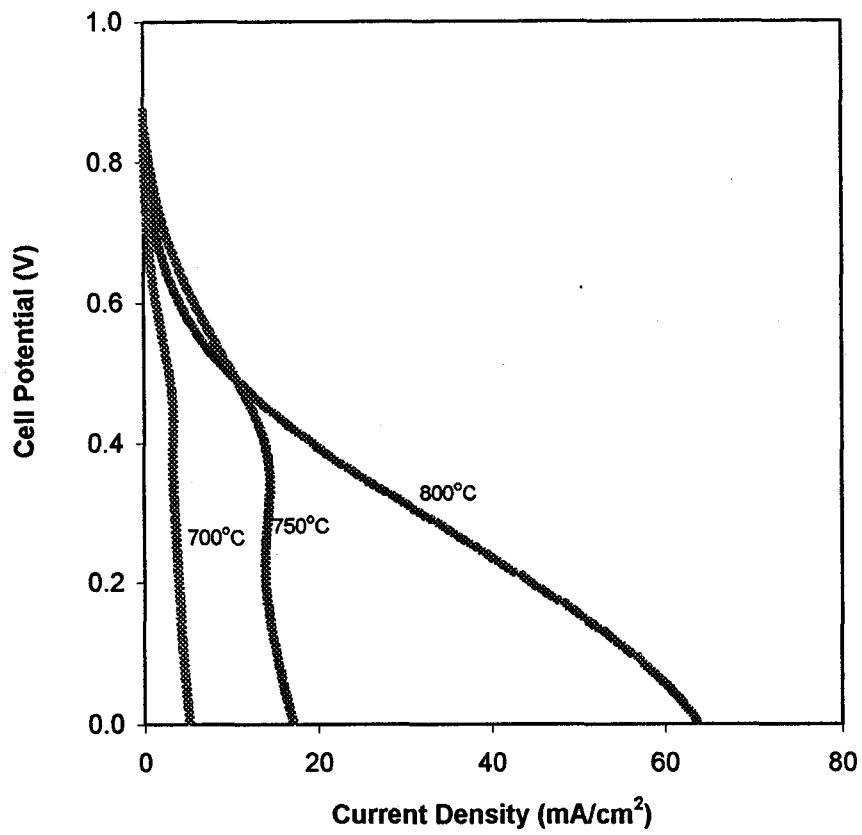


**Figure 5-11** Current as a function of voltage for the fuel cell:  
pure H<sub>2</sub>S, Pt/TiO<sub>2</sub> (paste painting)/YSZ/Pt, air.  
Flow rates: H<sub>2</sub>S, 25 mL/min; air, 75 mL/min.

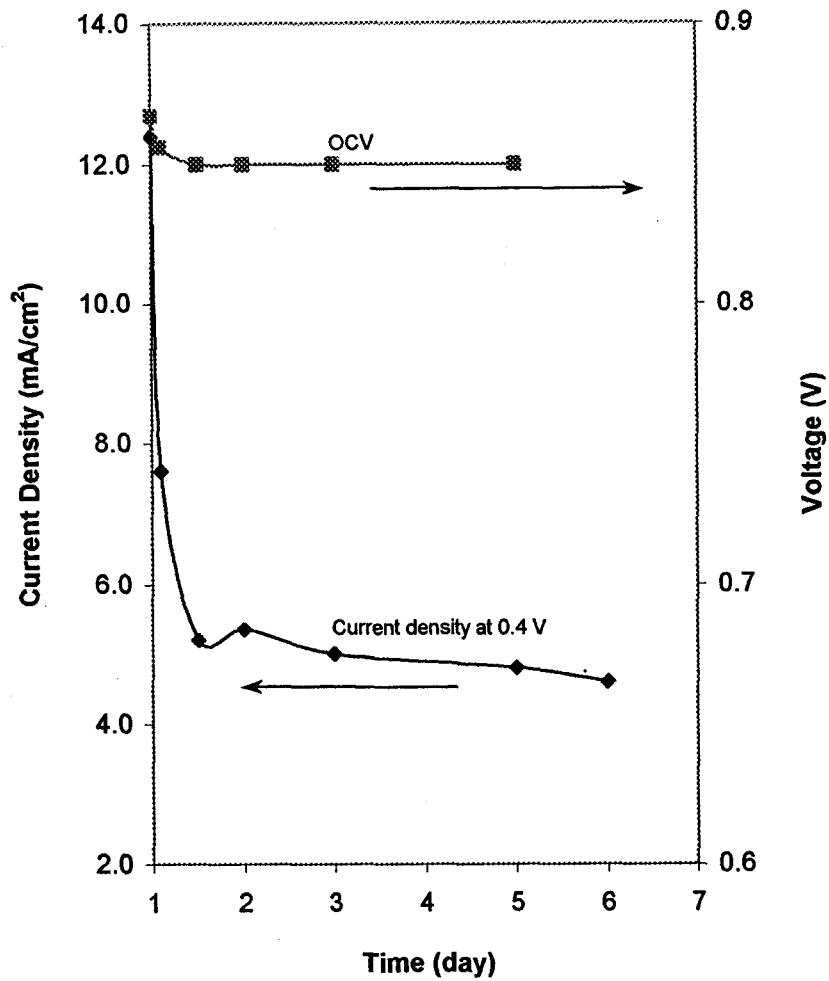


**Figure 5-12** Stability of H<sub>2</sub>S-air fuel cell with TiO<sub>2</sub> interlayer at 750°C.  
 Flow rates: H<sub>2</sub>S, 15 mL/min; air, 75 mL/min

The good physical and electrical stability of the Pt anode achieved by using TiO<sub>2</sub>-modified wafers is a promising result for high temperature H<sub>2</sub>S-air fuel cells. Hydrogen sulfide is an extremely corrosive gas, which is poisonous to the catalysts commonly used for hydrogen fuel cells and has the potential to disrupt catalyst structures. These effects result in short lifetime of most solid oxide fuel cells using H<sub>2</sub>S or H<sub>2</sub>S-contaminated feeds as fuel. The improvement in stability of cell performance described above is attributable to stabilization of active reaction sites and securing of the Pt anode catalyst to the YSZ wafer by the TiO<sub>2</sub> layer.

#### **5.4 Conclusions**

Platinum anodes deposited on YSZ having an intermediate layer of TiO<sub>2</sub> are more stable than Pt anodes in direct contact with YSZ for operation in a H<sub>2</sub>S-air fuel cell. When Pt is directly bonded to YSZ, cell performance decreased with a prolonged period of exposure time in pure H<sub>2</sub>S stream due to the contamination of Pt electrode by H<sub>2</sub>S gas. The contaminated Pt anode can be partly cleaned by polarizing the electrode in H<sub>2</sub> atmosphere or baking the wafer in N<sub>2</sub> atmosphere at high temperatures. A submicron layer of TiO<sub>2</sub> added to the anode surface of YSZ before depositing Pt anode stabilizes the Pt/YSZ interface. Stability of cell performance using platinum anode catalyst has thereby been significantly improved by applying the intermediate TiO<sub>2</sub> layer, which helps anchor the Pt anode and increases its activity. The TiO<sub>2</sub> layer prepared by paste painting renders better cell performance than the layer made by sol-gel technique, due to its highly porous structure.

## References

- [1] N. U. Pujare, K. W. Semkow and A. F. Sammells, *Journal of the Electrochemical Society*, **134**, 2639 (1987).
- [2] N. U. Pujare, K. J. Tsai and A. F. Sammells, *Journal of the Electrochemical Society*, **136**, 3662 (1989).
- [3] I. V. Yentekakis and C. G. Vayenas, *Journal of the Electrochemical Society*, **136**, 996 (1989).
- [4] T. J. Kirk and J. Winnick, *Journal of the Electrochemical Society*, **140**, 3494 (1993).
- [5] D. Peterson and J. Winnick, *Journal of the Electrochemical Society*, **145**, 1449 (1998).
- [6] D. Peterson and J. Winnick, *Journal of the Electrochemical Society*, **143**, L55 (1996).
- [7] C. Yates and J. Winnick, *Journal of the Electrochemical Society*, **146**, 2841 (1999).
- [8] M. Liu, P. He, J. L. Luo, A. R. Sanger and K. T. Chuang, *J. Power Sources*, **94**, 20 (2001).
- [9] T. W. Kueper, S. J. Visco and L. C. De Jonghe, *Solid State Ionics*, **52**, 251 (1992).
- [10] K. Kobayashi, K. Kato, K. Terabe, S. Yamaguchi and Y. Iguchi, *Journal of the Ceramic Society of Japan*, **106**, 860 (1998).
- [11] J. O'M. Bockris and S. Srinivasan., '*Fuel Cells: Their Electrochemistry*', Chapter 4, McGraw-Hill, New York (1969).
- [12] J. G. McCarty, K. M. Sancier and H. Wise, *Journal of Catalysis*, **82**, 92 (1983).

- [13] J. Zaman and A. Chakma, *Fuel Processing Technology*, **41**, 159 (1995).
- [14] A. Piepu, O. Saur, J.C. Lavalley, O. Legendre and C. Nedez, *Catalysis Reviews: Science and Engineering*, **40**(4), 409(1998).
- [15] M. T. Colomer, J. R. Jurado, R. M. C. Marques and F. M. B. Marques, *Proceedings of the 3<sup>rd</sup> International Symposium on Solid Oxide Fuel cells*, S. C. Singhal and H. Iwahara, Editors, PV 93-4, p. 523, Pennington, NJ (1993).
- [16] R. M. C. Marques, J. R. Frade and F. M. B. Marques, *Proceedings of the 3<sup>rd</sup> International Symposium on Solid Oxide Fuel cells*, S. C. Singhal and H. Iwahara, Editors, PV 93-4, p. 513, Pennington, NJ (1993).
- [17] T. Norby, *Solid State Ionics*, **40/41**, 857 (1990).
- [18] J. B. Bates, J. C. Wang and R. A. Perkins, *Physical Review B*, **19**, 4130 (1979).
- [19] U. Balachandran and N. G. Eror, *Journal of Materials Science*, **23**, 2676 (1988).
- [20] U. Roland, R. Salzer, T. Braunschweig, F. Roessner, and H. Winkler, *Journal of the Chemical Society, Faraday Transactions*, **91**, 1091 (1995).
- [21] N. M. Rodriguez and R. T. K. Baker, *Journal of Catalysis*, **140**, 287 (1993).
- [22] K. L. Scholl and E. A. Fletcher, *Energy*, **18**, 69 (1993).
- [23] J. H. Park and R. N. Blumenthal, *Journal of the Electrochemical Society*, **136**, 2867 (1989).

## CHAPTER 6

# PERFORMANCE CHARACTERISTICS OF H<sub>2</sub>S-POWERED SOLID OXIDE FUEL CELLS USING METAL SULFIDE ANODE CATALYSTS

### 6.1 Introduction

It has been recognized that hydrogen sulfide has potential value as a suitable fuel for operations in solid oxide fuel cells. However, the development of H<sub>2</sub>S-air fuel cells has received much less attention than H<sub>2</sub>-air fuel cells, in part because hydrogen sulfide is a powerful poison to most currently developed fuel electrodes for SOFCs [1]. The effects of sulfur-containing impurities in fuel gases, primarily hydrogen sulfide, on anode materials have become a challenging problem to the commercialization of SOFC systems [2]. It is much more difficult to select anode catalysts for the electrochemical conversion of H<sub>2</sub>S because the materials that can endure pure H<sub>2</sub>S at high operating temperatures of SOFCs are very limited. The selection of anode catalysts is crucial to cell performance when utilizing H<sub>2</sub>S as fuel.

Efforts have been directed to the development of suitable anode materials for H<sub>2</sub>S-powered SOFCs. The ability of platinum to electrochemically catalyze the oxidation of H<sub>2</sub>S at temperatures above 650°C has been acknowledged [3-7], but Pt degrades over time in H<sub>2</sub>S streams [7,8]. Pujare *et al.* investigated several thiospinels and tungsten sulfide as anode catalysts. Their relative activities, based on empirical kinetics, were found to be in the order: NiFe<sub>2</sub>S<sub>4</sub> > WS<sub>2</sub> > CuCo<sub>2</sub>S<sub>4</sub> > CuFe<sub>2</sub>S<sub>4</sub> ≈ NiCo<sub>2</sub>S<sub>4</sub> > CuNi<sub>2</sub>S<sub>4</sub> [9].

New active anode material consisting of  $\text{Li}_2\text{S}/\text{CoS}_{1.035}$  exhibited better activity for the conversion of  $\text{H}_2\text{S}$ , but the performance still decreased over time [10]. In order to be a suitable candidate for the electrochemical oxidation of  $\text{H}_2\text{S}$ , an anode material must possess good electrical conductivity and sulfur-tolerance at high temperatures in addition to good catalytic activity. It is known that most metals and metal oxides are severely corroded by  $\text{H}_2\text{S}$  at elevated temperatures. Therefore, it is intuitive to consider metal sulfides as alternative potentially useful catalysts.

Metal sulfides are inexpensive when compared with precious metals like Pt. Among them,  $\text{MoS}_2$ , a hexagonal layered n-type semiconductor, is a widely used component in catalysts for a variety of hydrogenation/dehydrogenation and hydrodesulfurization processes in the petroleum industry. Bimetallic sulfides of molybdenum with cobalt, iron and nickel are each active catalysts for hydrodesulfurization processes [11-13]. The activity is attributed in part to the presence of  $\text{MoS}_2$ -like aggregates. An important attribute of these catalysts is sulfur tolerance.  $\text{MoS}_2$  also has been shown to be an effective catalyst for reversible decomposition of  $\text{H}_2\text{S}$  above  $600^\circ\text{C}$  [14], which indicates that  $\text{MoS}_2$  is chemically stable in high temperature  $\text{H}_2\text{S}$  streams and is not poisoned. However,  $\text{MoS}_2$  sublimates at temperatures over  $450^\circ\text{C}$  at atmospheric pressure. The electrical conductivity of  $\text{MoS}_2$  increases as the temperature approaches  $400^\circ\text{C}$  [15]. Molybdenum disulfide supported on a conductive substrate is known to be an active anode catalyst for  $\text{H}_2\text{S}$ -air fuel cells operating at atmospheric pressure and  $20\text{-}90^\circ\text{C}$  [16], and at  $120\text{-}145^\circ\text{C}$  and  $235\text{-}510\text{ kPa}$  [17].

The objective of the present work is to examine the effectiveness of  $\text{MoS}_2$  and several composite metal sulfides as anode catalysts in  $\text{H}_2\text{S}$ -air SOFCs, by studying the

electrochemical behavior of the cell. It will be shown that these metal sulfide anode catalysts exhibit a combination of good electronic conductivity and better catalytic activity than Pt. It will also be shown that composite anode catalysts M-Mo-S (M = Fe, Co, Ni), prepared from mixed metal sulfides MS-MoS<sub>2</sub>, had superior stability and activity up to 850°C and were not volatile, in contrast to MoS<sub>2</sub> alone. However, the detachment of Pt current collecting layer coated on the surface of the anode largely increased cell resistance and thereby adversely affected cell performance. In order to overcome the poor electrical contact between the Pt current collecting layer and the anode layer, Ag powder was mechanically admixed into the anode material as current collector instead of applying a platinum layer. It will be shown that addition of Ag powder into the anode material Co-Mo-S improved cell performance and that the composite anode was stable over an extended period of time.

## **6.2 Experimental**

### **6.2.1 Preparation of Anode Catalysts**

Two different methods have been used to prepare the anode catalysts. In one method, cobalt molybdenum oxide (CoMoO<sub>4</sub>) was used as the starting material for the anodes. Upon exposure to pure H<sub>2</sub>S atmosphere, the oxide material was sulfided and then acted as the effective anode catalyst for fuel cell operation. Alternatively, commercially available metal sulfide powders were mixed and heat-treated for preparation of anode catalysts. The sources of these metal sulfides were: MoS<sub>2</sub> (Aldrich, 99.9%), CoS (Alfa Aesar, 99.9%), FeS (Alfa Aesar, 99.9%) and NiS (Alfa Aesar, 99.9%). Two-component metal sulfides to be tested were made by initially mixing MoS<sub>2</sub> with one of the metal

sulfides FeS, CoS or NiS in 1:1 molar ratio. To ensure uniform mixing, ethanol was added to the combination to make a suspension that was mixed thoroughly for several hours. Then ethanol was allowed to evaporate slowly, to leave the binary metal sulfides as powders. The binary metal sulfides were heat-treated in N<sub>2</sub> atmosphere at 1050°C for two hours and allowed to cool under N<sub>2</sub> to room temperature. The resulting powders were then used to prepare the anode catalysts.

### **6.2.2 Measurement of Electrical Resistivity of Anode Catalysts**

The electrical resistivity of each anode catalyst was measured as membranes having the structure Pt/anode catalyst/Pt under a flow of N<sub>2</sub> at temperatures between 25°C and 850°C.

A wafer of each catalyst was made by pressing the catalyst powder in a die at room temperature and a pressure of 47000 psi. Each catalyst disk so made was about 1 mm thick and 2.54 cm in diameter. Pt paste was painted onto both faces of the wafer, then each face was connected to a Pt lead. The catalyst disk was sealed between two ceramic tubes using ceramic sealant. Both faces were exposed to N<sub>2</sub> streams. The total resistance of the electrochemical apparatus, including that of the connecting wire, was determined using a Keithley 199 digital multimeter.

### **6.2.3 Cell Preparation and Construction**

The electrolyte wafers consisted of 8 mol% yttria stabilized zirconia (YSZ) with a thickness of 0.2 mm and a diameter of 2.54 cm. It is known that increases in roughness at the interface between the electrolyte and the electrode contribute to improved electrode performance [18]. Therefore, the surfaces of the electrolytes were pretreated and

mechanically roughened using silicon carbide power to increase the three-phase boundary area. Platinum paste (Heraeus CL11-5100) was screen printed onto one side of the electrolyte substrates as cathode. After drying, the platinum film was fired in air at 1050°C for half an hour. When CoMoO<sub>4</sub> was used as the anode material, it was mixed with isopropanol and glycerine to make a paste. Other anode catalysts were applied as viscous pastes formed by mixing the metal sulfide powder (MoS<sub>2</sub> or M-Mo-S) with  $\alpha$ -terpineol.

A thin layer of the anode paste (ca. 0.15 mm) was applied onto the anode side of the YSZ membrane using screen printing technique. Then, the assembly was heated to 1050°C and held at that temperature for 30 min. The sintering of the metal sulfides was necessarily performed in an oxygen-free atmosphere to avoid formation of volatile MoO<sub>3</sub> [12]. The assembly was cooled under N<sub>2</sub>. Then, for anode catalysts containing no Ag powder, platinum paste was also painted on top of the sintered metal sulfides and dried. The porous Pt layer so formed was intended to serve as current collector and improve electrical contact between the anode and the electrical lead.

When the anode catalyst was MoS<sub>2</sub> or M-Mo-S admixed with Ag, Ag powder (up to 10% by weight) was thoroughly mixed with the metal sulfide powder, and the mixture was mixed with  $\alpha$ -terpineol to make the paste. The paste was applied onto the anode face of the YSZ membrane and sintered following the same procedure as stated above. No Pt paste was applied to the anode of these cells. SEM (scanning electron microscopy) and EDX (energy dispersive X-ray spectrometry) data were obtained with a Hitachi S-2700 Scanning Electron Microscope and PGT Imix system. Results for a typical anode catalyst with Ag after the heat treatment are shown in Figure 6-1. The anode was porous, having

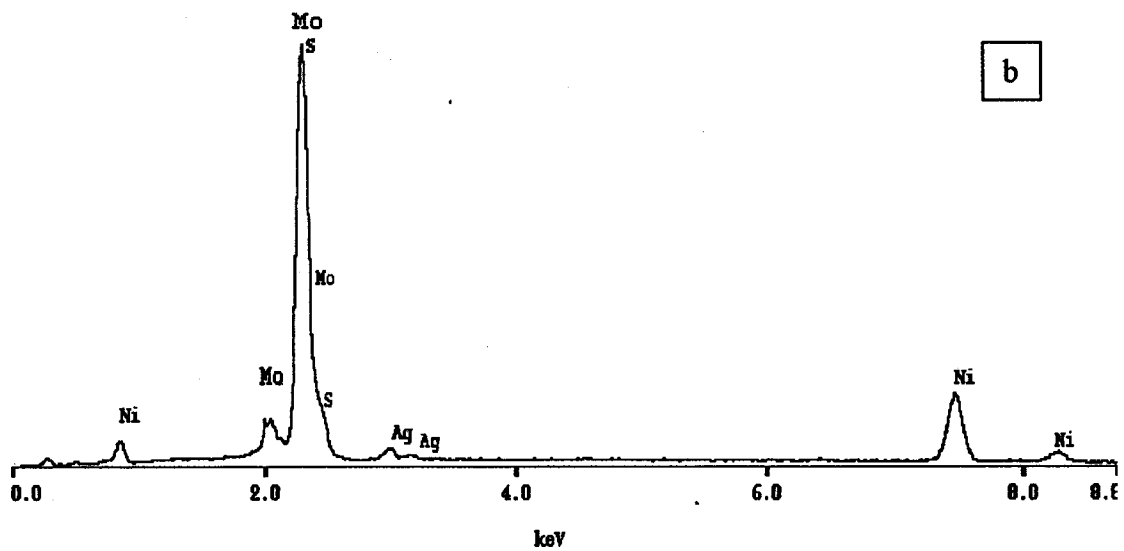
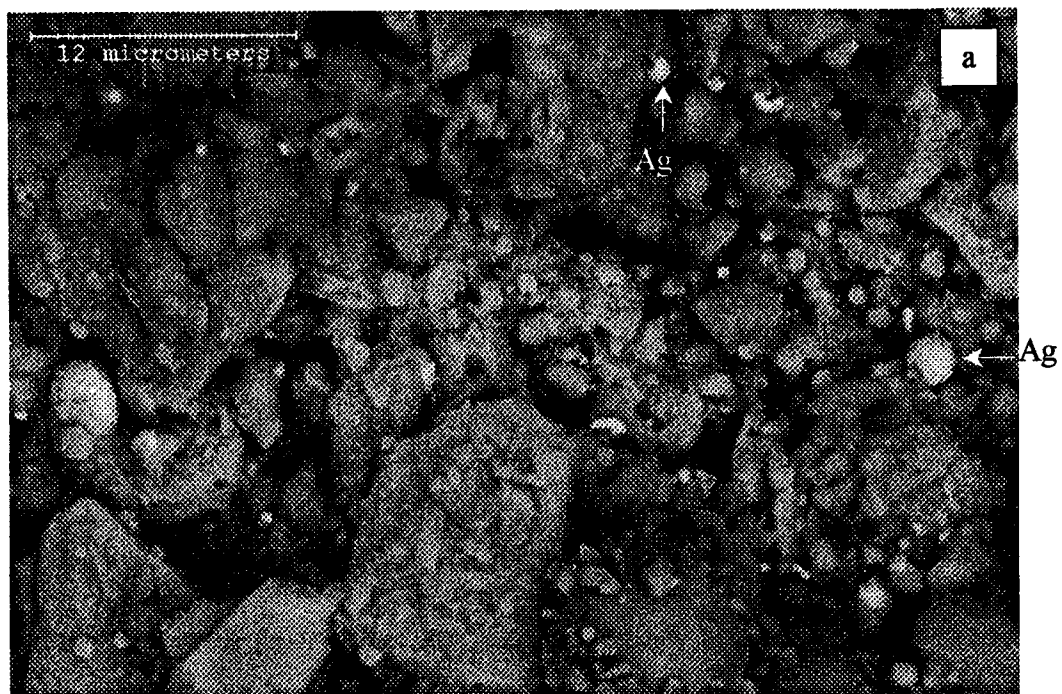


**Figure 6-1** (a) SEM image of anode catalyst after heat-treatment (back-scattering mode); (b) EDX spectrum of a typical catalyst particle in (a)

catalyst particle sizes between 0.05 and 10  $\mu\text{m}$ . An EDX result for a randomly chosen large particle ( $\sim 10 \mu\text{m}$  dia.) is shown in Figure 6-1b. Mo, Ni, Ag and S were all present throughout the particle, showing that the catalyst components were well mixed and well distributed. Ag coated some anode particle surfaces, shown as bright areas in Figure 6-1a.

The apparent electrode surface area was approximately  $1 \text{ cm}^2$ . A sheet of Pt mesh welded to a Pt lead wire was placed in intimate contact with the surface of each electrode. The cathode side of the electrode-electrolyte assembly was mounted onto a supporting annular alumina (98%) disk with ceramic sealant (Ceramabond 503, Aremco). This alumina disk was used to replace the glass holder in Figure 5-1 because alumina has a thermal expansion coefficient compatible with the YSZ electrolyte and the sealant. A 1.1 cm dia. opening in the center of the supporting ceramic disk allowed air to access the cathode. The supporting disk was then sealed between two alumina tubes arranged horizontally, using the same ceramic adhesive placed on both sides of the electrolyte to seal the gas compartments. The cell was heated in a tubular furnace (Thermolyne F79300). Air and nitrogen flowed through the cathode and anode chambers, respectively. The cell was slowly brought up to the operating temperature. Nitrogen was used as inert feed when the cell was not in operation. Pure  $\text{H}_2\text{S}$  was used as fuel gas and air was supplied as oxidant during all tests.

#### **6.2.4 Electrochemical Characterization**

Impedance measurements were carried out in the frequency range 0.5 Hz to 100 kHz using a Gamry EIS 300 system. Potentiodynamic current-potential measurements were performed using a Gamry electrochemical measurement system (PC4-750) at a scan

rate of 1 mV/s. For anode catalysts without the addition of Ag, current-potential curves were corrected for ohmic voltage losses in the system by subtracting ohmic drop (IR) from the measured potential, where the current (I) was negative and the ohmic resistance (R) was calculated from the impedance spectra. For anode catalysts admixed with Ag, the current-voltage performances were recorded potentiodynamically in both non-IR and IR compensation mode with the Gamry system.

### **6.2.5 Volatility of Catalyst Materials**

The volatility of anode catalysts was determined by formation of a mirror comprising sublimed material downstream from the anode. When MoS<sub>2</sub> alone was used as anode catalyst, a MoS<sub>2</sub> mirror formed on the cell walls downstream from the anode. In contrast, when composite sulfides M-Mo-S were used, no mirror was formed. Similarly, when M-Mo-S admixed with Ag was used as the anode catalyst, no mirror was formed.

## **6.3 Results and Discussion**

### **6.3.1 Resistivity of MoS<sub>2</sub> and M-Mo-S (M = Fe, Co, Ni)**

The electrical resistivities of anode catalyst samples with the structure Pt/anode catalyst/Pt are listed in Table 6-1. The resistivity of MoS<sub>2</sub> wafer decreased rapidly as the temperature increased to 750°C, and was then approximately constant in the range 750-850°C. The data are consistent with decrease of the electronic resistance of MoS<sub>2</sub> with increasing temperature [15,19]. Above 750°C, the resistivity of MoS<sub>2</sub> wafer decreased to less than 10 Ω·cm.

**Table 6-1** Electrical resistivities of anode catalysts: MoS<sub>2</sub> or M-Mo-S (M = Fe, Co, Ni)

Anode Catalyst	Resistivity ( $\Omega\cdot\text{cm}$ )						
	25°C	100°C	300°C	500°C	750°C	800°C	850°C
MoS <sub>2</sub>	210.17	198.02	178.78	63.31	9.12	8.10	7.60
Fe-Mo-S	96.22	53.68	11.14	8.61	8.61	6.08	4.56
Co-Mo-S	11.14	9.62	11.65	4.56	3.04	4.05	7.60
Ni-Mo-S	73.43	64.32	45.58	0.51	0.51	1.52	1.01

As shown in Table 6-1, the electrical resistivities of the composite catalyst pellets Pt/M-Mo-S/Pt (M = Fe, Co, Ni) at the temperature range of 25-500°C were much lower than that of MoS<sub>2</sub>. At fuel cell operating temperatures 750-850°C, the resistivities of the composite anode catalysts were in the range 0.51-8.61 Ω·cm. Thus the present anode catalysts have good electrical conductivity for use as anode catalysts under high temperature operating conditions.

### 6.3.2 Electrochemical Characteristics of Metal Sulfide Anode Catalysts

#### 6.3.2.1 CoMoO<sub>4</sub>

The first anode catalyst examined was sulfided CoMoO<sub>4</sub>. Open-circuit potentials of 0.9 V were obtained for this cell. However, the maximum current density was low, 10.7 mA/cm<sup>2</sup> at 750°C and 12.6 mA/cm<sup>2</sup> at 800°C, as shown in Figure 6-2. The primary reason for this mediocre cell performance was the very high cell resistance. Impedance measurements revealed that the cell specific ohmic resistance under open circuit conditions was about 17 Ω·cm<sup>2</sup> and 22 Ω·cm<sup>2</sup> at 750°C and 800°C, respectively. Postmortem inspection found that the anode material was very loosely attached to the electrolyte surface, resulting in a bad contact with the YSZ electrolyte. This phenomenon can be attributed to the morphology change during sulfurization of the oxide to metal sulfide in H<sub>2</sub>S. Therefore, subsequent experiments were all performed with metal sulfides directly coated on the electrolyte surface as anode material in order to maintain good contact between the electrode and the electrolyte.

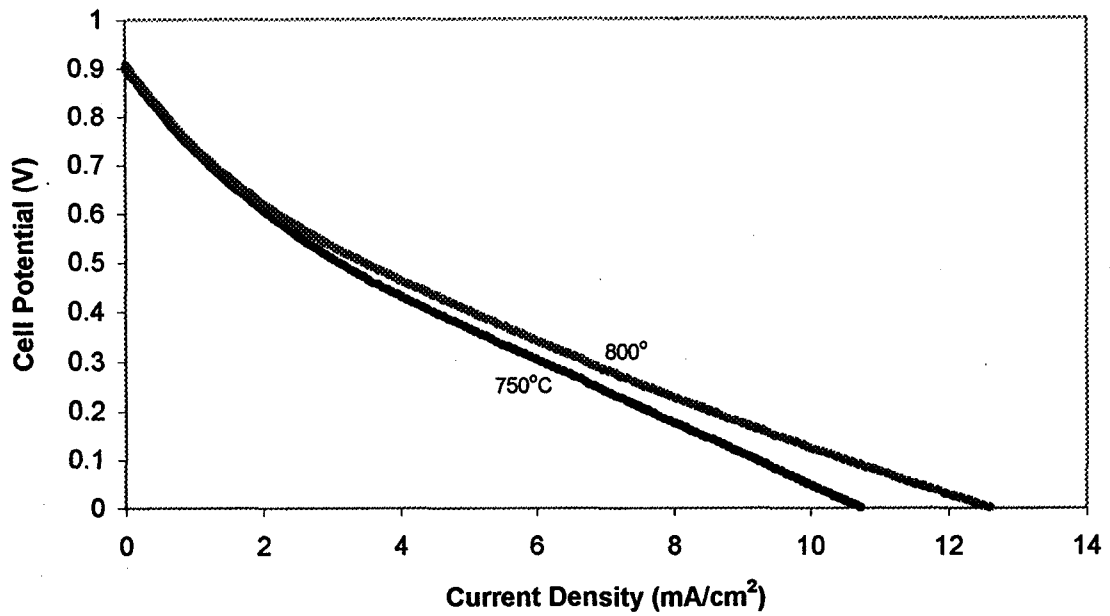


**Figure 6-2** Current-voltage curves for the fuel cell with  $\text{CoMoO}_4$  as anode material in pure  $\text{H}_2\text{S}$  atmosphere

### 6.3.2.2 $\text{MoS}_2$

Figures 6-3 and 6-4 compare the performances of  $\text{MoS}_2$  and Pt anode catalysts in  $\text{H}_2\text{S}$ -air SOFC at  $800^\circ\text{C}$ . The polarization characteristics with and without IR correction are shown in Figure 6-3. In the low current region, the  $\text{MoS}_2$  anode showed a higher current output when compared with that of the Pt anode at the same voltage, which indicated that  $\text{MoS}_2$  had a greater catalytic activity [20]. However, as these experiments were performed without a good reference electrode [21], it was not possible to fully elucidate anode effects. The maximum current density measured for Pt was  $101 \text{ mA/cm}^2$ , which was slightly higher than  $98.3 \text{ mA/cm}^2$  for  $\text{MoS}_2$ , because of the lower ohmic resistance of the cell using Pt as anode. The ohmic resistance determined from impedance measurements (Table 6-2) was  $2.77 \Omega\cdot\text{cm}^2$  for Pt and  $3.54 \Omega\cdot\text{cm}^2$  for  $\text{MoS}_2$ , from which the IR compensated I-V curves were derived. By comparing the actual I-V curves with those after IR correction, it was seen that the potential was reduced by as much as 384 mV for  $\text{MoS}_2$ . Thus it is necessary to reduce the internal ohmic resistance of the cell to improve the overall cell performance.

In contrast to the I-V relations, the maximum power densities obtained for  $\text{MoS}_2$  were higher than those for Pt, with and without IR correction (Figure 6-4). After IR compensation, power densities as high as  $40 \text{ mW/cm}^2$  were achieved for  $\text{MoS}_2$  at  $800^\circ\text{C}$ . Although the IR corrected curves did not exhibit the real cell performance, they showed the potential value of  $\text{MoS}_2$  as active anode catalysts. However,  $\text{MoS}_2$  is volatile above  $450^\circ\text{C}$ . Thus there was continuous loss of  $\text{MoS}_2$  in the anode stream, resulting in limited cell lifetime. Consequently, I then investigated M-Mo-S composite anode catalysts, as these materials are not volatile in the same temperature range.

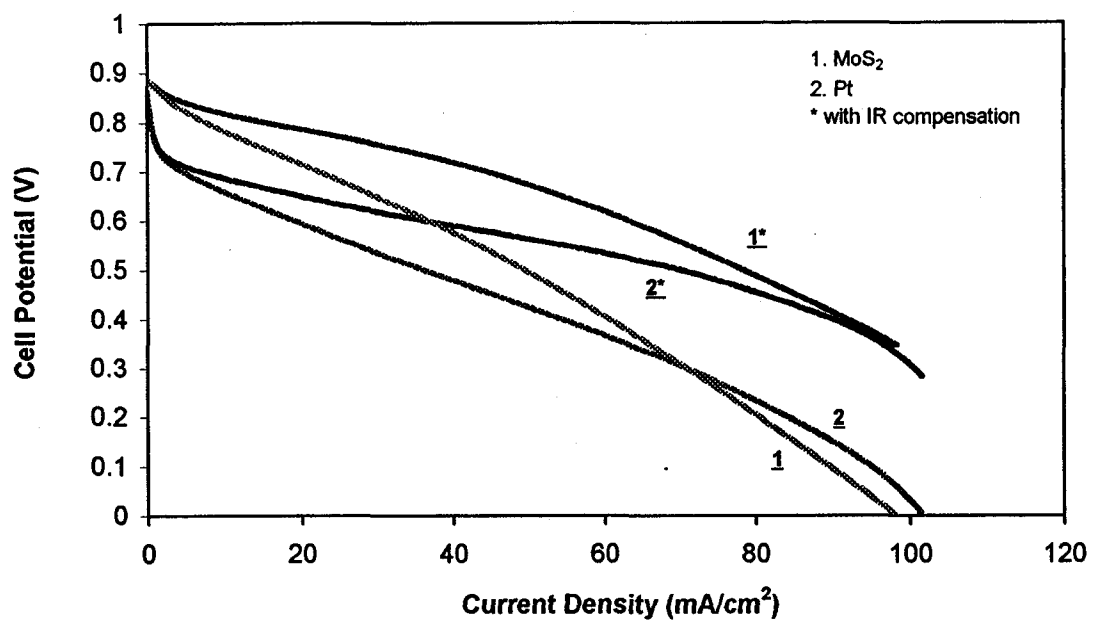


**Figure 6-3** Comparison of current-voltage curves using MoS<sub>2</sub> and Pt as anodes at 800°C with and without IR correction

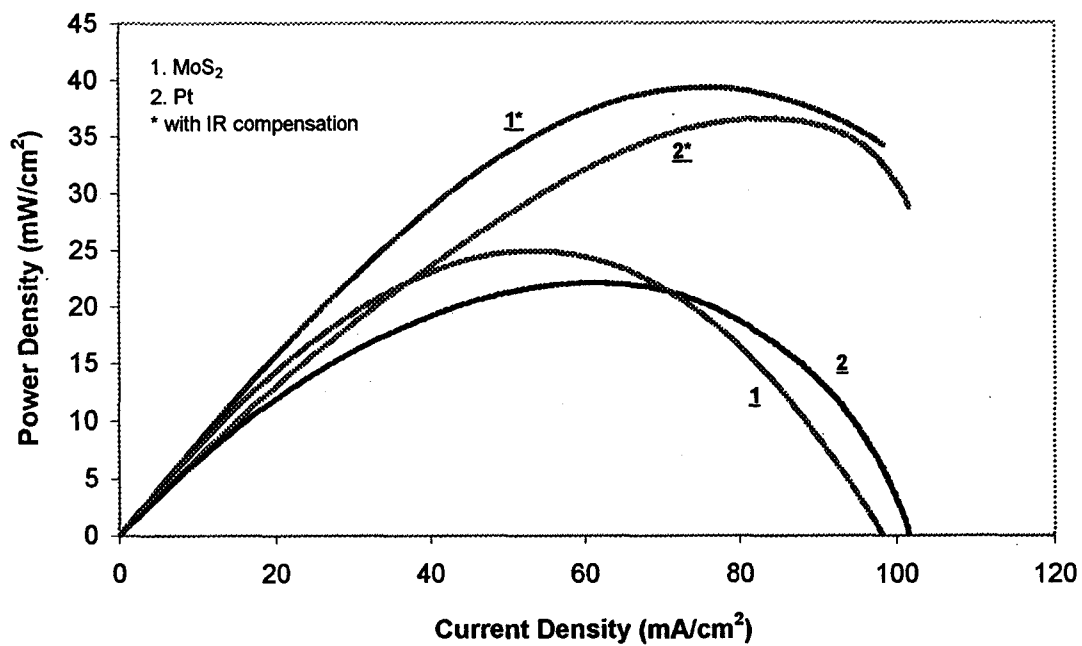


**Figure 6-4** Relationship of current density to power density for H<sub>2</sub>S-air fuel cells using MoS<sub>2</sub> and Pt as anodes at 800°C

**Table 6-2** Cell area specific ohmic resistance (R·A) using different anode materials at selected operating temperatures

<i>Temperature</i> (°C)	<i>R·A (Ω·cm<sup>2</sup>)</i>				
	Pt	MoS <sub>2</sub>	Co-Mo-S	Fe-Mo-S	Ni-Mo-S
800	2.77	3.54	3.10	3.65	
850			4.01	10.28	8.85

### 6.3.2.3 Fe-Mo-S

Figure 6-5 shows the current density vs. voltage behavior with Fe-Mo-S as the anode catalyst. In contrast to MoS<sub>2</sub> and the Co and Ni analogues, the maximum current density measured at 800°C was considerably higher than that at 850°C. The cause of this phenomenon was the large increase in the ohmic resistance of the cell from 3.65 Ω·cm<sup>2</sup> at 800°C to 10.3 Ω·cm<sup>2</sup> at 850°C (Table 6-2), which exceeded the decrease in electrolyte resistance at higher temperature. The large increase in cell area specific ohmic resistance was mainly ascribed to detachment and/or poisoning of Pt thin film in H<sub>2</sub>S gas, caused by electrochemical polarization at 800°C. In Chapter 5, I showed that PtS was easily formed on the surfaces of Pt electrodes in high temperature H<sub>2</sub>S streams, and that electrochemical oxidation of H<sub>2</sub>S on Pt/YSZ interface severely accelerated the reversible formation of PtS and led to rapid detachment of Pt anode from the YSZ [7,8]. Although herein Pt served primarily as current collector and not as catalyst, the large current flow had the same damaging effect. The failure of the contact between Pt current collector and the catalyst may also have been affected by another cause: weak bonding of the Pt film to the anode Fe-Mo-S. The adverse effect of polarization on cell resistance can also be seen in Figure 6-6, which shows how the cell resistance changed with polarization conditions at 800°C. The impedance spectra were measured in this order: (1) open circuit; (2) polarization at 0.5 V; and (3) polarization at 0.4 V. The cell area specific ohmic resistance increased from 3.65 Ω·cm<sup>2</sup> under open circuit conditions to 9.39 Ω·cm<sup>2</sup> at 0.5 V, then continued rising to 10.7 Ω·cm<sup>2</sup> at 0.4 V. However, when the temperature was increased to 850°C, the ohmic resistance dropped to 10.3 Ω·cm<sup>2</sup>, consistent with the decrease in the YSZ electrolyte resistance at higher temperature. This indicated that the increase in operating

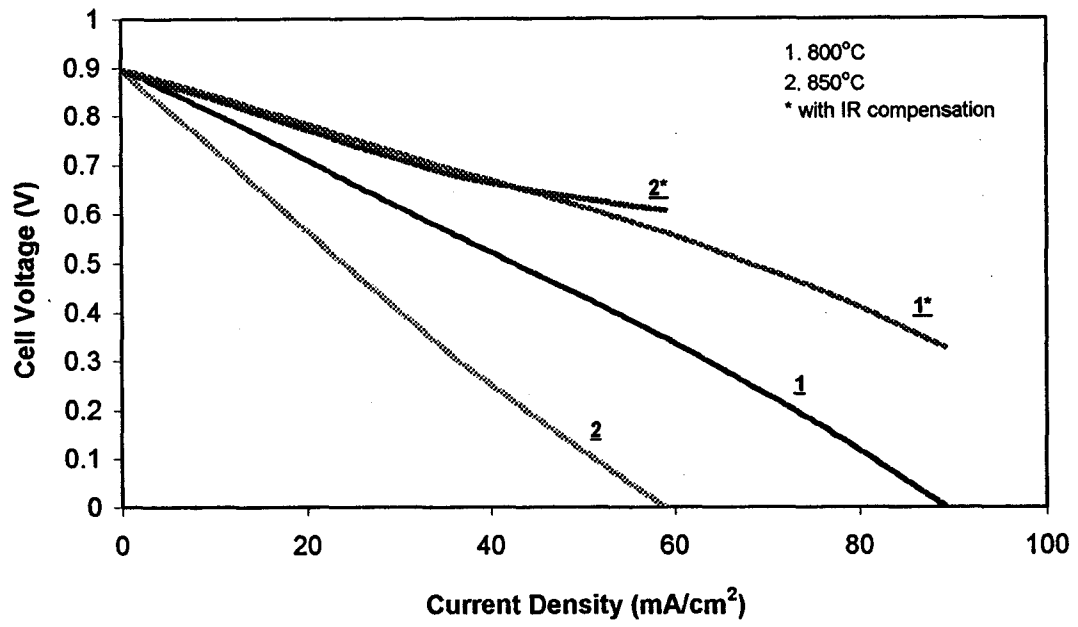


**Figure 6-5** Relationship between current density and voltage using Fe-Mo-S as anode

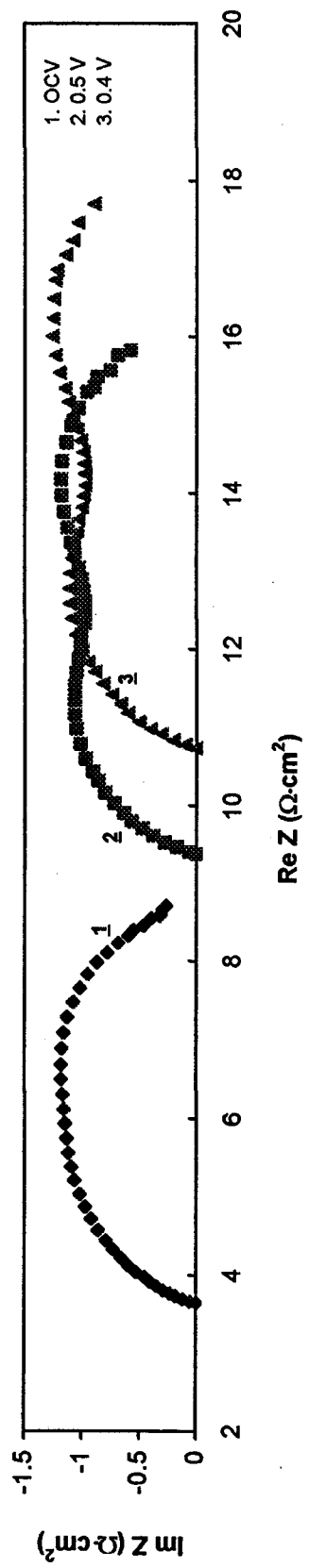


Figure 6-6 Impedance spectra for the cell using Fe-Mo-S as anode at 800°C

temperature did not further deteriorate the electrical contact between the Pt current collector and the anode.

Figure 6-7 shows current density as a function of power density for the use of Fe-Mo-S as anode catalyst. The IR-corrected power density obtained at 800°C increased to 34 mW/cm<sup>2</sup>. However, it was not possible to determine a maximum value for the IR compensated power density for this system due to the large internal resistance.

#### 6.3.2.4 Ni-Mo-S

Bimetallic Ni-Mo-S anode catalyst has been tested at 850°C only. Figure 6-8 shows the cell voltage and power density as a function of current density, with and without IR correction. The maximum current density was 67.6 mA/cm<sup>2</sup>. The ohmic resistance was 8.85 Ω·cm<sup>2</sup>, as determined by impedance spectroscopy (Table 6-2). Consequently, IR corrections as high as 600 mV potential were calculated at the maximum current density. The large resistance found for fresh samples indicated that the original electrical contact between screen-printed Pt layer and this anode material was poor, even before generation of any effects resulting from polarization. Thus, as found for Fe-Mo-S, the maximum IR corrected value for power density at 850°C could not be determined. Post-mortem inspection of the materials showed that the Pt film had become detached from the anode during testing. Thus Pt film alone cannot be used as current collector on Ni-Mo-S anode catalysts.

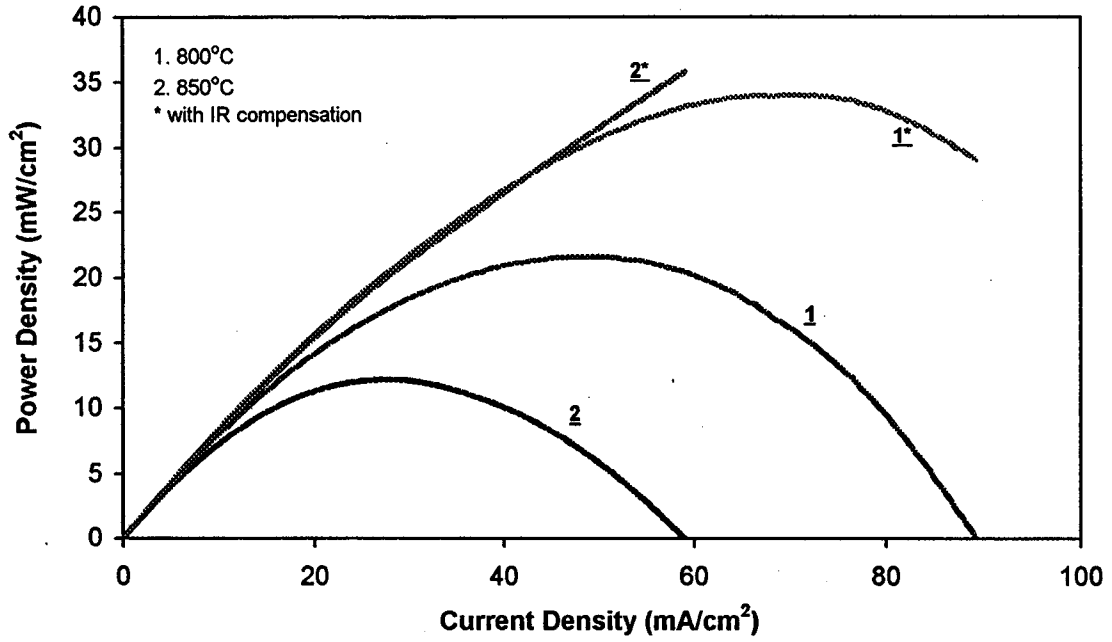


**Figure 6-7** Relationship between current density and power density for the cell using Fe-Mo-S as anode at 800°C and 850°C

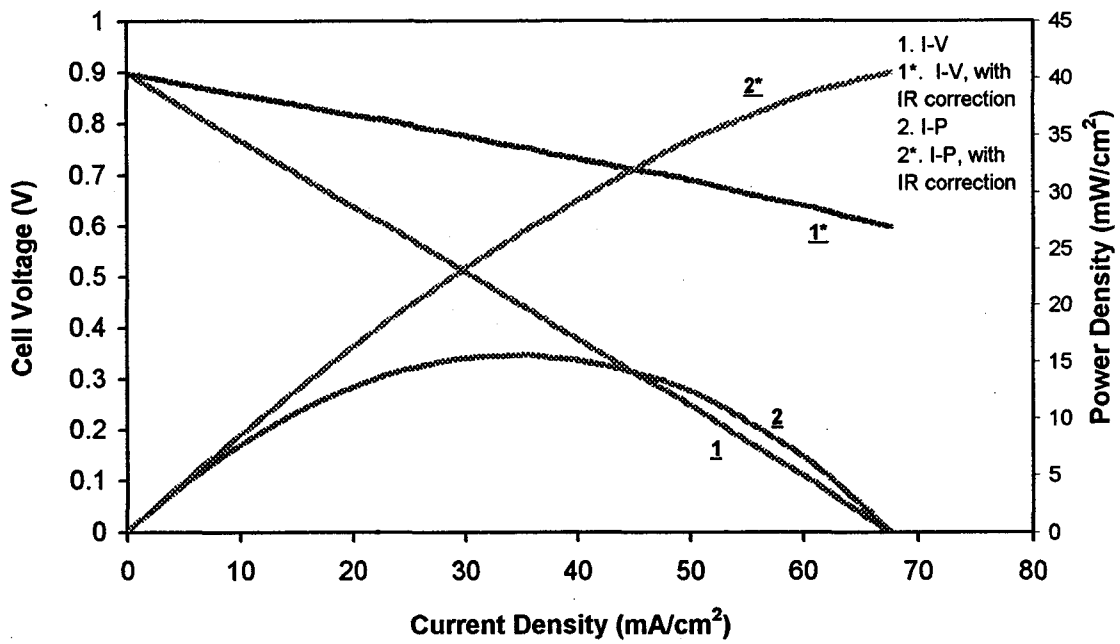


**Figure 6-8** Current-voltage and current-power relationships of H<sub>2</sub>S-air fuel cell using Ni-Mo-S anode at 850°C

### 6.3.2.5 Co-Mo-S

Use of Co-Mo-S as anode catalyst in H<sub>2</sub>S-air fuel cell gave better cell performance than either Fe-Mo-S or Ni-Mo-S. Figure 6-9 shows the relationship of current density to cell voltage for Co-Mo-S anode at 800°C and 850°C. The maximum current density was 83.3 mA/cm<sup>2</sup> at 800°C and 142 mA/cm<sup>2</sup> at 850°C. At 800°C, the current-voltage curve showed a steep drop in cell potential in the high current range, characteristic of mass transport limitation [20]. This was confirmed by the impedance spectra measured at 800°C under different polarization conditions (0.5 V, 0.4 V and 0 V), as displayed in Figure 6-10. The polarization resistance increased upon increasing the polarization amplitude. This result indicated that the applied voltage caused severe concentration polarization and hence increased the interfacial resistance. Nevertheless, the charge-transfer resistance was reduced. Therefore, mass transfer was the rate limiting process at 800°C. However, this effect was greatly reduced when the temperature was increased to 850°C. These observations were consistent with a mechanism in which sulfur was generated more rapidly at active sites than it was removed by desorption and transport at 800°C, which limited the ability of H<sub>2</sub>S fuel to access the triple-phase boundary, the reaction sites [3]. At 850°C, the rate of desorption and transport of sulfur from the vicinity of the active sites was increased, which thereby enhanced mass transport of H<sub>2</sub>S to the active sites.

As can be seen in Figure 6-11, the ohmic resistance of the cell with Co-Mo-S as anode catalyst increased with polarization at 800°C. However, the adherence of Pt current collecting film to Co-Mo-S anode surface deteriorated less rapidly than for either Fe-Mo-S or Ni-Mo-S, suggested by a smaller increase in cell ohmic resistance. Compared to the

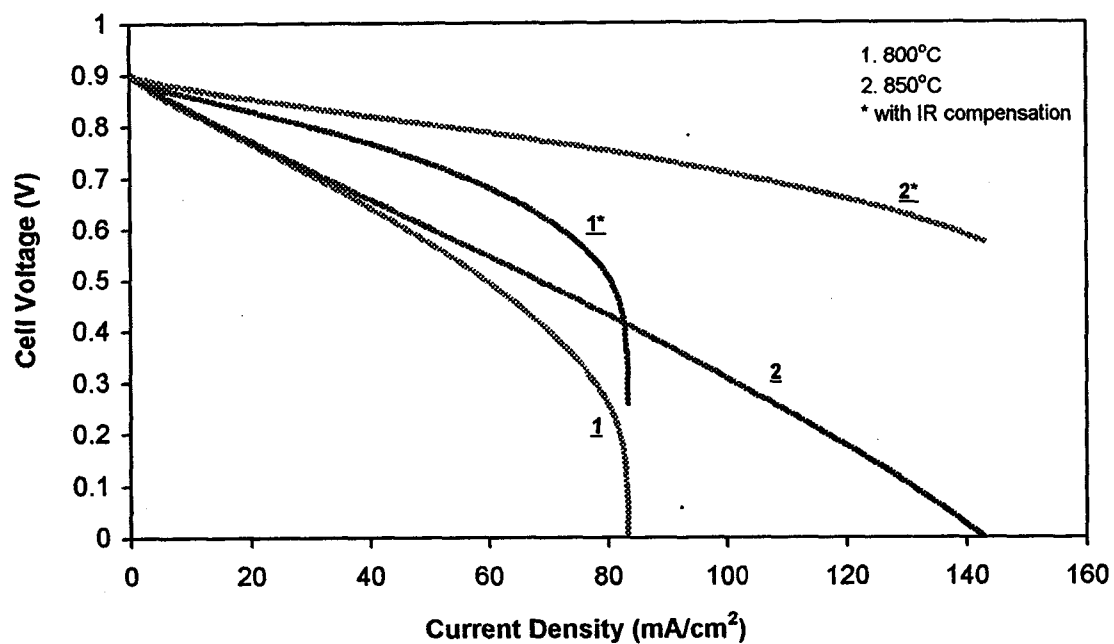


**Figure 6-9** The relationship between current density and cell voltage using Co-Mo-S anode at 800°C and 850°C

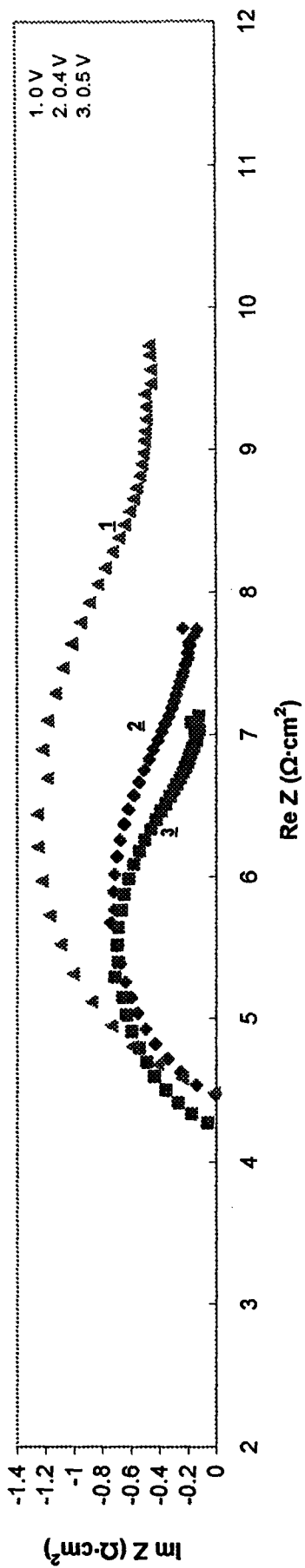


Figure 6-10 Impedance spectra for the cell using Co-Mo-S anode at 800°C under different polarization conditions

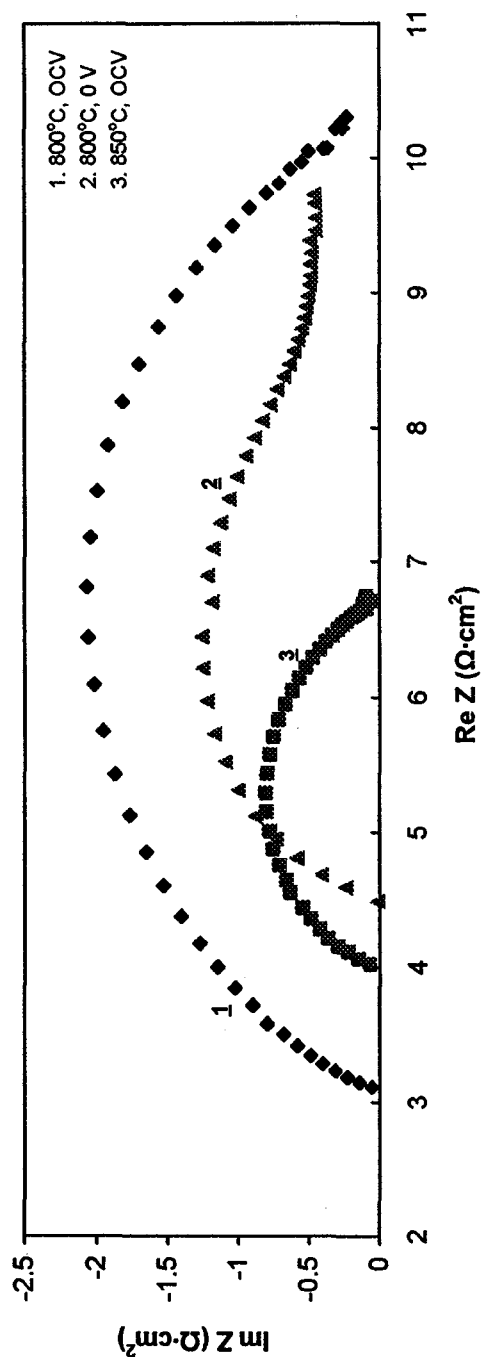
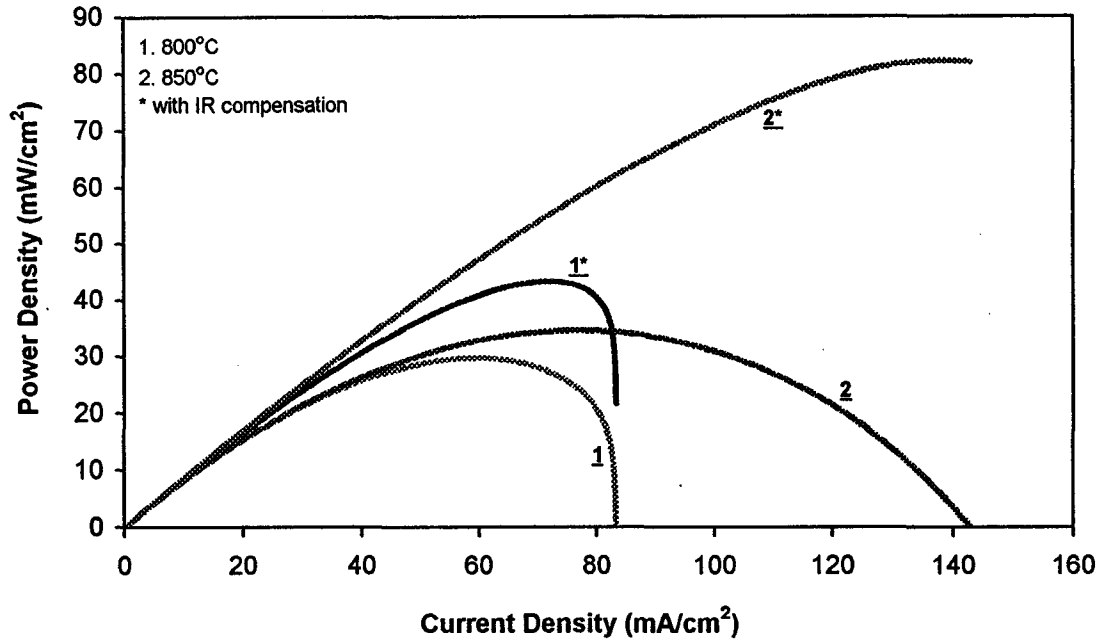


Figure 6-11 Impedance spectra for the cell using Co-Mo-S anode at different temperatures and polarization conditions

data acquired under open circuit conditions, the cell area specific ohmic resistance increased only  $1.38 \Omega \cdot \text{cm}^2$  for the condition of polarization at 0 V. In a similar manner to Fe-Mo-S, the resistance of Co-Mo-S decreased with increasing temperature, which suggested that the temperature change alone had no deleterious effects on the interface between the Pt film and the anode.

The power density characteristics at cell operating temperatures of 800°C and 850°C are shown in Figure 6-12. The values of maximum power density at 800°C and 850°C were similar, 29.7 and 34.6  $\text{mW}/\text{cm}^2$  respectively. However, the maximum IR compensated value at 850°C was over 80  $\text{mW}/\text{cm}^2$ , approximately double that at 800°C. The excellent cell performance after IR compensation using each of Fe-Mo-S, Ni-Mo-S and Co-Mo-S as anodes indicated that the above binary metal sulfides were active catalysts for the electrochemical oxidation of  $\text{H}_2\text{S}$ , but that improved contact was required.

The high activity of these catalysts is attributed to the properties of the M-Mo-S structure (M = Fe, Co, Ni), a general feature previously recognized for  $\text{MoS}_2$ -based HDS catalysts [11-13]. This type of structure is regarded as a  $\text{MoS}_2$ -like phase with the promoter atoms (Fe, Co or Ni) located at the edges [22]. These materials appeared to have been stable throughout the whole tests. No sublimation of the binary anode catalysts was detected. The IR corrected data showed that it was necessary to improve electrical contact in order to realize the full potential for these anode catalysts. The major source of the large ohmic resistance in the cell was the poor electrical contact between Pt film and anode. Consequently, we have also examined alternative compositions of the anode, with the objective of improving electrical contact and reducing ohmic resistance.



**Figure 6-12** The relationship between current density and power density using Co-Mo-S anode at 800°C and 850°C

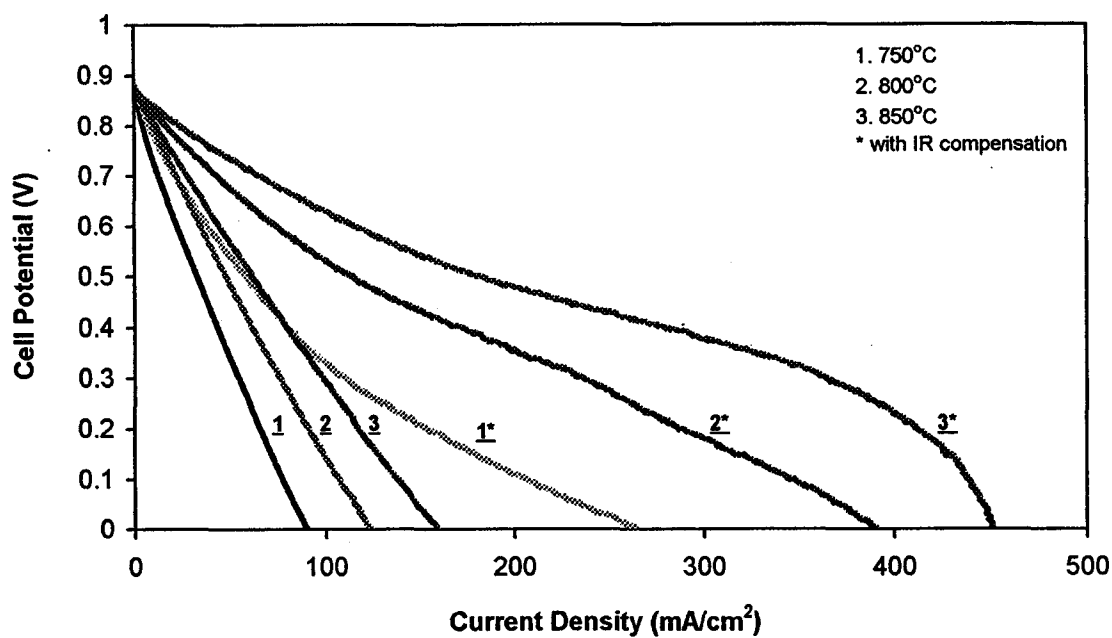
### 6.3.3 Admixing Ag Powder into Co-Mo-S Anode Catalyst

In order to overcome the weak bonding and poor electrical contact of Pt current collecting film with the anode, I investigated alternative anode compositions, in particular, composite anodes having up to 10% Ag powder admixed with Co-Mo-S, with the objective of improving anode electrical conductance. It was found that, when Ag powder was well distributed in the anode, the anode and mesh current collector were in good electrical contact. Thus there was no need to apply a Pt film, thereby avoiding the presence of an unstable interface between Pt film and anode, and also increasing the intimate contact area.

Ag powder easily reacts with sulfur to form  $\text{Ag}_2\text{S}$ . However,  $\text{Ag}_2\text{S}$  thermally decomposes to its elements above  $200^\circ\text{C}$  [23]. As a result, whereas formation of PtS increased resistance and caused detachment of the current collector, there were no similar adverse effects resulting from use of Ag powder. Pt mesh spot-welded with a Pt lead made good electrical contact when placed directly across the surface of the anode.

#### 6.3.3.1 Current-Voltage and Power Density Performance

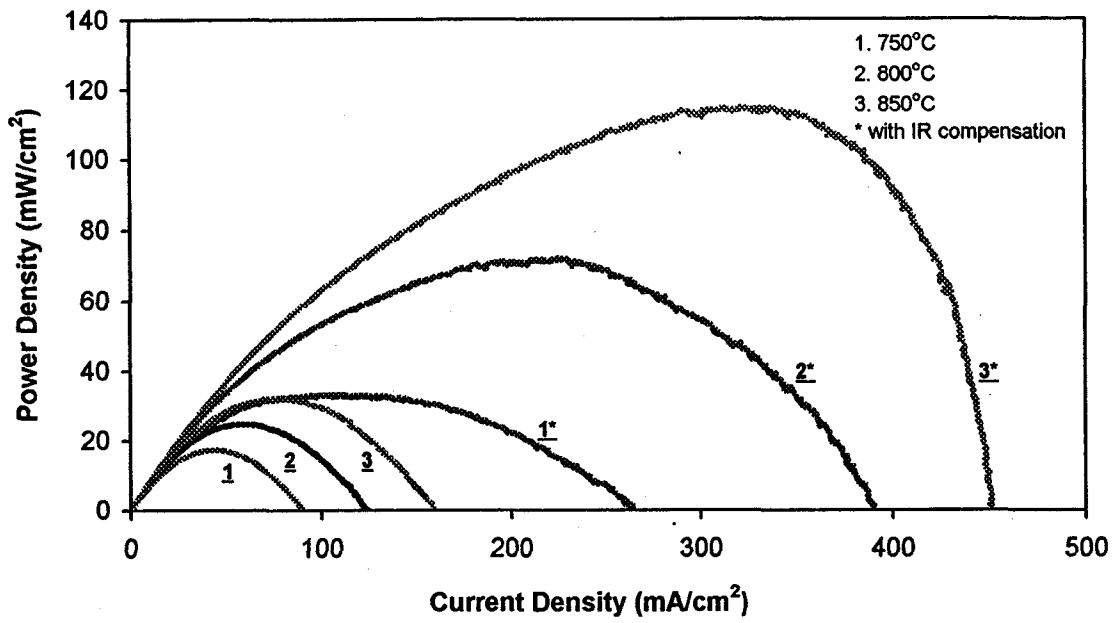
The cell was operated at  $750\text{-}850^\circ\text{C}$  and at atmospheric pressure for five consecutive days. Figure 6-13 shows the current vs. voltage relations for the third day of operation. Curves 1, 2 and 3 were measured without IR compensation, while curves 1\*, 2\* and 3\* were determined using the IR compensation function of the Gamry system. The maximum current density increased with temperature, both with and without IR correction. The values without IR compensation were  $90.5, 124, 159 \text{ mA/cm}^2$  at  $750^\circ\text{C}$ ,



**Figure 6-13** The relationship between current density and cell voltage at 750°C, 800°C and 850°C using (Co-Mo-S)+5%Ag as anode

800°C and 850°C, respectively. With IR compensation, the highest maximum current density of 450 mA/cm<sup>2</sup> was achieved at 850°C. The I-V curve 3\* in Figure 6-13 indicated a slight mass transfer limitation in the high current region. However, this characteristic was not observed at 750°C (Curve 1\*) or 800°C (Curve 2\*), probably because sulfur produced at high reaction rate at 850°C occupied the active sites or the reaction rate on the surface of the anode was higher than the O<sup>2-</sup> supply rate to the active sites at the three phase boundary, and therefore limited the further reaction of H<sub>2</sub>S gas.

The current-power density curves for the third day of operation are presented in Figure 6-14. The maximum power density increased with increasing temperature. The initial parts of these curves overlapped, suggesting that the electrocatalytic activity of the anode was independent of temperature at low current densities. The maximum values for non-IR and IR compensated power density were 32 and 115 mW/cm<sup>2</sup> at 850°C, respectively. The large gap between the cell performances with and without IR compensation at the same temperature, as shown in both Figure 6-13 and 6-14, indicated that it was imperative to reduce the cell ohmic losses in order to attain a better actual cell performance. It was anticipated that the ohmic resistance of the electrolyte could be lowered by reducing its thickness or adopting anode- or cathode-supported thin film cell designs. Further improvements could be realized by using alternative electrolyte materials with higher ionic conductivity, such as scandia-stabilized zirconia (ScSZ). The experimental apparatus required the use of approximately 1 m of Pt wire, which was subjected to the high temperature zone of the furnace and had a resistance of about 2 Ω at 750°C. The electrical resistance arising from the Pt connecting wires can be reduced by reducing their length for use in a practical cell.



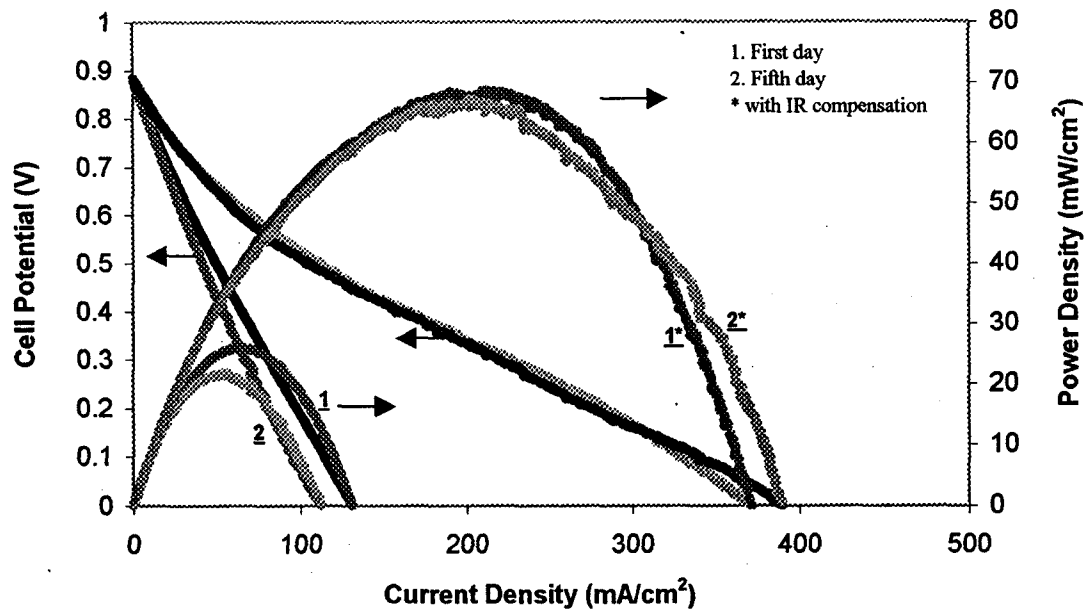
**Figure 6-14** The relationship between current density and power density at 750°C, 800°C and 850°C using (Co-Mo-S)+5%Ag as anode

Figure 6-15 gives the cell performances for the first and the last day operation at 800°C. As can be seen, the current-voltage and current-power relations acquired with IR compensation mode for the two days were almost identical, except for the high current region. The stable IR compensated cell performance showed the superior activity and longevity of the composite sulfide anode catalyst when compared with the poisoning of Pt in H<sub>2</sub>S atmosphere. On the contrary, the non-IR compensated current and power output both decreased with time, which was ascribed to the increase in cell ohmic resistance. The impedance analysis showed that the high frequency intercept of impedance spectra increased about 0.4 Ω from the 1st day to the 5th day. This probably was attributable to the sulfurization of the surfaces of Pt wire and Pt mesh after exposing them to pure H<sub>2</sub>S environment for a prolonged period of time at high temperatures, leading to a increase in contact and electrical resistance. The slight increase in cell ohmic resistance for the present system after operating for 5 days indicated greatly improved electrical contact characteristics in comparison with the use of metal sulfide catalysts having an overlayer of Pt.

Figure 6-16 displays the maximum current densities and power densities with IR compensation at 850°C for the duration of 5 days. The current and power values were higher than those for a Pt film/Co-Mo-S anode system, and the performance was sustainable for a much longer time, showing that the anode catalyst comprising Co-Mo-S catalyst admixed with Ag powder had higher performance and integrity.

#### 6.3.3.2 Impedance Characteristics

Figure 6-17 shows the typical variation of the complex impedance spectrum under



**Figure 6-15** Comparison of current-voltage and current-power relationships during the 1st and 5th day of operation at 800°C using (Co-Mo-S)+5%Ag as anode

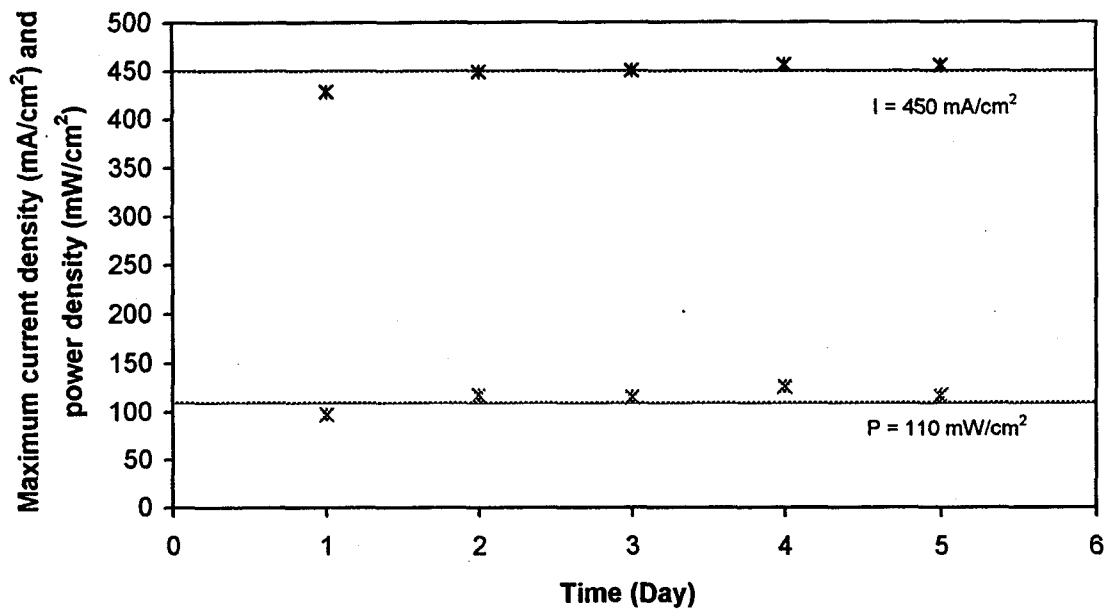


Figure 6-16 Maximum current density and power density of H<sub>2</sub>S-air fuel cell as a function of time on stream at 850°C

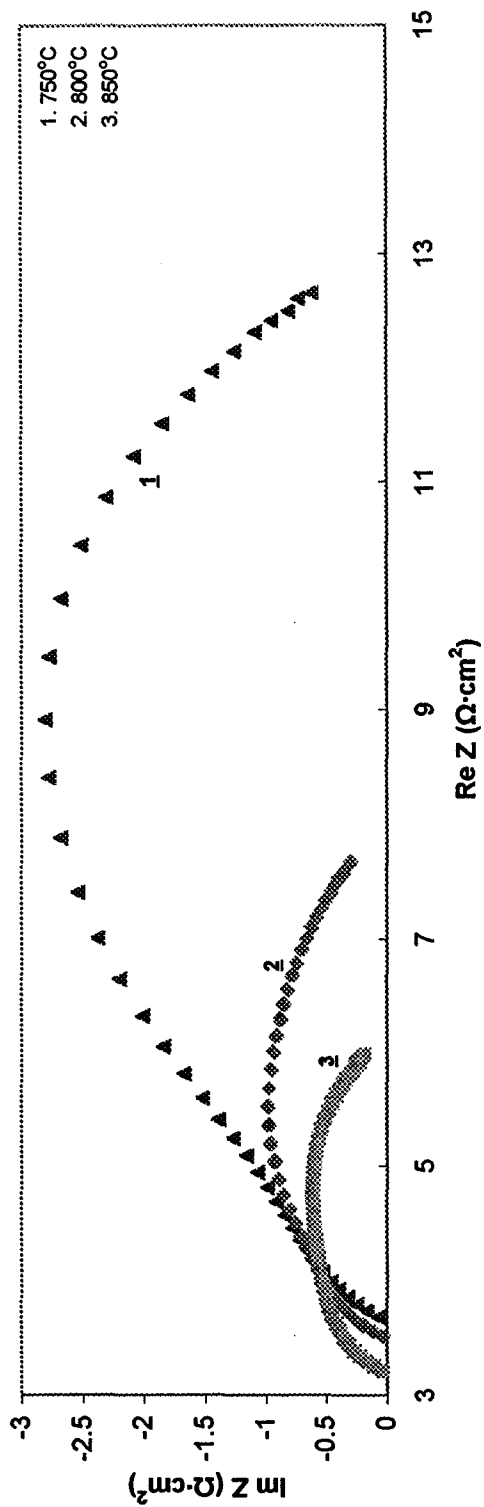
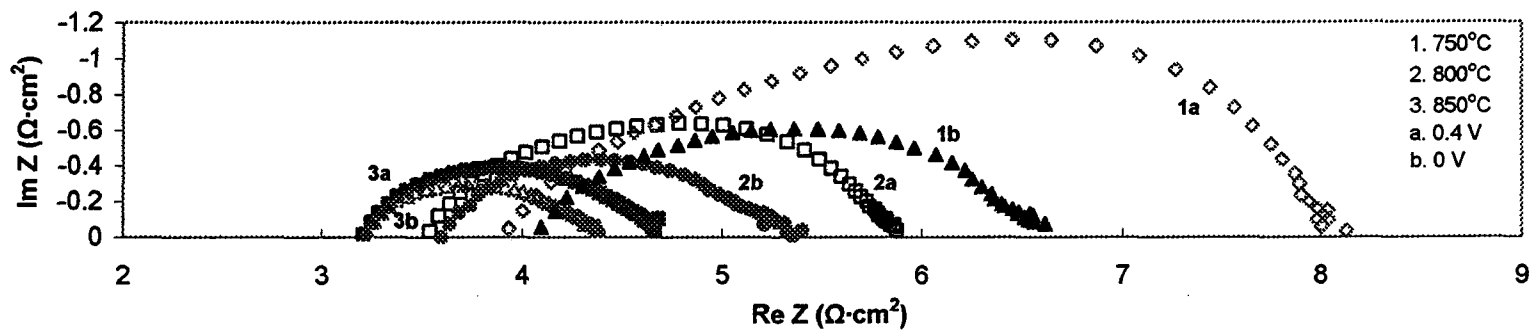


Figure 6-17 Impedance spectra for the cell using (Co-Mo-S)+5%Ag as anode at different temperatures under open circuit conditions

open circuit conditions with temperature within one day of operation. The high frequency intercept decreased with increasing operating temperature, which was consistent with the enhanced ionic conductivity of the YSZ electrolyte at higher temperatures. Unlike platinum, the anode catalyst was always in good intimate contact with the electrolyte and the interface stability was not affected by electrochemical polarization. As shown in Figure 6-17, the size of the impedance arcs was reduced significantly as temperature increased, which can be ascribed to the substantial improvement in the electrochemical reaction rate. Consequently, the maximum power density and current density obtained at 850°C were nearly two times higher than at 750°C, as displayed in Figures 6-13 and 6-14.

The impedance spectra measured at three different temperatures under polarization conditions (0.4 V and 0 V) are presented in Figure 6-18. For each temperature, the total cell resistance decreased with the amplitude of polarization. It is obvious that the cell ohmic resistance remained almost unchanged at a constant temperature and the decrease in total cell resistance resulted from the reduction in the polarization resistance. This behavior indicated that the influence of the applied polarization amplitude on the charge-transfer enhancement was stronger than on concentration polarization, which suggested that the electrode processes were primarily controlled by charge transfer, rather than by mass transfer near the electrolyte-electrode interfaces. The nearly linear I-V curves without IR compensation in Figure 6-13 support this conclusion.

The activation effect, which has been described for Pt catalyst in Chapter 4, section 4.3.2.2, was also observed for the anode material consisting of Co-Mo-S catalyst admixed with Ag. During each day of operation, the cell was first characterized



**Figure 6-18** Impedance spectra for the cell using (Co-Mo-S)+5%Ag as anode at different temperatures under polarization conditions

at 750°C until completion of that set of tests; then the temperature was increased to 800°C and 850°C to continue the studies. At 750°C, two impedance measurements were performed at OCV. The first test was done after pure H<sub>2</sub>S gas was supplied to the anode for about one hour and the cell reached a stable open circuit potential. Then the cell was polarized at a constant voltage of 0.6 V for 10 min. After about 30 min of subsequent equilibration, another measurement was taken at OCV (Figure 6-19). After passing current, the polarization resistance at OCV was significantly lower than the initial value, suggesting that the electrode was activated. Further polarization could not decrease the impedance arcs any further, i.e., a fully activated state had been achieved. The activated state could be maintained for subsequent studies at 800°C and 850°C during the same day, as no decrease in polarization resistance at OCV was observed for either temperature after the similar activation process. However, the electrode activation was not sustained on standby overnight, during which the cell was at 750°C and the anode feed was switched back to nitrogen. The activation phenomenon was persistent for the remaining days of operation when using the same fuel cell. When the cell was operated at an initial temperature of 750°C each day, decreased impedance arcs at OCV were obtained after polarization. Temperature seemed to have no direct effect on electrode activation. Other studies performed at a starting temperature of 850°C with the same anode catalyst showed that the electrode was activated only after passing current. However, the minimum amplitude of polarization or the amount of current as well as time of treatment required to fully activate these novel electrodes has not yet been optimized; an extensive systematic study will be required.

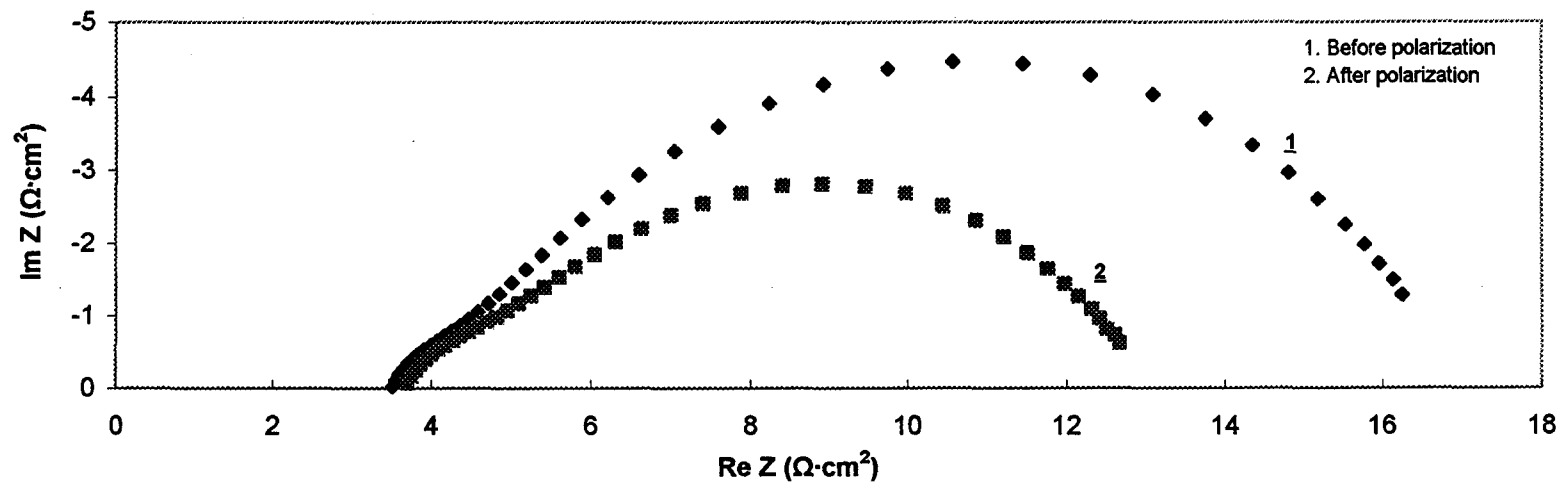


**Figure 6-19** Impedance spectra of the (Co-Mo-S+5%Ag)/YSZ/Pt cell at OCV under the influence of an applied voltage at 750°C

## 6.4 Conclusions

Four different metal sulfide catalysts have been shown to be active H<sub>2</sub>S-air fuel cell anode catalysts in the temperature range of 750-850°C. MoS<sub>2</sub> has a better activity than Pt for electrochemical oxidation of H<sub>2</sub>S. Binary metal sulfides M-Mo-S (M = Fe, Co, Ni) are not volatile, in contrast to MoS<sub>2</sub> alone, and have high activity. However, Pt film deposited as current collector across the metal sulfides does not have good adherence to the anode surface, and its performance is compromised by PtS reversibly formed by reaction with H<sub>2</sub>S or sulfur. Detachment of the Pt film from the anode resulted in a large increase in contact resistance and reduction in cell performance. Anode catalysts comprising Co-Mo-S admixed with up to 10% Ag powder were found to have better performance and longevity, and improved electrical contact when compared with Pt/M-Mo-S anode systems. Similar to Pt, the high-performance metal sulfide electrodes were activated by passing current. However, systematic studies need to be performed to determine the optimum current treatment, which can fully activate all electrodes, so that cell performance can be fully elucidated.

## References

- [1] Y. Matsuzaki and I. Yasuda, *Solid State Ionics*, **132**, 261 (2000).
- [2] J. M. Ralph, A. C. Schoeler and M. Krumpelt, *Journal of Materials Science*, **36**, 1161 (2001).
- [3] I. V. Yentekakis and C. G. Vayenas, *Journal of the Electrochemical Society*, **136**, 996 (1989).

- [4] T. J. Kirk and J. Winnick, *Journal of the Electrochemical Society*, **140**, 3494 (1993).
- [5] D. Peterson and J. Winnick, *Journal of the Electrochemical Society*, **143**, L55 (1996).
- [6] D. Peterson and J. Winnick, *Journal of the Electrochemical Society*, **145**, 1449 (1998).
- [7] M. Liu, P. He, J. L. Luo, A. R. Sanger and K. T. Chuang, *Journal of Power Sources*, **94**, 20 (2001).
- [8] P. He, M. Liu, J. L. Luo, A. R. Sanger and K. T. Chuang, *Journal of the Electrochemical Society*, **149**, A808 (2002).
- [9] N. U. Pujare, K. J. Tsai and A. F. Sammells, *Journal of the Electrochemical Society*, **136**, 3662 (1989).
- [10] C. Yates and J. Winnick, *Journal of the Electrochemical Society*, **146**, 2841 (1999).
- [11] D. A. Agievskii, M. V. Landau and A. A. Slinkin, *Kinetics and Catalysis*, **29**, 792 (1989).
- [12] E. I. Stiefel, 'Kirk-Othmer Encyclopedia of Chemical Technology', Vol. 16 (Molybdenum Compounds), John Wiley & Sons, New York (2001).
- [13] J. A. Rodriguez and M. Kuhn, *Journal of Vacuum Science & Technology A*, **14**, 1609 (1996).
- [14] T. Chivers, J. B. Hyne and C. Lau, *International Journal of Hydrogen Energy*, **5**, 499 (1980).
- [15] M. Breysse, R. Frety and M. Vrinat, *Applied Catalysis*, **12**, 165 (1984).

- [16] S. V. Slavov, K. T. Chuang, A. R. Sanger, J. C. Donini, J. Kot and S. Petrovic, *International Journal of Hydrogen Energy*, **23**, 1203 (1998).
- [17] K. T. Chuang, J. C. Donini, A. R. Sanger and S. V. Slavov, *International Journal of Hydrogen Energy*, **25**, 887 (2000).
- [18] X. Zhang, S. Ohara, K. Mukai, M. Ogawa and T. Fukui, *Electrochemistry*, **68**(1), 11 (2000).
- [19] O. E. Beqqali, I. Zorkani, F. Rogemond, H. Chermette, R. B. Chaabane, M. Gamoudi and G. Guilaud, *Synthetic Metals*, **90**, 165 (1997).
- [20] J. O'M. Bockris and S. Srinivasan, '*Fuel Cells: Their Electrochemistry*', Chapter 4, McGraw-Hill, New York (1969).
- [21] M. Gödickemeier, K. Sasaki and L. J. Gauckler, *Journal of the Electrochemical Society*, **144**, 1635 (1997).
- [22] H. Topsøe and B. S. Clausen, *Catalysis Reviews: Science and Engineering*, **26**, 395 (1984).
- [23] J. E. Macintyre, F. M. Daniel and V. M. Stirling, '*Dictionary of Inorganic Compounds*', 1st ed., Vol. 1, p. 14, Chapman & Hall, London (1992).

## CHAPTER 7

# CONCLUSIONS, RECOMMENDATIONS AND FUTURE WORK

The potential utilization of hydrogen sulfide as fuel in solid oxide fuel cells has been investigated using different kinds of anode catalysts. I have developed a series of novel composite metal sulfide catalysts, and have demonstrated their superiority for use in H<sub>2</sub>S-air fuel cells over conventional Pt-based anode catalysts.

### 7.1 Pt Anode Catalyst Directly Deposited on YSZ

Platinum has good electrocatalytic activity for the conversion of H<sub>2</sub>S in a zirconia-based solid electrolyte fuel cell operating at the temperature range of 750°C-850°C, which has been shown by the promising initial values of current and power output obtained with a 5% H<sub>2</sub>S fuel stream. A non-IR corrected power density of about 16 mW/cm<sup>2</sup> and current density of 100 mA/cm<sup>2</sup> were achieved at 800°C. Furthermore, this performance could be improved significantly by reducing cell ohmic losses, such as using shorter connecting wires and enhanced electrical contacts. However, platinum anode catalyst directly deposited on YSZ surface is not suitable for a prolonged operation in the diluted H<sub>2</sub>S stream since the Pt/YSZ interface is physically unstable over time on stream, leading to an increase in contact resistance.

Cell performance with the use of Pt catalyst in pure H<sub>2</sub>S feed was much worse than that in 5% H<sub>2</sub>S feed. Moreover, cell performance in pure H<sub>2</sub>S stream deteriorated

very rapidly, resulting in a shorter lifetime, which is typically 5-6 h. This was attributed to severe degradation and detachment of Pt anode in the concentrated H<sub>2</sub>S stream. The degradation rate of the anode catalyst was strongly affected by the current passing through the fuel cell. At elevated temperatures, dynamic reversible formation and decomposition of PtS on the platinum surface caused instability of the Pt/YSZ interface. A high current density accelerated the mass transportation of H<sub>2</sub>S towards the Pt/YSZ interface and the formation of PtS, and hence accelerated detachment of the Pt anode from the YSZ electrolyte. As a result, the contact resistance between Pt anode and the electrolyte increased significantly, leading to the rapid failure of the fuel cell. Cell performance also decreased with exposure time in pure H<sub>2</sub>S stream and often showed diffusion limitation after a prolonged period of time. With extending the exposure time, more active Pt sites were covered by sulfur and converted to PtS. Both effects reduced the number of available active sites and impeded the transport of the reactant gas onto and the products away from the three-phase reaction zone. Contaminated Pt anode was partly cleaned by polarizing the electrode in H<sub>2</sub> atmosphere or baking the electrode/electrolyte assembly in N<sub>2</sub> atmosphere at high temperatures.

While high electrochemical reaction rate accelerated the degradation of the Pt anode significantly, a short-time low current polarization may activated some electrodes. The nature of the activation process has so far not been revealed. However, in order to obtain comparable data, the electrodes have to be pretreated with an optimum current to reach a fully activated state.

**Recommendation:**

Avoid use of Pt as anodes in H<sub>2</sub>S-air fuel cells.

## 7.2 Stabilization of Pt Anode Catalyst with TiO<sub>2</sub> Interlayer

A very thin (submicron) layer of TiO<sub>2</sub> added to the anode surface of YSZ electrolyte before depositing the Pt catalyst stabilized the Pt/YSZ interface. Stability of cell performance has thereby been significantly improved by applying this intermediate TiO<sub>2</sub> layer, which helped anchor the Pt anode to YSZ and increased the activity due to the spillover effect. The porous TiO<sub>2</sub> layer prepared by paste painting rendered better performance than the dense spin-coated layer applied by sol-gel technique. However, cell performance decreased greatly during initial operation.

### **Recommendation and future work:**

More extensive studies are needed to investigate the interaction between Pt anode catalyst, TiO<sub>2</sub> interlayer and YSZ electrolyte under H<sub>2</sub>S atmosphere at high temperatures, in order to find out the reason for the initial rapid degradation in cell performance so that it can be improved.

It is anticipated that cell performance could be improved by interposing a thin layer of a good oxygen ion and electronic conductor instead of TiO<sub>2</sub>. This conductor should be stable in pure H<sub>2</sub>S atmosphere and will not penetrate to YSZ electrolyte during lengthy operation. Doped CeO<sub>2</sub> could be a candidate material for this application. It is well known that CeO<sub>2</sub> doped with CaO, Y<sub>2</sub>O<sub>3</sub>, Sm<sub>2</sub>O<sub>3</sub>, Gd<sub>2</sub>O<sub>3</sub> and a number of other rare earth oxides has higher oxygen-ion conductivity than most stabilized zirconia [1]. Moreover, doped ceria develops electronic conductivity due to the reduction of Ce (IV) to Ce (III) at low oxygen partial pressures prevailing in the anode compartment. However, one should be cautious to avoid heat treatment of ceria and zirconia at temperatures

above 1200°C because the two materials in direct contact will react and diffuse into each other at this temperature and then form solid solutions that have much lower ionic conductivity [2].

Another alternative approach is to replace the Pt/TiO<sub>2</sub> layer with Pt/YSZ cermet [3]. Similar to Ni/YSZ cermet commonly used in most standard solid oxide fuel cells, the Pt/YSZ cermet affords benefits, including compatible thermal expansion coefficient with the electrolyte, control of Pt grain growth and extension of three-phase boundary area for the fuel oxidation reaction in addition to the stabilization of the anode.

### **7.3 Metal Sulfide Anode Catalysts**

Four different metal sulfides have been shown to be active anode catalysts for H<sub>2</sub>S-air fuel cell at the operating temperature of 750-850°C. MoS<sub>2</sub> has a superior activity to Pt for the electrochemical oxidation of H<sub>2</sub>S, but is highly volatile. In contrast to MoS<sub>2</sub> alone, binary metal sulfides M-Mo-S (M = Fe, Co, Ni) are not volatile and have high electrocatalytic activity. However, Pt film deposited as current collector across the metal sulfide anodes does not have good adherence to the electrode surface, and its performance is compromised by PtS reversibly formed by reacting with H<sub>2</sub>S or sulfur. Detachment of the Pt film from the metal sulfide anodes resulted in a large increase in contact resistance and consequent reduction in cell performance. Anode catalysts comprising Co-Mo-S admixed with up to 10% Ag powder were found to have excellent performance and longevity, and improved electrical contact when compared with Pt/M-Mo-S anode systems. A current density of 450 mA/cm<sup>2</sup> and power density of 115

$\text{mW/cm}^2$  were achieved at  $850^\circ\text{C}$  with IR compensation. Similar to Pt anode catalyst, the high-performance metal sulfide electrodes were activated while passing current.

**Recommendation and future work:**

Systematic studies need to be performed to determine the optimum preparation and current treatment, to fully activate all electrodes.

The big difference between the IR compensated and non-IR compensated cell performance at the same temperature indicated that it is imperative to reduce the cell ohmic losses in order to attain a better actual cell power output. It is anticipated that the ohmic resistance of the electrolyte can be lowered by reducing its thickness [4] or adopting anode- or cathode-supported thin film cell design [5]. Further improvements could be realized by using alternative electrolyte materials with higher ionic conductivity, such as scandia-stabilized zirconia (ScSZ) [6]. The electrical resistance arising from the Pt connecting wires is expected to be reduced by using a more advanced cell configuration in which the lead is shortened so that its resistance is minimal. Contact resistance could be improved by submerging Pt lead in the electrode material.

#### **7.4 Product Distribution of $\text{H}_2\text{S}$ -Air Fuel Cell**

Gas analysis results showed that both hydrogen sulfide and hydrogen formed from the decomposition of  $\text{H}_2\text{S}$  at elevated temperatures were actively involved in the half-cell reactions occurring at the anode. However, it is unlikely to identify the dominant electrocatalytic species based on the available data. Furthermore, gas analysis studies with a dilute stream of hydrogen sulfide suggested that the product distribution changed from sulfur to sulfur dioxide with increasing current. Especially at very high fuel

utilizations, sulfur dioxide was predominant in the anode outlet streams, and sulfur produced from the partial oxidation of  $\text{H}_2\text{S}$  seemed to be further oxidized electrochemically to  $\text{SO}_2$ . No sulfur dioxide was detected in the anode effluents for pure  $\text{H}_2\text{S}$  feed, attributed to the reaction of  $\text{SO}_2$  with excess  $\text{H}_2\text{S}$  in the anode compartment through the Claus reaction.

The generation of sulfur dioxide from the  $\text{H}_2\text{S}$ -air fuel cell could pose a disposal problem due to its gaseous nature. For cases where there is a market for sulfuric acid,  $\text{SO}_2$  could be utilized as a precursor to produce sulfuric acid. Otherwise,  $\text{SO}_2$  could react further with  $\text{H}_2\text{S}$  to produce elemental sulfur, a salable product, using existing Claus technology, which could be realized by operating the  $\text{H}_2\text{S}$ -air SOFC on concentrated  $\text{H}_2\text{S}$  fuel streams. Another approach would be to use proton conductors as the electrolyte to replace the oxygen ion conductors such as YSZ. Sulfur would be the only anodic product for this type of fuel cell. Some promising proton ceramics have been tested for the use with hydrocarbon fuels [7]. Finding solid electrolytes with high proton conductivity and stability in  $\text{H}_2\text{S}$  atmosphere at high fuel cell operating temperatures, and removing the large amounts of sulfur produced to prevent the poisoning of the catalysts, are the most challenging problems facing this new technology.

## References

- [1] S. P. S. Badwal and K. Foger, *Materials Forum*, **21**, 187 (1997).
- [2] A. Tsoga, A. Gupta, A. Naoumidis, D. Skarmoutsos and P. Nikolopoulos, *Ionics*, **4**, 234 (1999).

- [3] H. Shiga, T. Okubo and M. Sadakata, *Industrial and Engineering Chemistry Research*, **35**, 4479 (1996).
- [4] T. Tsai, E. Perry and S. Barnett, *J. Electrochem. Soc.*, **144** (1997) L130.
- [5] P. Holtappels and U. Stimming, '*Handbook of Fuel Cells*', Vol. 1, Chapter 20, John Wiley & Sons Ltd., West Sussex, England (2003).
- [6] Y. Arachi, H. Sakai, O. Yamamoto, Y. Takeda and N. Imanishi, *Solid State Ionics*, **121**, 133 (1999).
- [7] W. G. Coors, *Journal of Power Sources*, **118**, 150 (2003).

# APPENDIX A

## GC ANALYSIS

### A.1 Operating Parameters of GC and Detectors

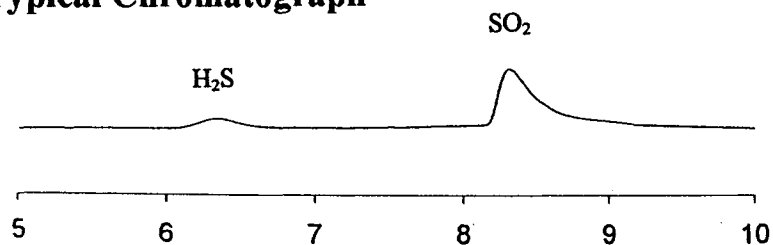
**Table A-1** Parameters under which GC and its detectors worked for analysis of sulfur-containing compounds

<i>Description</i>	<i>Value</i>
Oven temperature program	50°C for 5 min; to 120°C at 25°C/min; and held for 3 min
TCD temperature	200°C
Carrier gas flow rate for packed column	30 mL/min
Capillary column head pressure	65 kPa guage
Splitting flow rate	100 mL/min
SCD burner temperature	800°C
SCD burner pressure	34.6 kPa absolute
Flow rate of H <sub>2</sub> to SCD burner	100 mL/min
Flow rate of air to SCD burner	40 mL/min
Pressure of air in ozone generator	41.4 kPa guage

**Table A-2** Parameters under which GC and its detector worked for analysis of H<sub>2</sub>

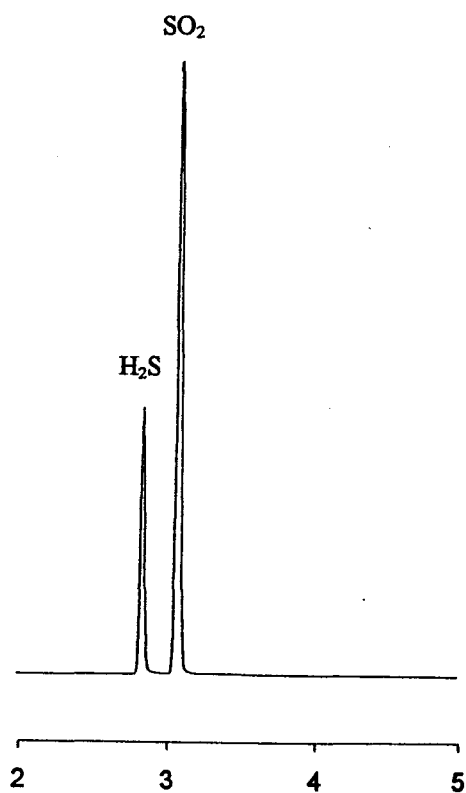
<i>Description</i>	<i>Value</i>
Oven temperature program	30°C for 3 min; to 150°C at 40°C/min; and held for 8 min
TCD temperature	220°C
Carrier gas flow rate for packed column	35 mL/min
Head pressure	165 kPa guage

## A.2 Typical Chromatograph



Time (min)

(a)



Time (min)

(b)

**Figure A-1 (a)** TCD chromatograph of typical sulfur containing compounds separated using a packed column with Porapak Q packing and **(b)** SCD chromatograph of the same sulfur-containing compounds separated using CP-Sil 5CB capillary column at a chosen temperature program shown in Table A-1

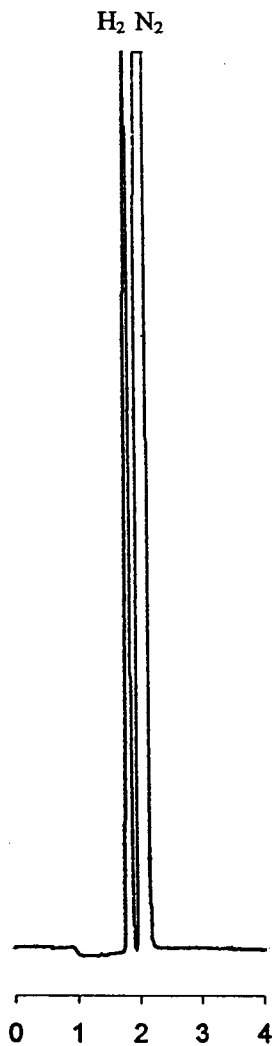


**Figure A-2** TCD chromatograph of non-sulfur containing compounds separated using a packed column with Porapak R packing at a chosen temperature program shown in Table A-2

### A.3 Calculation of Reaction Rates of H<sub>2</sub>S, SO<sub>2</sub> and H<sub>2</sub>

The reaction rates of H<sub>2</sub>S, SO<sub>2</sub> and H<sub>2</sub> at different current densities can be calculated using the following equation:

$$r = \frac{Pv(X_o - X_i)}{RT} \quad (\text{A-1})$$

When the cell current was 59 mA/cm<sup>2</sup> at 800°C,

$$r_{\text{H}_2\text{S}} = \frac{Pv(X_{o,\text{H}_2\text{S}} - X_{i,\text{H}_2\text{S}})}{RT} = \frac{101325\text{Pa} \times 6.1\text{mL}/\text{min} \times (4.01\% - 0.473\%)}{8.314\text{JK}^{-1}\text{mol}^{-1} \times 298.15\text{K}} = 14.7 \times 10^{-8} \text{mol}/\text{s}$$

$$r_{\text{SO}_2} = \frac{PvX_{i,\text{SO}_2}}{RT} = \frac{101325\text{Pa} \times 6.1\text{mL}/\text{min} \times 1.36\%}{8.314\text{JK}^{-1}\text{mol}^{-1} \times 298.15\text{K}} = 5.65 \times 10^{-8} \text{mol}/\text{s}$$

$$r_{\text{H}_2} = \frac{Pv(X_{o,\text{H}_2} - X_{i,\text{H}_2})}{RT} = \frac{101325\text{Pa} \times 6.1\text{mL}/\text{min} \times (0.3595\% - 0.03875\%)}{8.314\text{JK}^{-1}\text{mol}^{-1} \times 298.15\text{K}} = 1.33 \times 10^{-8} \text{mol}/\text{s}$$

### A.4 Conversions of H<sub>2</sub>S and H<sub>2</sub>

The conversions of H<sub>2</sub>S and H<sub>2</sub> at different cell current densities can be calculated using the following equation:

$$\text{Conversion}\% = \frac{X_o - X_i}{X_o} \quad (\text{A-2})$$

Table A-3 gives the calculated conversions of H<sub>2</sub>S and H<sub>2</sub> based on their measured concentrations at different total cell current densities and the theoretical conversions of H<sub>2</sub>S to either sulfur or SO<sub>2</sub> based on the current drawn from the cell.

**Table A-3 Conversions of H<sub>2</sub>S and H<sub>2</sub>**

<i>Current Density</i> (mA/cm <sup>2</sup> )	<i>Calculated Conversion</i> (%)		<i>Theoretical Conversion of H<sub>2</sub>S</i> (%)	
	H <sub>2</sub>	H <sub>2</sub> S	Reaction (3-2)	Reaction (3-3)
0	0	0	0	0
26	75.7	69.2	74.4	24.8
59	89.2	88.2	*	58.2
87	92.9	97.1	*	87.7
90	93.2	97.2	*	90.3

\* These conversion values are above 100% if the reacted H<sub>2</sub>S was completely converted to sulfur, which indicates that H<sub>2</sub>S was converted to both sulfur and SO<sub>2</sub> under the corresponding current densities.

### A.5 Calculation of Stoichiometric Values in Figures 4-14 and 4-15

$$r_{SO_2} = \frac{I}{6F} \quad (\text{the line for } n=6 \text{ in Figure 4-15})$$

$$r_{H_2S} = \frac{I}{6F} \quad (\text{the line for } n=6 \text{ in Figure 4-14})$$

$$r_{H_2S} = \frac{I}{2F} \quad (\text{the line for } n=2 \text{ in Figure 4-14})$$